OSAKA UNIVERSITY

DOCTORAL THESIS

Unique electrical transport properties of atomically layered antiferromagnets with high mobility

---

Author:
Mori WATANABE

Supervisor:
Yasuhiro NIIMI

Nanoscale Physics Group
Graduate School of Science

Preface

Atomically layered materials are a group of materials where two-dimensional sheet-like blocks are stacked on top of each other. In 2004, Novoselov and Geim had shown that simply by peeling layered materials with scotch tapes, an atomic monolayer can be obtained. Graphene, a single layer of graphite, is the first example to demonstrate the atomic monolayer from bulk graphite crystals. Since then, the ease of high-quality thin-film fabrication and the controllability of physical properties by electric fields have lead to active research of atomically layered materials.

In recent years, atomically layered magnetic materials have been gaining large attention especially in the field of magnetism. This was sparked by the study of CrI_3 and $CrGeTe_3$ in 2017, which reported the existence of long-range magnetic order even down to an atomic monolayer and bilayer respectively. While it is evident that this material group is attractive from an applicational point of view towards next generation spintronic devices, it is also attractive from a fundamental point of view, since magnetism can be changed when its dimensionality is lowered. Active research is being made to elucidate the detailed magnetic structure of various atomically thin magnets, and also to discover new properties arising from thin-film fabrication.

Meanwhile, studies of electrical transport in these materials are still largely under development. This is a missed opportunity since unique electrical

transport phenomena are expected to arise in a system where the conduction electrons are coupled to the magnetic order. For example, exotic magnetic textures coupled to the conduction electrons can induce unique electrical transport phenomena such as the topological or unconventional anomalous Hall effect. Therefore, the transport measurements provide information on the electronic and magnetic structure of the thin films, and also provide a stepping stone for nanoscale magnetic devices with novel electronic properties. The purpose of this thesis is to investigate the electronic transport properties unique to the atomically thin-film magnetic materials fabricated through the scotch tape method. Specifically, we have focused on two atomically layered antiferromagnets with high mobility.

The first is the rare-earth antiferromagnet $CeTe_3$. This material lies in the group of rare-earth tritellurides, which has recently gained attraction for its high mobility, arising from the complex Fermi surface structure due to the charge density wave formation. Especially in $CeTe_3$, strong Ruderman-Kittel-Kasuya-Yosida (RKKY) interaction is suggested from its bulk electrical transport measurements, indicating a strong coupling between the magnetic order and the conduction electrons. However, electrical transport measurements were previously unreported for thin films, likely due to the difficulty of device fabrication. Through magnetoresistance measurments of the $CeTe_3$ thin films, we observed two characteristics that were previously unreported in the bulk counter part. One is the magnetoresistance hysteresis, which indicated the existence of anisotropy of the magnetic moments along the stacking direction of the thin film. The other is the clear quantum oscillation, which originates from a small Fermi pocket formed due to the charge density wave transition. From the temperature dependence of the quantum oscillation amplitude, it was shown that the effective mass was enhanced by a factor of roughly 7 at temperatures below the magnetic transition temperature, indicating a modulation of the Fermi surface due to the magnetic order.

The second is the triangular-lattice antiferromagnet Ag_2CrO_2. In this material, a unique magnetic state known as the partially disordered state is thought to be realized due to the geometrical frustration of the material. In this state, one in five spins acts as a free spin even under its magnetic transition temperature. Although this material is inherently poly-crystalline in bulk, thin-film fabrication significantly increases the crystallinity of the material, which allows for electrical transport measurements in such an exotic magnetic structure. We have performed magnetoresistance and Hall measurements, and observed the anomalous Hall effect in a temperature region near the magnetic transition temperature, where fluctuations of the magnetic moments are large. The obtained Hall angle reaches 4%, and its scaling relation with respect to the longitudinal conductivity indicates that this effect arises from extrinsic scattering mechanisms. It is strongly indicated that the fluctuating moment near the magnetic transition temperature plays a key role in the unique anomalous Hall effect.

This thesis is organized as follows. In Chapter 1, a brief introduction on the theoretical and experimental background related to the thesis is discussed. Chapter 2 explains the experimental method in detail, including the device fabrication conditions and measurement set up. In Chapters 3 and 4, we discuss magnetoresistance measurements of $CeTe_3$ and Ag_2CrO_2, respectively. In Chapter 5, we summarize the results of this thesis and provide perspectives towards future research.

Contents

Chapter 1

Introduction

In this Chapter, we outline experimental and theoretical backgrounds related to this thesis. First, a brief introduction on atomically layered magnetic materials is given. Then, we introduce background information on the two magnetic materials studied in this thesis, $CeTe_3$ and Ag_2CrO_2. Finally, a summary of the electrical transport phenomena related to this thesis is given.

1.1 Recent advancements in atomically layered magnets

In this section, we will briefly summarize the background on some atomically layered magnetic materials. As the name suggests, atomically layered materials are a group of materials, consisting of a two-dimensional sheet-like atomic structure stacked on top of each other. Sparked by the discovery of Graphene in 2004 [1], the study of these materials has become an important stream in the field of condensed matter physics. The ease of thin film fabrication through the scotch tape method has led to active research of atomically thin films with a wide variety of physical properties, such as metals, semimetals, topological insulators, semiconductors, or insulators [2]. Furthermore, fabrication of high quality heterostructures and control of physical properties through electric field effects by gating have also attracted great

attention from the viewpoint of application, and progress towards next generation electronic devices are actively being made [3, 4].

Amongst the wide variety of properties found and studied in the atomically layered materials, one topic which has gained attention in recent years is the study of magnetism. Since 2016, studies of magnetism in atomically layered materials have started to gain attraction, where efforts have been made to both fabricate and elucidate the magnetic properties of atomically thin films using materials such as phosphorous trichalcogenides [5–8]. In such materials, the Raman spectroscopy had provided some indirect evidence of magnetism retained in the thin film counterpart. The breakthrough had occurred in 2017, with the reports of fabrication and characterisation of monolayer CrI_3 [9] and bilayer $CrGeTe_3$ [10]. In these reports, the temperature dependence of the magneto-optical Kerr effect (MOKE) was taken in order to directly observe the magnetic structure of the CrI_3 and $CrGeTe_3$ thin films. The MOKE signal as a function of the external applied field for monolayer, bilayer and trilayer CrI_3 thin films are shown as Fig. 1.1. In this measurement setup, the MOKE signals represent the out-of-plane magnetization, therefore providing direct and clear proof that the magnetism is clearly retained in CrI_3 thin films. A similar result was obtained for $CrGeTe_3$, where a finite MOKE signal was observed with applied fields of 0.075 T below $\sim$ 30 K.

This was a groundbreaking result for several reasons, in addition to the advantages and characteristics discussed above. The first reason is that, in general, it is not always trivial whether a long-range magnetic order is retained in the two-dimensional limit. For example, it is theoretically known that a long-range order does not exist in the two-dimensional limit for isotropic Heisenberg spins [11–13]. Therefore, a direct evidence of the long-range magnetic order in atomically thin magnetic films was an intriguing experimental finding from the perspective of the low-dimensional magnetism. The second reason was the change of the magnetic properties in the thin film counterpart.

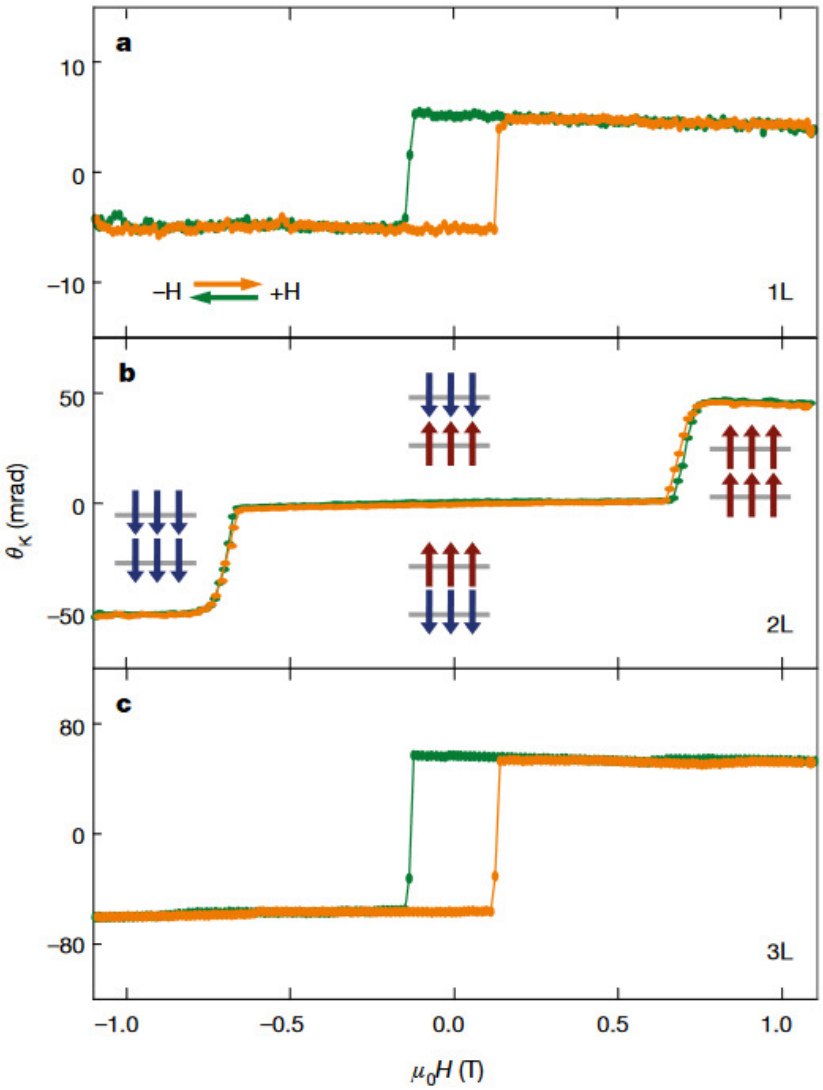

FIGURE 1.1: Magneto-optical Kerr effect signals of (a) monolayer, (b) bilayer, and (c) trilayer CrI_3 thin films. This figure is reproduced from Reference. [9] with permission from Springer Nature.

For example, emergence of an antiferromagnetic state was found only in the bilayer structure for CrI_3, which was otherwise found to be ferromagnetic in the monolayer, trilayer, and bulk counterpart. These results stress the fact that the magnetism in the thin films can often inherently change from that of the bulk sample. These reports have since then sparked significant interest in the study of atomically layered magnetic materials, from the viewpoints of the fundamental study of low-dimensional magnetism and also of the exploration of magnetic materials with novel properties unique to the thin film counterpart, which could be useful in future magnetic devices.

Meanwhile, it is important to note that the field of atomically layered magnetic materials is still a young and emerging field, with large room for exploration. In particular, the electrical transport of such magnetic thin films is a field which has not been extensively studied. This is a missed opportunity, since it is known that unique electrical transport properties can be observed in materials where the conduction electrons are coupled to the magnetic order. For example, coupling of the conduction electrons and exotic, non-coplanar magnetic structure can often lead to unique transport phenomena, such as the topological [14] or unconventional anomalous Hall effect [15, 16]. The study of electrical transport in atomically layered magnetic materials provides information on the electrical and magnetic properties of the thin films, and also explores novel transport properties in the atomically thin magnets, which could be useful in device applications.

With these motivations in mind, we have focused on the investigation of electrical transport properties in atomically layered antiferromagnetic materials with high electrical mobility. This is because rather than a simple ferromagnetic structure, exotic magnetic structures can be expected in an antiferromagnetic material. Furthermore, the high mobility could be useful in future device applications, such as spin transport devices. In the next section, we introduce the two magnetic materials studied in this thesis, namely the

rare-earth antiferromagnet $CeTe_3$ and the triangular lattice antiferromagnet Ag_2CrO_2.

1.2 Rare-earth antiferromagnet $CeTe_3$

$CeTe_3$ is an atomically layered material which belongs to the family of rare-earth tritellurides RTe_3 (R = Lanthanoid) [17]. While this family of materials had initially been extensively studied from the viewpoint of charge density wave (CDW) formation [18, 19] and high-pressure induced superconductivity [20], it has recently also gained attraction in the field of magnetism. In this section, we will discuss the unique electrical and magnetic properties of $CeTe_3$.

1.2.1 Electrical properties of $CeTe_3$

First, we will discuss the electronic properties of $CeTe_3$. The crystal structure of $CeTe_3$ is shown in Fig. 1.2. It has a weakly orthorhombic structure in the space group *Cmcm*, confirmed by transmission electron microscopy and X-ray diffraction measurements [21–23]. The crystal structure consists of CeTe slabs which are responsible for its magnetism, separated by two Te layers weakly bonded through the van-der-Waals force, allowing fabrication of thin films through the scotch tape method.

One of the unique electrical properties of $CeTe_3$ is its extremely high mobility. In the family of rare-earth tritellurides, the conduction is entirely dominated by the Te layers. This can be well described through an appropriate tight-binding model [21, 25, 26], in which the Te $5p_x$ and $5p_z$ orbitals form the dominant conduction band [26, 27]. The hopping parameters of the p_x and p_z orbitals, shown in the schematic image in Fig. 1.3(a), have been measured experimentally as $t_{||} \sim 1.8$ eV and $t_{\perp} \sim 0.35$ eV, which agree well with theoretical estimations of $t_{||} \sim 2.0$ eV and $t_{\perp} \sim 0.37$ eV [18, 27, 28]. The wide band

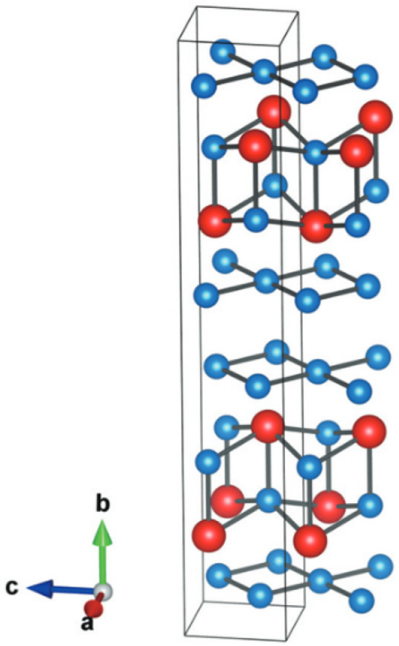

FIGURE 1.2: Crystal structure of $CeTe_3$. The red and blue spheres denote Ce and Te, respectively. This figure is reproduced from Reference. [24] with the permission of AIP Publishing.

formed by the p orbitals results in a small effective mass and a high carrier mobility in RTe_3. For example, $GdTe_3$ is known to possess one of the highest mobilities amongst the atomically layered magnets, where the mobility of the bulk counterpart is comparable to that of black phosphorous [29]. This has led to a renewed interest of RTe_3 as an atomically layered antiferromagnet with extremely high mobility in recent years.

Another unique electrical property is the CDW formation. From the tight-binding model of the Te-sheet, the Fermi surface can be constructed by considering the three-dimensional Brillouin zone occupied by the Te bilayers, as shown in Fig. 1.3(b). Some parts of the Brillouin zone behaves as a quasi-one-dimensional Fermi surface, which results in a formation of CDW states in the rare-earth tritellurides [18, 19, 21, 30]. For $CeTe_3$, it is known to transition to a CDW state well above room temperature, even above $\sim$500 K [31]. This results in a drastic reconstruction of the Fermi surface and therefore a complex

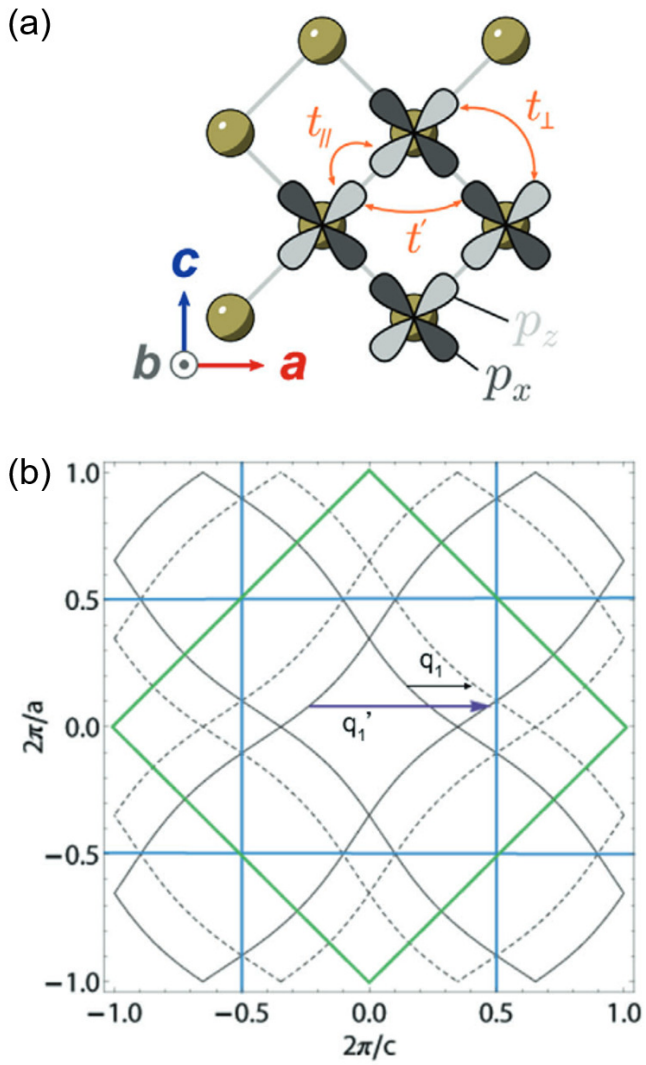

FIGURE 1.3: (a) Schematic image of one of the Te layers in RT_3, with the p-orbitals responsible for the electrical conduction. (b) Fermi surface of the Te monolayer (two-dimensional (2D) Brillouin zone: green line) and the Te bilayer (three-dimensional (3D) Brillouin zone: blue line). The arrows represents the CDW wavevector. Solid lines are the Fermi surface for the 2D Brillouin zone, and dotted lines are the Fermi surface for the 3D Brillouin zone. This figure is reproduced from Reference. [17] under the Creative Commons CC BY License https://creativecommons.org/licenses/by/4.0/.

Fermi surface structure, which has been studied extensively through positron annihilation [19] and angle-resolved photoemission spectroscopy (ARPES) measurements [18, 32]. Although the CDW itself has unique effects on the electrical transport properties such as the zero field resistivity [30, 33], CDW sliding [34, 35], and linear magnetoresistance [36], the coexistence of CDW and antiferromagnetic order is especially intriguing. While the coexistence of CDW and magnetic order is rare, previous reports on electrical transport in such materials have observed the emergence of unique phenomena such as the anomalous Hall effect [37]. This material is a good test-bed for the investigation of novel transport phenomena originating from competition and coupling of different ordered states.

1.2.2 Magnetic properties of $CeTe_3$

In terms of its magnetic properties, $CeTe_3$ has two antiferromagnetic transitions at low temperatures of $T_{N1} \approx 3.0$ K and $T_{N2} \approx 1.2$ K. The temperature dependences of magnetic susceptibility and heat capacity are shown in Fig. 1.4 [38]. As evident from the anisotropy in the magnetic susceptibility with respect to the crystallographic axis, the magnetic moments have a strong in-plane easy axis. The effective magnetic moments obtained from the Curie-Weiss law is consistent with the theoretical effective magnetic moment of $2.54\mu_B$ for a free Ce^{3+} ion [22], indicating that the $4f$ orbitals are responsible for the magnetism. At T_{N1}, the magnetic susceptibility shows a small kink, while the heat capacity shows a broad hump. The kink structure of the susceptibility suggests that this magnetic transition is from a paramagnetic state to an antiferromagnetic state, and the small amplitude of the kink suggests that this magnetic state is not a simple antiferromagnetic state but rather a helical or incommensurate sort. The broad hump of the heat capacity may be related to the low-dimensional character of $CeTe_3$, although

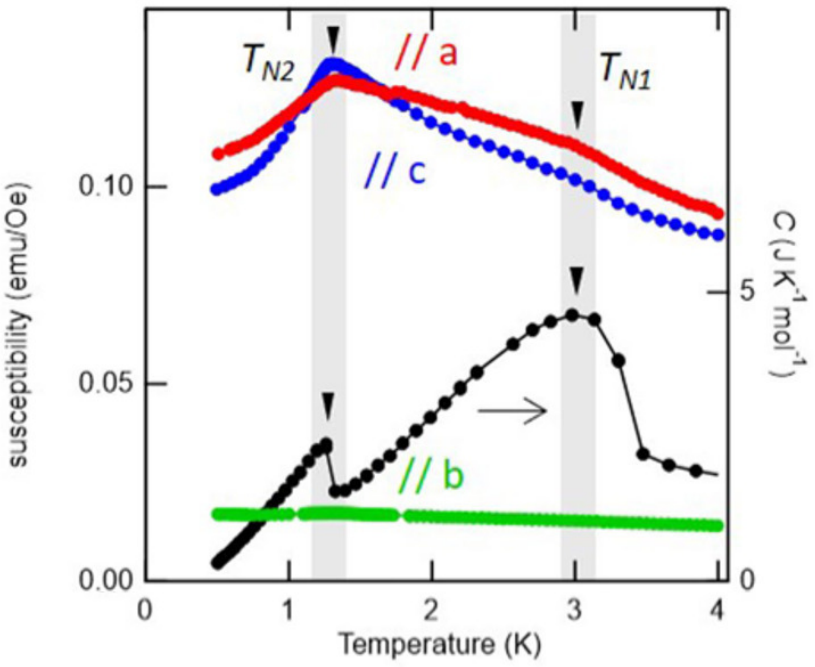

FIGURE 1.4: (Left axis) Temperature dependence of magnetic susceptibility of $CeTe_3$ along the *a*- and *c*-axes (in-plane direction) and the *b*-axis (perpendicular direction). (Right axis) Temperature dependence of heat capacity measurements of $CeTe_3$ bulk sample. This figure is reproduced from Reference. [38] under the Creative Commons CC BY License https://creativecommons.org/licenses/by/4.0/. Figure axes have been edited for clarity.

its details are still unknown [23]. At T_{N2}, the heat capacity measurement shows a discontinuous jump, indicating a typical second-order transition. The magnetic susceptibility shows a large kink structure, indicating the transition from the incommensurate antiferromagnetic state to a second long-range antiferromagnetic state at this temperature.

The magnetization below T_{N2} is shown in Fig. 1.5(a). This measurement also confirms the strong in-plane anisotropy of the magnetization, with a spin-flop type magnetization switching observed along the *c*-axis at roughly 1 T. At high enough fields, the in-plane magnetization saturates at roughly $1.0\mu_B$/Ce-atom, which is consistent with the magnetic moment of the calculated $J = 5/2$ ground state for the $4f$ moments $\sim 0.87\mu_B$ [22].

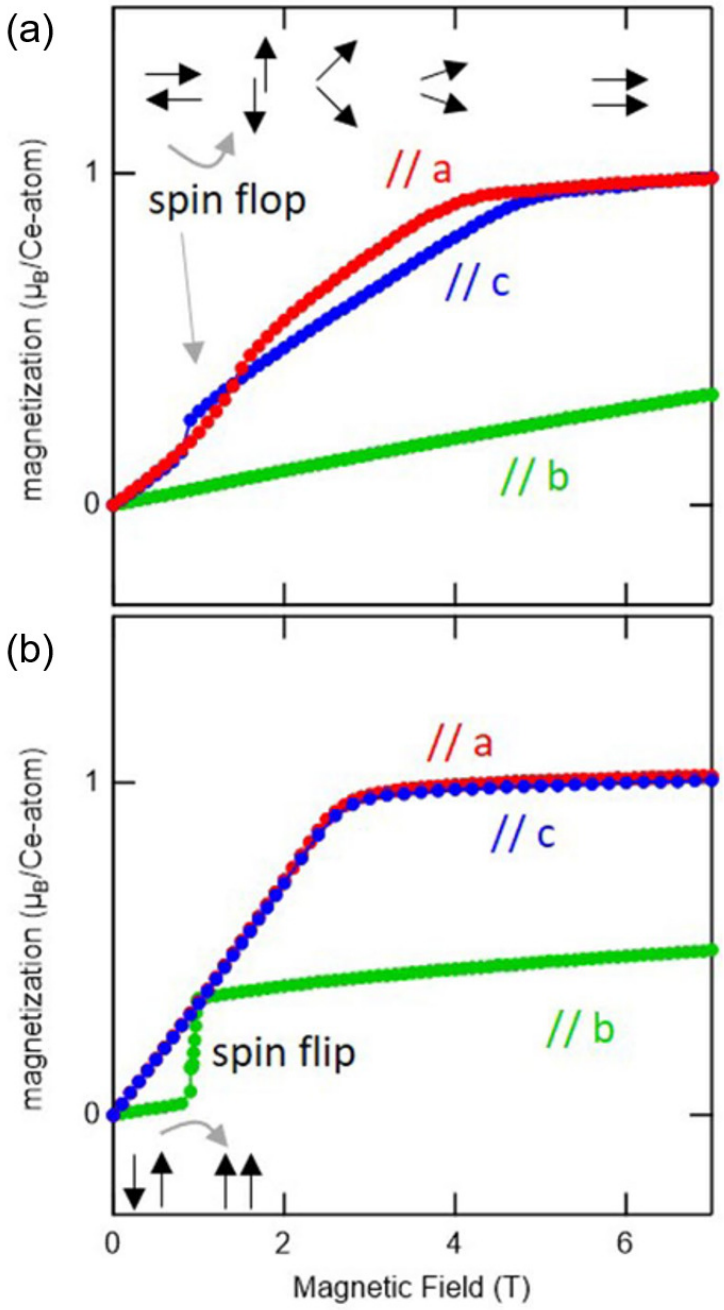

FIGURE 1.5: Mangetization measurements for (a) $CeTe_3$ and (b)$CeSeTe_2$ at 0.5 K. This figure is reproduced from Reference. [38] under the Creative Commons CC BY License https://creativecommons.org/licenses/by/4.0/.

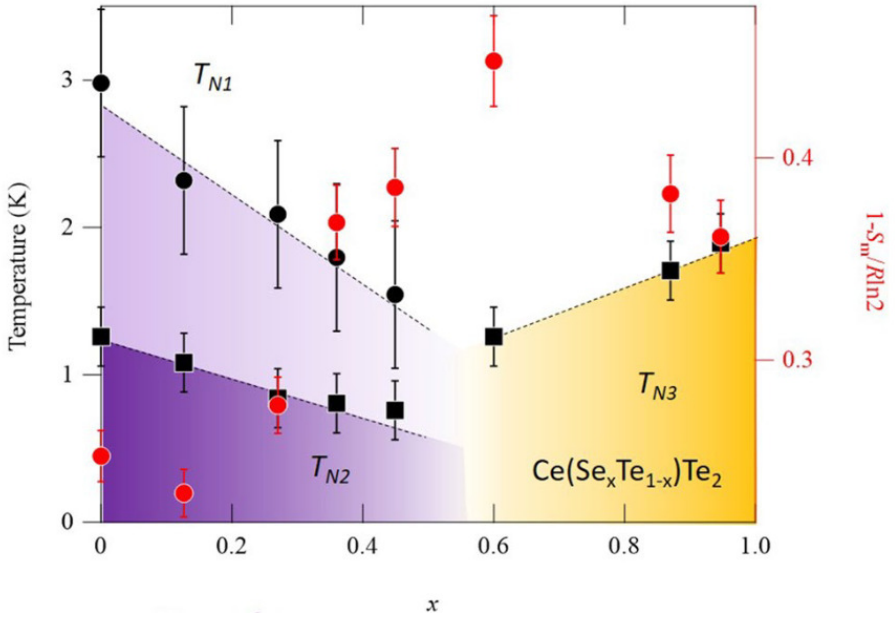

FIGURE 1.6: Phase diagram as a function of doping concentration x for $Ce(Se_xTe_{1-x})Te_2$. This figure is reproduced from Reference. [38] under the Creative Commons CC BY License https://creativecommons.org/licenses/by/4.0/.

In addition to the strong in-plane anisotropy of the magnetization, an out-of-plane anisotropy can be induced by doping Se atoms. Okuma *et al*. [38] investigated the effect of systematic doping of Se into $CeTe_3$, which is selectively substituted for the Te atoms in the CeTe slab structure. Through heat capacity, susceptibility and magnetization measurements, they found that the in-plane anisotropy was suppressed with increasing the Se concentration. At a critical concentration of $x \sim 0.6$ for $Ce(Se_xTe_{1-x})Te_2$, they observed a new magnetic phase which has a spin flip-type magnetization switching along the b axis of the material, as shown in the magnetization measurement of $CeSeTe_2$ in Fig. 1.5(b). The phase diagram as a function of Se concentration is shown in Fig. 1.6. While this study demonstrates a systematic control of magnetic anisotropy in $CeTe_3$, it also indicates that fluctuations of the magnetic moments may be important in the characterization of the magnetic structure of $CeTe_3$, which is likely modulated through the additional chemical pressure from Se doping.

Finally, regarding the relationship between the magnetic structure and the conduction electrons, the most unique property of $CeTe_3$ amongst the family of RTe_3 is that it is the only material in which the Ruderman-Kittel-Kasuya-Yosida (RKKY) interaction is the dominant interaction, whereas all other RTe_3 interact via a direct exchange or super-exchange interaction [22]. This means that a strong coupling can be expected between the conduction electrons and the magnetic order, and novel electrical transport phenomena which are sensitive to the magnetic state can be expected. It is also important to stress that the studies mentioned above are mostly performed in the bulk counterpart, likely due to the high reactivity to air and the difficulty in fabrication of measurable thin-film devices. Therefore, the magnetic and electronic properties of the thin films are still largely unexplored, and unique effects owing to the high mobility in $CeTe_3$ are expected to be observed also in the thin-film counterpart.

1.3 Triangular lattice antiferromagnet Ag_2CrO_2

In this section, we discuss the background on the triangular lattice anttiferromagnet (TAFM), Ag_2CrO_2. In this material, a unique magnetic ordering known as the partially disordered structure is realized owing to the frustration in the system. Furthermore, it is one of the few TAFMs to show metallic behavior, allowing studies of electrical transport phenomena in such an exotic magnetic structure. In this section, a brief introduction about the topics related to TAFMs is given, followed by the description of the magnetic and electrical properties of Ag_2CrO_2.

1.3.1 Triangular lattice antiferromagnet and frustration

A study of TAFM is an important stream in the field of magnetism, well known for the realization of various exotic magnetic structures. This comes from a concept known as frustration, where the magnetic system does not possess a trivial ground state due to competing interactions. A simple example of classical spins placed on a two-dimensional triangular lattice is shown in Fig. 1.7. In this example, if the placed spins are two-dimensional Ising spins, a trivial ground state does not exist due to the competing antiferromagnetic interactions. In reality, such a degeneracy of the ground state implies a very large fluctuation and instability of the ordered magnetic moments, leading to novel magnetic phenomena such as quantum spin liquids [39–41]. Moreover, the ground state degeneracy can be lifted in the presence of small anisotropy in the system, such as the anisotropy in the crystal symmetry. This can lead to observation of exotic magnetic states which may be unexpected from a simplified consideration of the symmetry of the system.

Although there are many theoretical studies to elucidate the magnetic structures of various TAFMs, we will briefly explain the Ising TAFM model, which is useful in understanding the magnetic structure of Ag_2CrO_2. Such

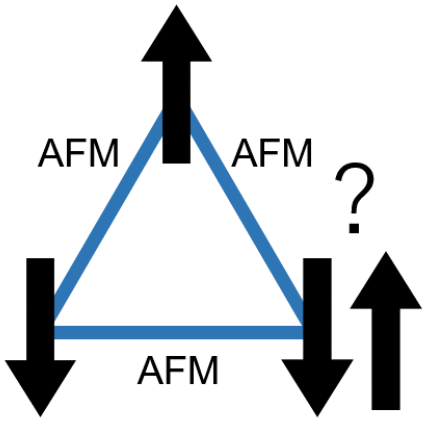

FIGURE 1.7: Schematic image of frustration induced in a triangular lattice spin system.

a model had first been studied from the viewpoint of hexagonal ABX_3 type compounds [42]. In particular, we focus on the simulation performed by Mekata [43] and Takagi [44]. Mekata first considered the triangular Ising model with an antiferromagnetic neighbour interaction $J < 0$ and also a ferromagnetic next-nearest neighbour interaction $J' > 0$. In such a case, the triangular lattice is divided into three sub-lattices as shown in Fig. 1.8(a). The Hamiltonian for the l-th sub-lattice can be written in the molecular field approximation as

$$\mathcal{H} = -6J(\langle S_m \rangle + \langle S_n \rangle) \sum_i S_l^i - 12J' \langle S_l \rangle \sum_i S_l^i - g\mu_B H \sum_i S_l^i, \qquad (1.1)$$

where subscripts l, m and n specify the sub-lattice and i is the unit cell. Here, g is the g-factor and μ_B is the Bohr magneton. The relative magnetization of the sub-lattice $\langle \sigma_l \rangle$ can be obtained by substituting S_l for $S\sigma_l$ as

$$\langle \sigma_l \rangle = \tanh\{\beta(\alpha \langle \sigma_l \rangle + \langle \sigma_m \rangle + \langle \sigma_n \rangle + \gamma), \qquad (1.2)$$

where $\alpha = 2J'/J$, $\beta = 6S^2J/k_BT$, and $\gamma = g\mu_B H/6SJ$. Here, k_B is the Boltzmann constant. Equation (1.2) can be solved numerically as a function of α, β and γ, from which the stable state was obtained. From the calculations,

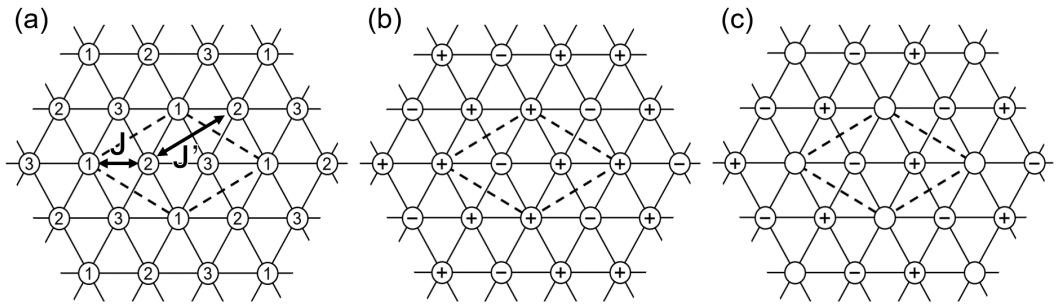

FIGURE 1.8: Schematic images of (a) the sub-lattice structure of the two-dimensional Ising TAFM system, (b) ferrimagnetic structure, and (c) the partially disordered antiferromagnetic structure.

it was shown that in the range of $0 > \alpha > -0.8$, there exists a second-order transition from a ferrimagnetic state (Fig. 1.8(b)) to an anitferromagnetic state where one out of three spins are completely disordered (Fig. 1.8(c)). This state is what is now known as the "partially diordered" (PD) state. In 1995, further work on the PD state in a triangular lattice was performed by Takagi and Mekata [44]. In this theoretical study, Monte Carlo simulations were performed to model the ground states of Ising triangular lattice spin systems with third nearest neighbour interactions in addition to the next nearest neighbour interaction discussed above. The Hamiltonian is given as

$$\mathcal{H} = -J_1 \sum_{\text{1st } n} \sigma_i \sigma_j - J_2 \sum_{\text{2nd } n} \sigma_i \sigma_j - J_3 \sum_{\text{3rd } n} \sigma_i \sigma_j, \tag{1.3}$$

where σ_i takes values of ± 1, and J_1, J_2, J_3 are the first, second, and third nearest neighbour interactions, respectively. The summation is taken as shown in Fig. 1.9. For the calculations, $J_1 < 0$ is assumed, and other interactions are scaled with respect to $|J_1|$ as

$$\tilde{J}_2 = J_2/|J_1|, \quad \tilde{J}_3 = J_3/|J_1|, \quad \tilde{T} = k_B T/|J_1| \tag{1.4}$$

in order to make them dimensionless. Although no PD ground state was

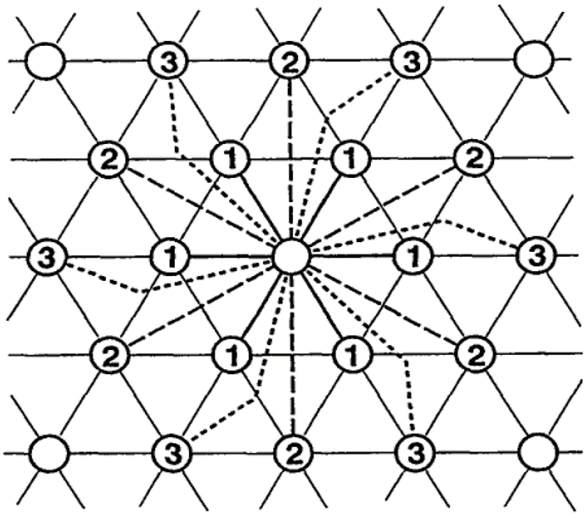

FIGURE 1.9: Schematic image for the summation took in the calculation for Eq. 1.3. This figure is reproduced from Reference. [44] with permission from The Physical Society of Japan ©(1995).

observed for $T = 0$ K, multiple PD states of 3, 5, and 9 sub-lattices were obtained at a finite temperature of $\tilde{T} = 0.75$, as $\tilde{J}_2$ and $\tilde{J}_3$ were varied (see Fig. 1.10). Therefore, it was shown that various types of PD states could occur in a TAFM with strong further-neighbour interactions.

Experimentally, early works of PD states can be found in the $ACoX_3$ compounds such as $CsCoCl_3$ [43, 45] and $CsCoBr_3$ [46]. Since then, various materials have been found to possess the unique PD state, such as the one-dimensional oxides [47–52] or multiferroic materials [53–55]. Meanwhile, metallic TAFM which possess the PD state are still limited to certain material groups such as the f-electron systems [56–64], and further works on the novel transport effects arising from the exotic magnetic structure are anticipated. In the next subsection, we will discuss the magnetic and electrical properties of Ag_2CrO_2, which is a metallic TAFM with a 5-PD state below its antiferromagnetic transition temperature.

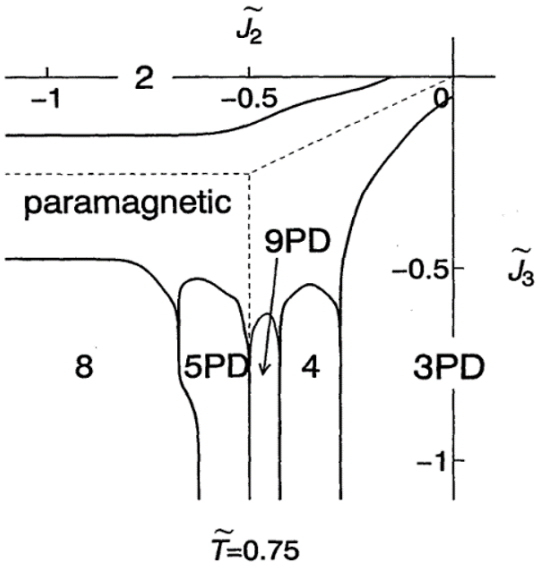

FIGURE 1.10: The phase diagram of the ground state for TAFM in the finite temperature regime. This figure is reproduced from Reference. [44] with permission from The Physical Society of Japan ©(1995).

1.3.2 Partially disordered state of Ag_2CrO_2

In this subsection, we outline the magnetic property of Ag_2CrO_2. The crystal structure of Ag_2CrO_2 is shown in Fig. 1.11(a). It consists of alternating layers of the CrO_2 layer and the Ag_2 conductive layer. The magnetic properties originate from the Cr^{3+} orbitals with a nearly fully occupied high spin state (t_{2g}^3), which are placed in a triangular lattice configuration. From the X-ray diffraction [65] and the neutron powder diffraction [66], Ag_2CrO_2 is found to possess a trigonal structure ($P\bar{3}m1$: Fig. 1.11(b)) with $a = 2.9298$ Å and $c = 8.6637$ Å at 200 K, and a monoclinic structure ($C2/m$: Fig. 1.11(c)) below its antiferromagnetic transition temperature.

In the specific heat measurement [65] shown in Fig. 1.12, a sharp peak is observed at around 24 K, which corresponds to the antiferromagnetic transition temperature T_N. The magnetic transition is also clear from the temperature dependence of the magnetic susceptibility [65], shown in Fig. 1.13. At high temperatures, the magnetic susceptibility (M/H) shown in the inset of

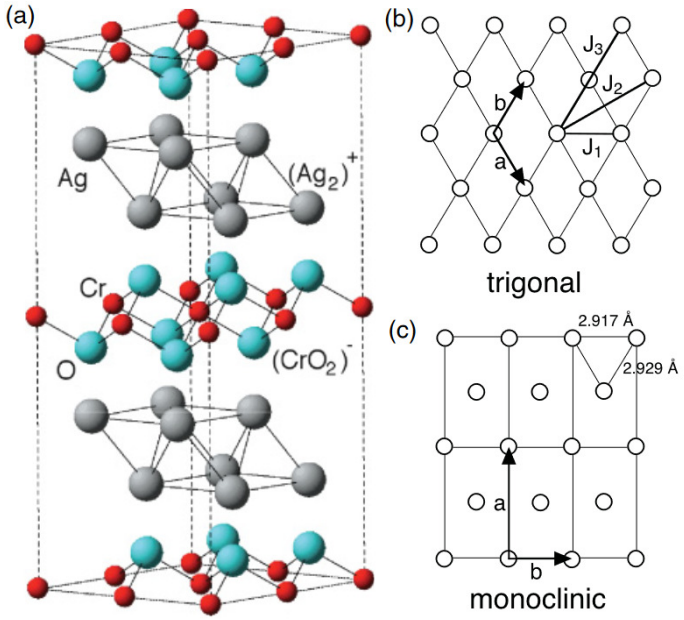

FIGURE 1.11: (a) Crystal structure of Ag_2CrO_2, and schematic images of the (a) trigonal crystal symmetry and (b) monoclinic crystal symmetry. The figure is reproduced with permission from Reference. [66] Copyright 2023 by the American Physical Society.

Fig. 1.13(a) obeys the Curie-Weiss law, from which the effective moment p_{eff} and Weiss temperature θ_W are estimated to be 3.55 and -97 K, respectively. At low temperatures, the magnetic susceptibility abruptly increases at 24 K, indicating a magnetic transition. Meanwhile, the magnetization of Ag_2CrO_2 shown in Fig. 1.13(b) shows a linear magnetization at 50 K, and a hysteresis loop of $\sim 0.08\mu_B$/Cr at 2 K. Noting that the magnetization depicted in Fig. 1.13(b) is normalized by the fully saturated moment of the Cr^{3+} state $\sim 3\mu_B$, the magnetic hysteresis observed at 2 K corresponds to about 8.5% of the full saturated moment. Furthermore, the magnetization only reaches about 12% of the fully saturated moment even at a high applied field of 7 T. These results indicate that the ground state of Ag_2CrO_2 has a nontrivial antiferromagnetic order with some weak ferromagnetic components.

In order to gain information on the detailed magnetic structure, neutron

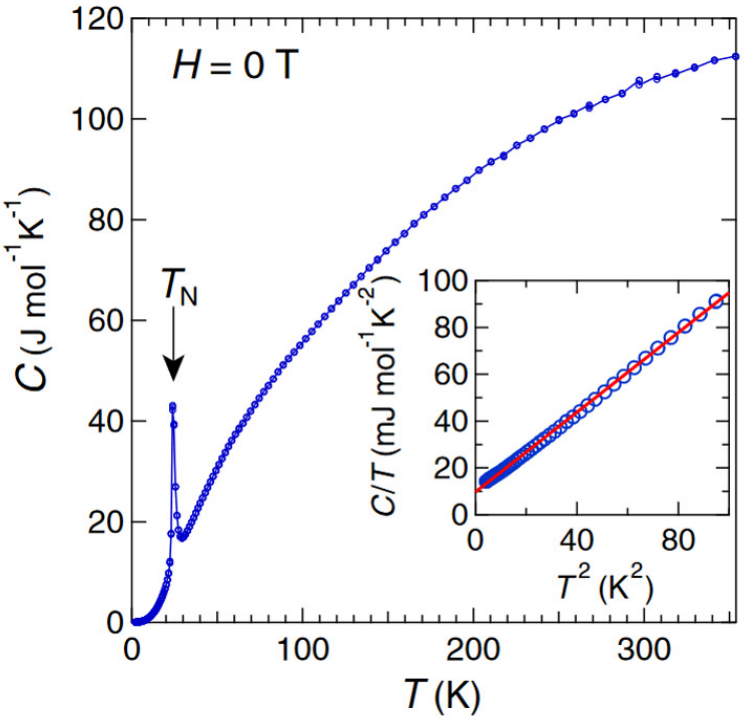

FIGURE 1.12: Specific heat capacity measurement of Ag_2CrO_2. This figure is reproduced from Reference. [65] with permission from The Physical Society of Japan ©(2011).

diffraction [66] has also been performed for the powder sample. In the magnetic Bragg reflections below T_N shown in Fig. 1.14(a), magnetic reflections with $\left(\frac{1}{5}, \frac{1}{5}, 0\right)$ and $\left(\frac{4}{5}, \frac{1}{5}, 1\right)$ are observed, indicating that the magnetic structure has a 5 sub-lattice unit cell with a ferromagnetic moment along the c-axis. The temperature dependence of the magnetic Bragg peak intensity developed abruptly below T_N, while the nuclear Bragg peak intensity dropped below T_N (see the inset of Fig. 1.14(b)), indicating that the magnetic and structural transitions occur simultaneously at T_N. Based on these measurements, the most reasonable spin arrangement for Ag_2CrO_2 is expected to be a 5 sublattice PD state, with an up-down-up-down-disordered... structure along the b-axis shown in Fig. 1.15, which is realised with the structural phase transition. It is important to note that similar results have been obtained by μSR measurements performed by Sugiyama *et al*. [67].

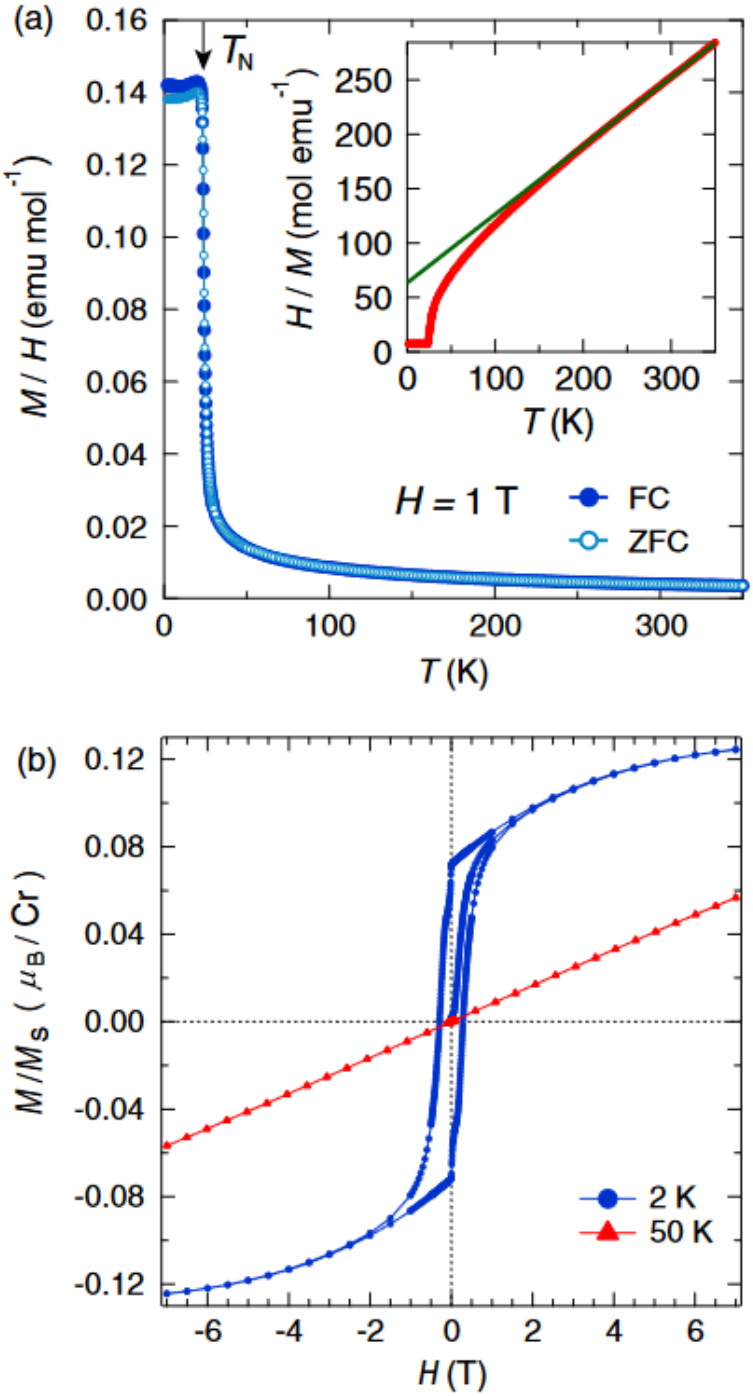

FIGURE 1.13: (a) Temperature dependence of the magnetic susceptibility of Ag_2CrO_2. (b) Magnetization normalized by the full saturation moment ($3\mu_B$) against $\mu_0 H$ at $T = 2$ and 50 K. This figure is reproduced from Reference. [65] with permission from The Physical Society of Japan ©(2011).

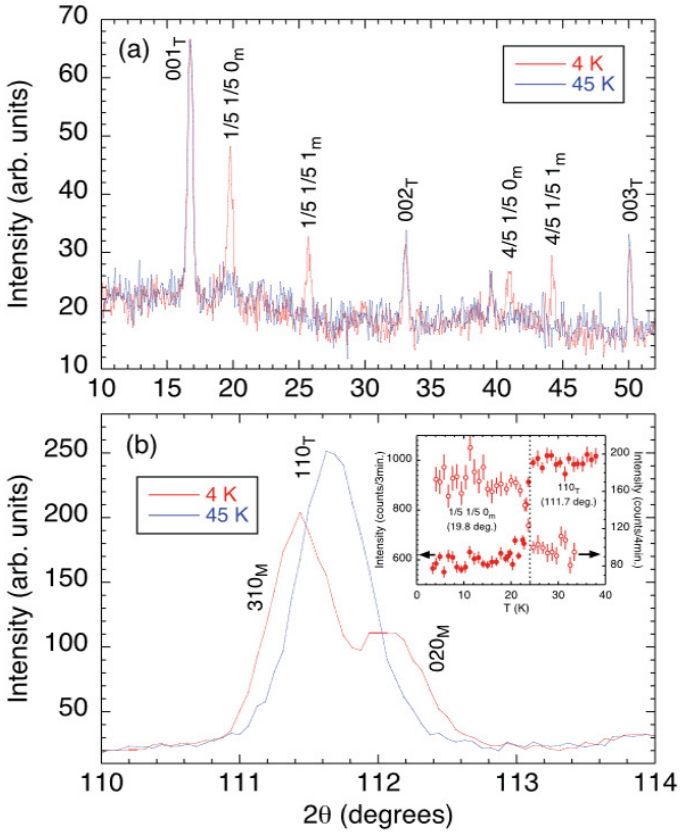

FIGURE 1.14: Neutron diffraction patterns in Ag_2CrO_2 at $T = 4$ and 45 K. (a) Data for low scattering angles, where some magnetic Bragg peaks can be observed. (b) Data for high scattering angles, which show the splitting of nuclear Bragg peaks below T_N. The inset shows the temperature dependence for the magnetic and nuclear Bragg peak intensities. The figure is reproduced with permission from Reference. [66] Copyright 2023 by the American Physical Society.

While Ag_2CrO_2 was shown to possess a 5 sub-lattice PD structure, a couple of questions still remain on its detailed magnetic properties, such as the origin of the finite magnetization below T_N, and the magnetic structure at a high applied field of 7 T.

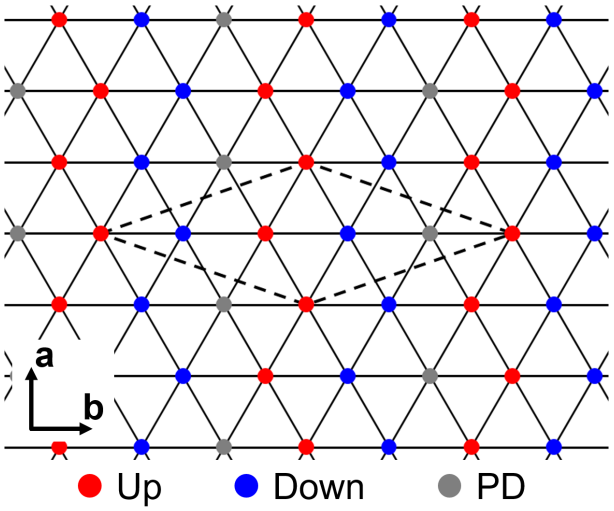

FIGURE 1.15: Schematic image of the 5 sub-lattice PD structure of Ag_2CrO_2. The dotted line indicates the magnetic unit cell.

1.3.3 Electrical properties of Ag_2CrO_2

As mentioned in the previous subsection, the crystal structure of Ag_2CrO_2 possesses a highly conductive Ag_2 layer, which allows electrical transport measurements to be performed. A typical temperature dependence of resistivity under $H = 0$ and 9 T for poly-crystalline bulk samples are shown in Fig. 1.16 [65]. This material has a metallic conductivity owing to the Ag-5*s* band. Furthermore, there is a large drop in resistivity at T_N, which is most likely due to the suppression of paramagnetic scattering below the magnetic transition temperature.

The magnetoresistance (MR) and the Hall effect for the bulk poly-crystalline samples have been investigated by Kida *et al*. [68]. The temperature dependence of the MR is shown in Fig. 1.17. While a large linear positive MR was observed at temperatures well below T_N, the MR slope decreases as temperature is increased, with an emergence of negative MR around T_N. This is likely due to the large fluctuations of the magnetic moments, which leads to paramagnetic scattering at zero magnetic field and the emergence of the negative MR in the vicinity of T_N. Meanwhile, a non-linear Hall resistivity was

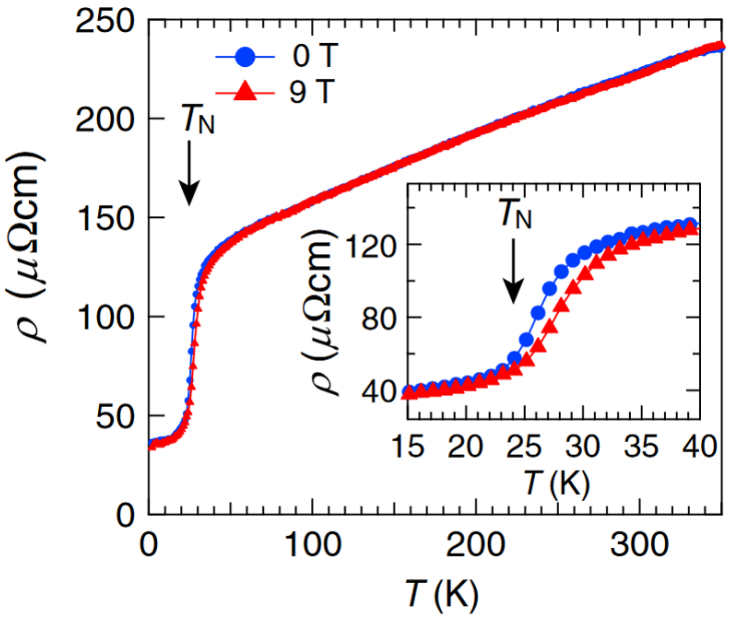

FIGURE 1.16: Temperature dependence of resistivity for poly-crystalline Ag_2CrO_2. This figure is reproduced from Reference. [65] with permission from The Physical Society of Japan ©(2011).

observed for all temperatures, as shown in Fig. 1.18(a). The Hall resistivity ρ_H in itinerant ferromagnets can be expressed as

$$\rho_H = R_0 \mu_0 H + R_s M, \tag{1.5}$$

where R_0 is the ordinary Hall coefficient, μ_0 is the vacuum permeability, R_s is the anomalous Hall coefficient and M is the magnetization. As evident from Eq. (1.5), ρ_H should be proportional to M if we assume that the R_0 component is very small, which is a valid assumption in Ag_2CrO_2 due to the large carrier concentration. The graph of ρ_H against M is shown for different temperatures in Fig. 1.18(b). ρ_H deviates from the M-linear relationship in the vicinity of the transition temperature. This indicates some unconventional anomalous Hall behaviour, which is induced only in the vicinity of T_N.

So far, the discussed experimental results are from poly-crystalline samples, since the bulk sample is inherently poly-crystalline from synthesis. In

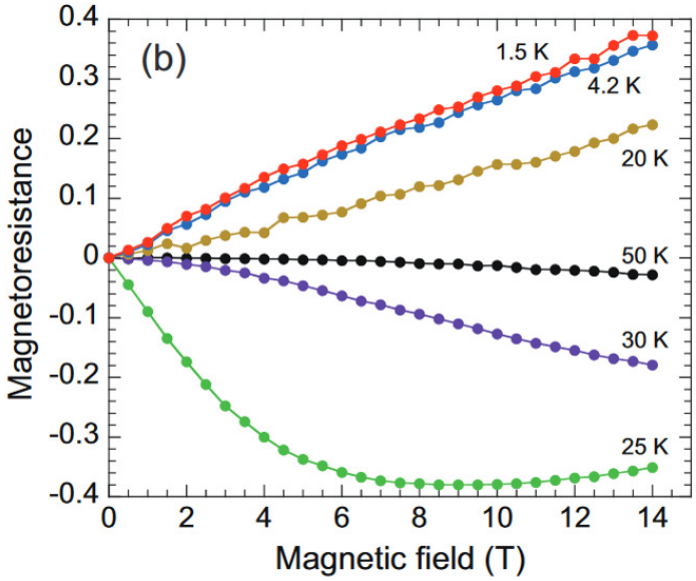

FIGURE 1.17: Magnetoresistance of poly-crystalline Ag_2CrO_2 at different temperatures. This figure is reproduced from Reference. [68] under the Creative Commons CC BY-NC-ND License https://creativecommons.org/licenses/by-nc-nd/4.0/.

2018, Taniguchi *et al*. [69] had shown that nearly mono-crystalline micrometer-scale flakes could be obtained through the mechanical exfoliation method. Through this method, Ag_2CrO_2 samples with extremely high crystallinity could be obtained, and electrical transport measurements could be performed through nanofabrication. This also allows investigation of the anisotropy in the electrical transport with respect to the crystallographic axis, since the exfoliated flakes are transferred onto the substrate along the stacking direction (c-axis).

Following the fabrication of high quality Ag_2CrO_2 thin films, the MR of the Ag_2CrO_2 thin film devices up to $H = 1$ T in the temperature range from 5 to 36 K had been investigated, as shown in Fig. 1.19 [70]. The unique point of this measurement is the butterfly-shaped hysteresis in the MR, which was observed only in the vicinity of T_N, and only when the magnetic field was applied along the c-axis. Such an MR hysteresis had not been reported in

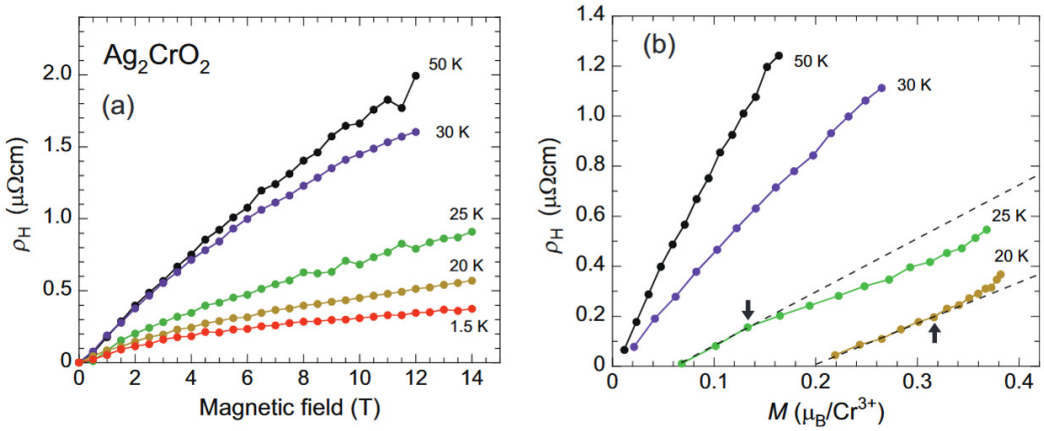

FIGURE 1.18: (a) Hall resistivity against the applied magnetic field at notable temperatures. (b) ρ_H against M for notable temperatures. Arrows indicate points where the Hall resistivity deviates from the linear relation. This figure is reproduced from Reference. [68] under the Creative Commons CC BY-NC-ND License https://creativecommons.org/licenses/by-nc-nd/4.0/.

the bulk counterpart, which is directly related to the crystallinity of the measured sample. This behavior would be caused by the large fluctuations and switching of the disordered magnetic moments, suggesting a large coupling between the PD state and the conduction electrons. These results of the thin film devices indicate that further unique transport phenomena could still be found in the thin film Ag_2CrO_2, such as the unique anomalous Hall effects in the vicinity of T_N which were pointed out by Kida *et al*. [68] from the polycrystalline bulk measurements.

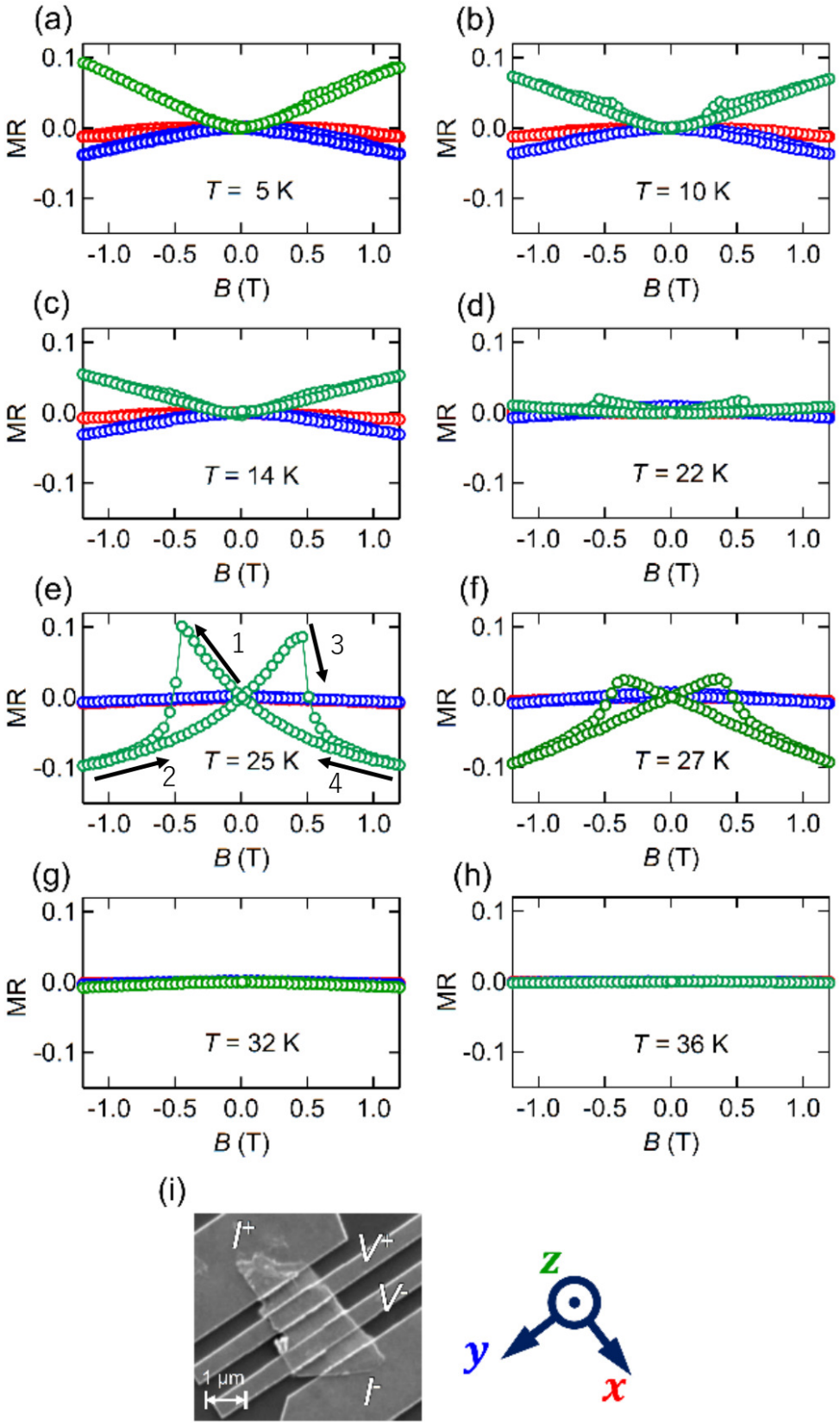

FIGURE 1.19: (a)-(h) Magnetoresistance of a Ag_2CrO_2 thin-film device at notable temperatures. Arrows in (e) shows the magnetic field sweep order. (i) The scanning electron microscope image of the measured device. This Figure is reproduced from Reference. [71] with permission of the author.

1.4 Quantum oscillations of high mobility materials

In this section, we outline the concept of quantum oscillation, which is related to the electrical transport measurements of a rare-earth antiferromagnet $CeTe_3$. Quantum oscillation is a generalized name for phenomena where physical quantities such as heat capacity, magnetization and resistance of a material oscillate as a function of the externally applied magnetic field. One of the most commonly observed quantum oscillations is the Shubnikov-de-Haas (SdH) effect, where an oscillation of resistance is observed as a function of the external field. Some of the important characteristics of the SdH effect are outlined in this section.

1.4.1 Qualitative description of the SdH effect

This subsection will first provide a qualitative picture for the origin of the SdH effect (also known as the SdH oscillation). When a magnetic field is applied to the electron, the electron goes through a cyclotron motion. This leads to a quantization of allowed orbits with quantized energy, known as Landau levels. The formation of quantized orbits is the origin of SdH oscillations.

A schematic image of the origin of SdH oscillation is shown in Fig. 1.20. For simplicity, we will first ignore any z component and consider the motion of free electrons in two-dimension (2D). Figure 1.20(a) shows a schematic image of the wavenumber space (k space) of the free electron in a 2D system. The red circle is the Fermi surface (or Fermi line in the case of 2D), and the dots are the allowed states of the electron. As shown, states are occupied as long as they are within the Fermi surface. The occupied and unoccupied states are represented with blue dots and grey dots, respectively. In reality,

References. [72] and [73] were useful for understanding the detailed origins of SdH effect.

the density of these allowed states is much more dense and thus appears continuous. The same k space under an external magnetic field is shown in Fig. 1.20(b). Here, the electron goes through a cyclotron motion, resulting in a quantization of allowed orbits. In Fig. 1.20(a), the allowed states were uniformly spread over the entire k space, but now it must lie on the quantized orbits indicated by the black solid lines shown in Fig. 1.20(b). As before, the occupied states are only ones which lie within the Fermi surface.

As the external magnetic field is increased, the radius of these orbits increases in the k space. At some point, the largest circle inside the Fermi surface (in Fig. 1.20(b), this is the the circle $n = 3$) becomes larger than the Fermi surface. Since electronic states cannot be occupied outside of the Fermi surface, the electrons will rearrange to occupy the states below the Fermi energy, resulting in an abrupt decrease in the occupied states near the Fermi surface. This leads to an abrupt change in the resistivity of the material, which is the fundamental cause of the SdH oscillation. In the next subsection, the quantitative description of this phenomena is discussed from the momentum of charged particles in a magnetic field, and shows that this oscillation is periodic to $1/B$. We will also discuss how this periodicity is related to the area of the Fermi surface.

1.4.2 Quantization of electron orbit under a magnetic field

The total momentum $\boldsymbol{p}$ of a charged particle in a magnetic field is given by

$$\boldsymbol{p} = \hbar \boldsymbol{k} + q\boldsymbol{A}, \tag{1.6}$$

where $\hbar$ is the reduced Planck's constant, $\boldsymbol{k}$ is the wavevector, q is the charge and $\boldsymbol{A}$ is the vector potential. The orbit of the charged particle in a magnetic

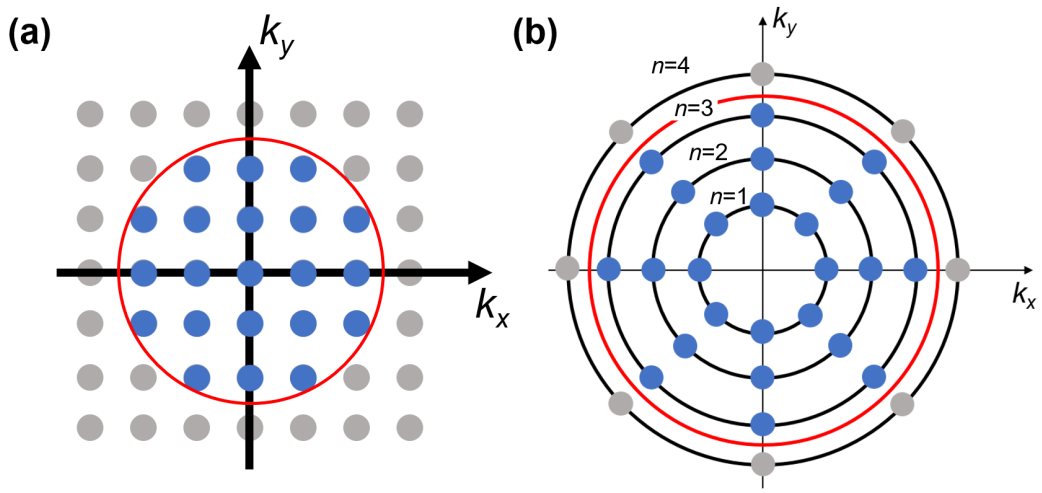

FIGURE 1.20: Schematic image of the 2D electron system. (a) k space of the 2D electron in the absence of magnetic field. The red curve is the Fermi surface. The blue dots represent occupied states, and grey dots represent unoccupied states. (b) k space under a magnetic field. The allowed electronic states become restricted to quantized orbits given as the black solid lines, represented by the quantum number n.

field is quantized by the Bohr-Sommerfeld relation

$$\oint \boldsymbol{p} \cdot d\boldsymbol{r} = (n + \gamma) 2\pi\hbar, \tag{1.7}$$

where n is an integer and γ is a phase correction term ($\gamma = 1/2$ for free electrons). Equation (1.6) can also be expressed as

$$\oint \boldsymbol{p} \cdot d\boldsymbol{r} = \oint \hbar\boldsymbol{k} \cdot d\boldsymbol{r} + q \oint \boldsymbol{A} \cdot d\boldsymbol{r}. \tag{1.8}$$

The equation of motion of the charged particle in a magnetic field is given as

$$\hbar \frac{d\boldsymbol{k}}{dt} = q \frac{d\boldsymbol{r}}{dt} \times \boldsymbol{B}, \tag{1.9}$$

which can be integrated with respect to time to give

$$\hbar \boldsymbol{k} = q\boldsymbol{r} \times \boldsymbol{B}. \tag{1.10}$$

A constant of integration is omitted here as it does not contribute to the final result. The first term on the right hand side in Eq. (1.8) is given as

$$\oint \hbar \boldsymbol{k} \cdot d\boldsymbol{r} = q \oint \boldsymbol{r} \times \boldsymbol{B} \cdot d\boldsymbol{r} = -q\boldsymbol{B} \cdot \oint \boldsymbol{r} \times d\boldsymbol{r} = -2q\Phi, \tag{1.11}$$

where Φ is the magnetic flux contained within the orbit in real space. Here, the scalar triple product is used as

$$\boldsymbol{a} \cdot (\boldsymbol{b} \times \boldsymbol{c}) = \boldsymbol{b} \cdot (\boldsymbol{c} \times \boldsymbol{a}), \tag{1.12}$$

for arbitrary vectors $\boldsymbol{a}$, $\boldsymbol{b}$ and $\boldsymbol{c}$, and the relation

$$\oint \boldsymbol{r} \times d\boldsymbol{r} = 2 \times (\text{area enclosed by the orbit}), \tag{1.13}$$

is also used. The second term on the right hand side in Eq. (1.8) can be written as

$$q \oint \boldsymbol{A} \cdot d\boldsymbol{r} = q \int (\nabla \times \boldsymbol{A}) \cdot d\boldsymbol{\sigma} = q \int \boldsymbol{B} \cdot d\boldsymbol{\sigma} = q\Phi, \tag{1.14}$$

with the application of the Stokes theorem and the vector potential relation $\nabla \times \boldsymbol{A} = \boldsymbol{B}$. Here $d\boldsymbol{\sigma}$ is the area element in real space. Therefore, the path integral in Eq. (1.8) can be rewritten as a sum of Eq. (1.11) and Eq. (1.14),

$$\oint \boldsymbol{p} \cdot d\boldsymbol{r} = -q\Phi = (n + \gamma)2\pi\hbar. \tag{1.15}$$

This means that the orbit of an electron is quantized in such a way that the magnetic flux through the orbit is

$$\Phi_n = A_n B = (n + \gamma)(2\pi\hbar/e), \tag{1.16}$$

where A_n is the area covered by the electron orbit in real space, and B is the magnetic field. Here, the charge is $q = -e$ where e is the elementary charge. The energies of the orbiting electrons are also quantized, which are known as Landau levels.

It is also useful to understand these quantized electron orbits in the k space. Equation (1.10) implies that a line element in real space Δr in the plane normal to $\boldsymbol{B}$ is related to Δk by $\Delta r = (\hbar/eB)\Delta k$. Thus, an area S_n in the k space is related to the area A_n in real space by

$$A_n = (\hbar/eB)^2 S_n. \tag{1.17}$$

It follows that

$$\Phi_n = A_n B = \left(\frac{\hbar}{e}\right)^2 \frac{1}{B} S_n = (n + \gamma)\frac{2\pi\hbar}{e}, \tag{1.18}$$

so the orbits are also quantized in the k space with the relation

$$S_n = (n + \gamma)\frac{2\pi e}{\hbar} B, \tag{1.19}$$

where S_n is the area covered by the electron orbit in the k space. Therefore, the area covered by the electron orbit in the k space increases as B is increased.

As stated in the previous subsection, an oscillation in resistivity is observed each time the electron orbit passes through the Fermi surface. Imagine a situation depicted in Fig. 1.21. Here, the orbit $n + 1$ has just passed over the Fermi surface, while the orbit n is still inside the Fermi surface and fully

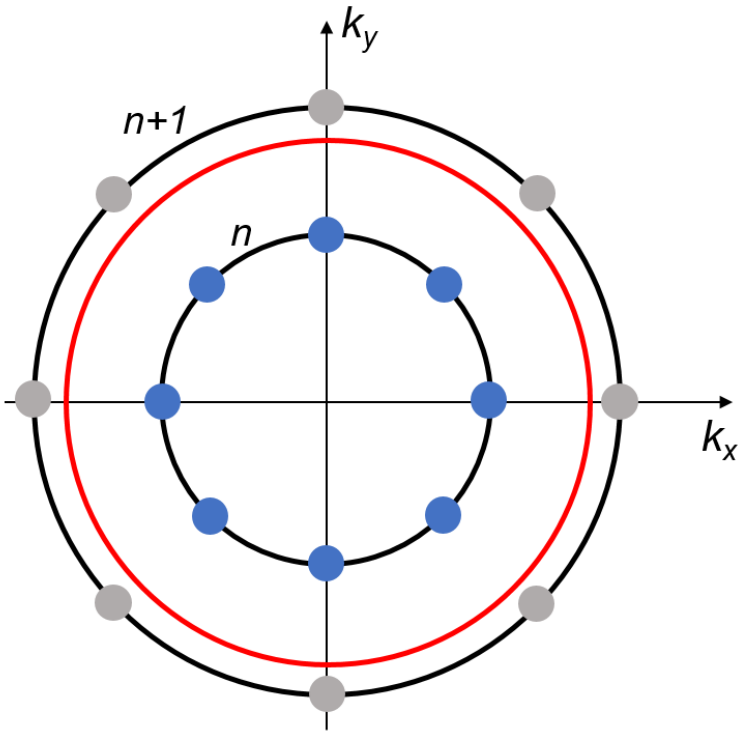

FIGURE 1.21: Schematic image of the orbits of n and $n+1$.

occupied. The area of the orbit for $n+1$ can be written as a function of B,

$$S_{n+1}(B) = S_{\mathrm{F}} = (n+1+\gamma)\frac{2\pi e}{\hbar}B_1, \tag{1.20}$$

where S_{F} is the area of the Fermi surface, and B_1 is some finite magnetic field. We have assumed that the $n+1$-th orbit has only just left the Fermi surface, so the area of the orbit covered by $n+1$-th is equal to the area of the Fermi surface. Assuming that the n-th orbit reaches an area of the orbit S_{F} at some different finite magnetic field $B_2 > B_1$, i.e.,

$$S_n(B) = S_{\mathrm{F}} = (n+\gamma)\frac{2\pi e}{\hbar}B_2. \tag{1.21}$$

Using the above two equations, a relation can be made with the period of the oscillation and S_{F},

$$S_{\mathrm{F}}\left(\frac{1}{B_1} - \frac{1}{B_2}\right) = \frac{2\pi e}{\hbar}. \tag{1.22}$$

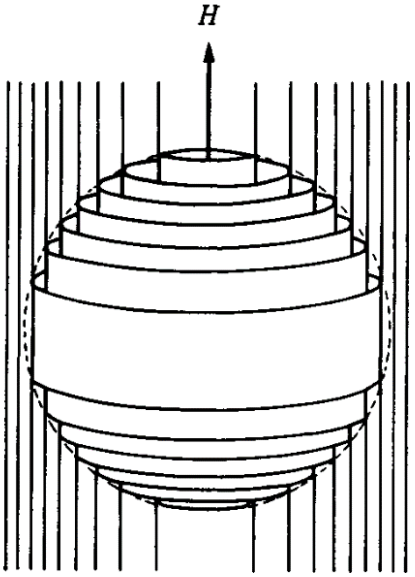

FIGURE 1.22: Schematic image of Landau tubes inside a 3D spherical Fermi surface. This figure is reproduced from Reference. [73] with permission of Cambridge University Press through PLSclear.

It should be noted that S_F is constant. The above equation shows that after the $n+1$-th orbit has just left the Fermi surface, the n-th orbit will leave the Fermi surface such that an increment in $1/B$, i.e., $\Delta 1/B = (1/B_1) - (1/B_2)$ is constant. This is also true for $n-1$, $n-2$ and so on. Thus, SdH oscillations are periodic in $1/B$. This also means that by measuring the frequency of the SdH oscillation with respect to $1/B$, we can estimate the Fermi surface area S_F through the relation

$$f_{1/B} = \left(\frac{1}{B_n} - \frac{1}{B_{n+1}}\right) = \frac{2\pi e}{\hbar S_F}. \tag{1.23}$$

where $f_{1/B}$ is the frequency of the SdH oscillation with respect to $1/B$.

1.4.3 3D systems

Similar arguments can be made in 3D systems. In 3D, the quantized orbit forms cylinders along the applied magnetic field. This can be regarded as the black solid lines in Fig. 1.20(b) extended along the z axis in the k space.

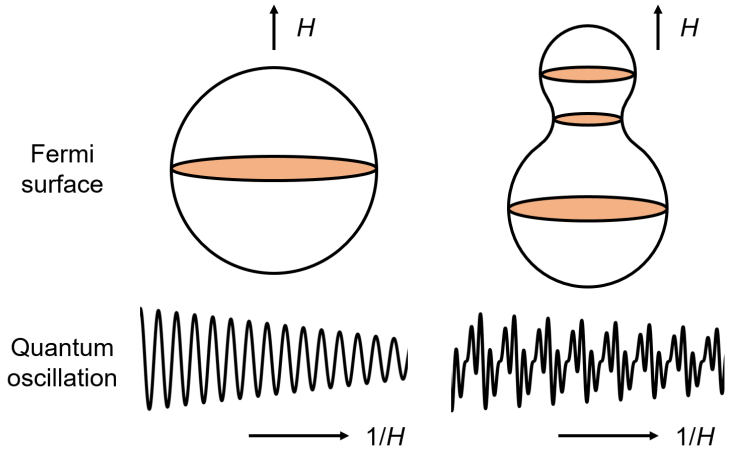

FIGURE 1.23: Schematic image of the Fermi surface and the corresponding quantum oscillations. Multiple extremal cross sections in the Fermi surface (shaded in orange) result in a superposition of different frequencies in the quantum oscillation.

These are known as Landau tubes. Again, the only occupied states are only states within the Fermi surface. In Fig. 1.22, Landau tubes for a spherical Fermi surface are shown. Only states within the spherical Fermi surface are occupied, shown as the solid lines inside the sphere. As the magnetic field is increased, the Landau tubes expand perpendicular to the applied magnetic field. In 3D, the Landau tubes completely pass through the Fermi surface at points known as extremal cross sections. The extremal cross sections are the maxima and minima cross sectional areas of the Fermi surface perpendicular to the applied magnetic field [74]. As shown in the previous subsection, the area of the Fermi surface determines the frequency of the SdH oscillation. If the Fermi surface is a sphere, there is one extremal cross section, so SdH oscillations will be a single frequency. If there are multiple extremal cross sections, this results in the Landau tubes passing through the Fermi surfaces at different $1/B$ frequencies, and hence SdH oscillations with a superposition of multiple frequencies are observed. The schematic image of the Fermi surface structures and its corresponding quantum oscillations are shown as Fig. 1.23.

1.4.4 Amplitude of SdH: Lifshitz-Kosevich formula

From the SdH amplitudes, physical quantities such as relaxation times of the cyclotron motion can be obtained. This is because the amplitude of the SdH oscillations are reduced in real materials by two main factors. One is the effect of finite temperature. At 0 K, the boundary between the occupied and unoccupied states is sharp at the Fermi surface. When the Landau tubes pass through the Fermi energy, a large abrupt change occurs depending on the number of occupied states. This results in a large SdH oscillation amplitude. However, a finite temperature slightly blurs out the boundary between the occupied and unoccupied states by a range of $k_{\mathrm{B}}T$. This leads to a less abrupt decrease in the occupied states and a damping of the SdH amplitude. The other effect is the uncertainty principle, $\Delta E \Delta t \geq \hbar$. The sharpness of the Landau levels, and therefore the Landau tubes, will be blurred by some finite range $\hbar/\Delta t$ where Δt is a finite relaxation time of the electron cyclotron motion. Again, the blurring will lead to a less abrupt change in the occupied states, leading to a damping of the SdH amplitude.

The amplitude of the SdH oscillation is well-described by the Lifshitz-Kosevich (LK) formula,

$$\Delta\rho' \propto \frac{\lambda(B)T}{\sinh\{\lambda(B)T\}} e^{-\lambda(B)T_{\mathrm{D}}} \cos\left\{2\pi\left(\frac{F}{B} - \frac{1}{2} + \beta + \delta\right)\right\}, \tag{1.24}$$

where $\Delta\rho'$ is the oscillatory part of the magnetoresistance. F is the frequency, $2\pi\beta$ is the Berry phase, and δ is a phase shift which is 0 and $\pm\frac{1}{8}$ for 2D and 3D systems, respectively. $\lambda(B)$ is given as

$$\lambda(B) = (2\pi^2 k_B m^*)/(\hbar e B), \tag{1.25}$$

where m^* is the effective cyclotron mass. The factor

$$\lambda(B)T/\sinh\{\lambda(B)T\} \tag{1.26}$$

in the LK formula is also known as the reduction factor R_T. This is the factor which accounts for the damping of the SdH amplitudes due to the finite temperature. The temperature dependence of the FFT amplitudes can be fitted using R_T in order to determine the effective mass of the cyclotron motion.

T_{D} is the Dingle temperature, which has the form $\frac{\hbar}{2\pi k_B}\frac{1}{\tau_q}$. τ_q is known as the quantum lifetime, which is the finite relaxation time for the cyclotron motion due to scattering effects. The Dingle temperature accounts for the forementioned damping effect due to the uncertainty principle. The quantum lifetime can be determined from T_D, and the mobility of the conduction electrons can be calculated from the quantum lifetime.

1.5 Anomalous Hall effect

In this section, we will discuss the concept of the anomalous Hall effect (AHE), which is related to the electrical transport measurements performed in the triangular lattice antiferromagnet Ag_2CrO_2.

AHE is the effect in which the measured resistivity transverse to the applied current is enhanced proportionally to the magnetization of the material. First observed in 1880 [75], it is well known that the following empirical formula often holds for the Hall effect in a magnetic material [76, 77],

$$\rho_{yx} = R_0 H_z + R_s M_z, \tag{1.27}$$

where ρ_{yx} is the transverse resistivity, R_0 is the ordinary Hall coefficient, R_s is the anomalous Hall coefficient and M_z is the magnetization along the direction of the applied field. The first term on the right hand side is the ordinary Hall effect which is inversely proportional to the carrier density, and the second term is the AHE. Although the AHE seems like a simple proportional relationship between the transverse resistivity and the magnetization of the material, its detailed origin are far more complicated than one might expect, and active research is still being performed to elucidate the origin of the anomalous Hall behavior in various magnetic materials. In recent years, it is widely accepted that two main mechanisms play a key role in the emergence of the anomalous Hall effect, which is the intrinsic and extrinsic mechanisms [78]. In the next subsections, we will provide an introductory summary of these two main mechanisms.

1.5.1 Intrinsic mechanism

In this subsection, we will discuss the intrinsic mechanism of AHE. This mechanism was first proposed by Karplus and Luttinger (KL) [79], and originates from the intrinsic band structure of the material, hence its name. In a ferromagnetic material, conduction electrons are coupled to the magnetic order through the spin-orbit interaction (SOI). In the presence of an external applied field, the total Hamiltonian of the material $\mathcal{H}_T$ can be written as

$$\mathcal{H}_T = \mathcal{H}_0 + \mathcal{H}_{\mathrm{SOI}} + \mathcal{H}_E. \tag{1.28}$$

Here, $\mathcal{H}_0 = p^2/2m + V(\boldsymbol{r})$ is the Bloch Hamiltonian of the electron in the absence of SOI, $\mathcal{H}_{\mathrm{SOI}} = [\sigma \times \nabla V(\boldsymbol{r})] \cdot \boldsymbol{p}/4m^2c^2$ is the SOI term, and $\mathcal{H}_E = -e\boldsymbol{E} \cdot \boldsymbol{r}$ is the perturbation due to the applied electric field. p is the momentum, m the mass, and r the position of the electron, respectively. KL calculated the effect of SOI on the transverse conductivity, and showed that when an external electric field is applied to the material, an additional contribution to the group velocity is obtained by the conduction electrons. KL proposed that this "anomalous velocity" of the conduction electrons are the origin of the AHE.

The intrinsic mechanism had been first derived in 1954 by KL, and it has recently attracted renewed interest from the point of view of band topology [80, 81]. Since KL's theory is a direct consequence of interband coherence, which is determined by the intrinsic band structure of a material, connection could be made between the Berry phase curvature of the band and the "anomalous velocity" of the conduction electrons. From a topological perspective, the intrinsic AH conductivity $\sigma_{ij}^{\mathrm{AH-int}}$ can be calculated directly form the Kubo formula for the Hall conductivity, given the eigenstates $|n, \boldsymbol{k}\rangle$

and eigenvalues $\epsilon_n(\boldsymbol{k})$ of the Bloch Hamiltonian $\mathcal{H}_0$,

$$\begin{aligned}\sigma_{ij}^{\mathrm{AH-int}} = e^2\hbar \sum_{n\neq n'} \int \frac{d\boldsymbol{k}}{(2\pi^d)}[f(\epsilon_n(\boldsymbol{k})) - f(\epsilon_{n'}(\boldsymbol{k}))] \\ \times \mathrm{Im}\frac{\langle n,\boldsymbol{k}|v_i(\boldsymbol{k})|n',\boldsymbol{k}\rangle \langle n',\boldsymbol{k}|v_i(\boldsymbol{k})|n,\boldsymbol{k}\rangle}{[\epsilon_n(\boldsymbol{k}) - \epsilon_{n'}(\boldsymbol{k})]^2}\end{aligned} \tag{1.29}$$

where the velocity operator is defined by

$$\boldsymbol{v}(\boldsymbol{k}) = \frac{1}{i\hbar}[\boldsymbol{r}, \mathcal{H}_0(\boldsymbol{k})] = \frac{1}{\hbar}\nabla_k \mathcal{H}_0(\boldsymbol{k}). \tag{1.30}$$

Then, it can be shown that this contribution is directly related to the topological properties of the Bloch states, i.e., the integration over the Fermi sea of the Berry curvature of the occupied bands. By noting that

$$\langle n,\boldsymbol{k}|\nabla_k|n',\boldsymbol{k}\rangle = \frac{\langle n,\boldsymbol{k}|\nabla_k \mathcal{H}_0(\boldsymbol{k})|n',\boldsymbol{k}\rangle}{\epsilon_{n'}(\boldsymbol{k}) - \epsilon_n(\boldsymbol{k})}, \tag{1.31}$$

Eq. (1.29) can be expressed as

$$\sigma_{ij}^{\mathrm{AH-int}} = -\varepsilon_{ijl}\frac{e^2}{\hbar}\sum_n \int \frac{d\boldsymbol{k}}{(2\pi)^d} f(\varepsilon_n(\boldsymbol{k}))b_n^l(\boldsymbol{k}), \tag{1.32}$$

where ε_{ijl} is the antisymmetric tensor and $\boldsymbol{b}_n(\boldsymbol{k})$ is the Berry-phase curvature,

$$\boldsymbol{b}_n(\boldsymbol{k}) = \nabla_k \times \boldsymbol{a}_n(\boldsymbol{k}). \tag{1.33}$$

Here, $\boldsymbol{a}_n(\boldsymbol{k})$ is the Berry-phase connection $\boldsymbol{a}_n(\boldsymbol{k}) = i\langle n,\boldsymbol{k}|\nabla_k|n,\boldsymbol{k}\rangle$, corresponding to the states $\{|n,\boldsymbol{k}\rangle\}$. It is important to stress that this AHE mechanism is determined only by the nature of the band structure, and thus independent of the electron transport lifetime τ or the electrical conductivity of the material.

1.5.2 Extrinsic mechanism

In contrast to the theory proposed by KL, which was completely governed by the intrinsic band structure of the material, other mechanisms of AHE arising from extrinsic effects such as scattering by impurity sites had also been actively researched in the middle of the 20th Century. This is known as the extrinsic mechanism. Here, we review some of the extrinsic mechanisms of AHE which are related to this thesis.

Skew scattering mechanism

The most well known extrinsic mechanism of AHE is the skew scattering mechanism, first proposed by Smit [82, 83]. In the linear response regime, the acceleration of electrons due to the electric field $\boldsymbol{E}$ should be balanced out by the scattering from impurities and phonons for the steady-state current. Smit pointed out that this balance was absent from the KL theory, and argued that the "anomalous velocity" proposed by KL would disappear when taking this balance in consideration. This is because the anomalous velocity component is proportional to the acceleration $\dot{k}$. $\dot{k}$ should disappear in the steady-state where the force from $\boldsymbol{E}$ is balanced with the scattering from the impurity potentials. Instead, Smit proposed that asymmetric scatterings due to impurity sites were the origin of AHE. In the presence of SOI, the matrix element of the impurity scattering potential can be expressed as

$$\langle \boldsymbol{k}', s'|V|\boldsymbol{k}, s\rangle = \tilde{V}_{\boldsymbol{k},\boldsymbol{k}'}\left(\delta_{s,s'} + \frac{i\hbar^2}{4m^2c^2}(\langle s'|\boldsymbol{\sigma}|s\rangle \times \boldsymbol{k}')\cdot\boldsymbol{k}\right). \tag{1.34}$$

In a microscopic equilibrium condition, the transition probability $W_{m\to n}$ between states n and m should be identical to the transition probability of the opposite direction, $W_{n\to m}$. For example, this is true in the Fermi's golden-rule

approximation,

$$W_{n\to m} = \frac{2\pi}{\hbar} |\langle n|V|m\rangle|^2 \delta(E_n - E_m), \tag{1.35}$$

where V is the perturbation which induces the transition. Meanwhile, this microscopic equilibrium is not strictly universal. For example, the equilibrium is broken for calculations of the Hall conductivity, which involves the second Born approximation. For a simple model in which the conduction electrons are scattered once per an impurity site, the asymmetric part of the transition probability can be included as

$$W^A_{\boldsymbol{k}\boldsymbol{k}'} = -\tau_A^{-1} \boldsymbol{k} \times \boldsymbol{k}' \cdot \boldsymbol{M}_s, \tag{1.36}$$

where τ_A^{-1} is the scattering rate for the asymmetric part. With the inclusion of this asymmetric scattering (also known as the "skew scattering"), the scattering probability $W_{\boldsymbol{k}\to\boldsymbol{k}'}$ takes a different value from $W_{\boldsymbol{k}'\to\boldsymbol{k}}$. From a physical perspective, this means that the scattering of the conduction electron induces a momentum perpendicular to both the incident moment $\boldsymbol{k}$ and the magnetization $\boldsymbol{M}$, leading to a transverse current proportional to the longitudinal current. This also implies that this AH conductivity is proportional to the longitudinal conductivity σ_{xx}, therefore also proportional to the conduction electron transport lifetime τ. Although this mechanism is distinct from the theory proposed by KL, it is also consistent with various experiments, especially for dilute magnetic alloy systems [84].

Kondo theory of skew scattering

After the findings by Smit, Kondo proposed a finite-temperature model in which spin excitation of localized moments leads to skew scattering [85]. In the KL theory, the model considers itinerant magnetism where the conduction electrons are also responsible for the magnetization of the material.

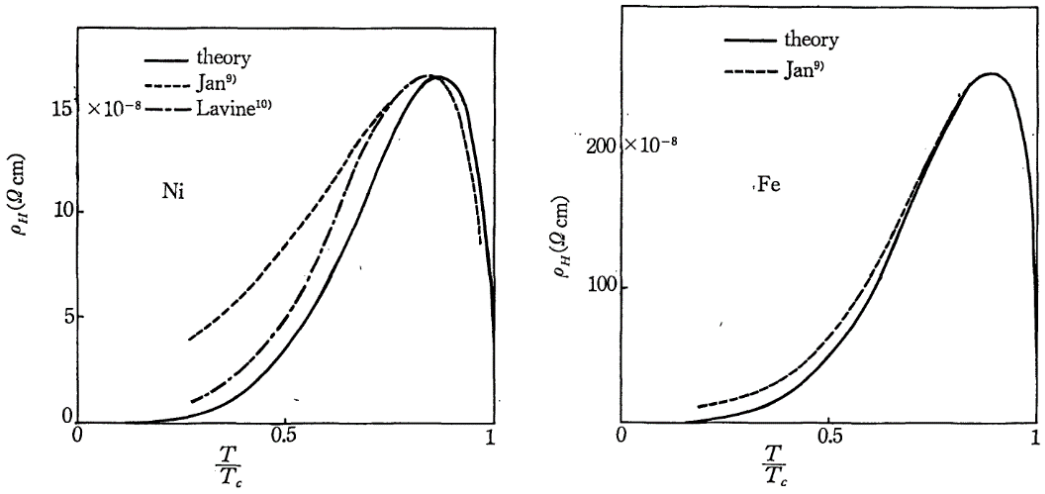

FIGURE 1.24: The experimental data of the anomalous Hall resistivity for Fe and Ni with the theory by Kondo. This figure is reproduced from Reference. [85] by permission of Oxford University Press.

Kondo focused on the opposite model in which the non-magnetic conduction electrons are scattered by the spin excitation of the localized magnetic moments, which is a valid model in the cases where the orbital moments of the localized electrons are not quenched. In such a case, Kondo showed that the second-order perturbation of the usual *s-d* Hamiltonian due to the inclusion of the spin-orbit coupling introduces an AHE current, which originates from a finite asymmetric transition probability (skew-scattering) $\sim \boldsymbol{k} \times \boldsymbol{k}'$. From these calculations, Kondo showed that the AHE is enhanced due to third-order fluctuations of the magnetic moments $\chi_1 \sim \sum \langle (M - \langle M \rangle)^3 \rangle$, and the theoretical temperature dependence of the AH resisitivity was found to match well with the experimental observations in ferromagnets such as Ni and Fe as shown in Fig. 1.24 [86, 87]. This result is one of the earliest works which showcased the significant influence of the magnetic moment fluctuations on the AHE.

1.5.3 Scaling relation

As discussed in the previous subsections, the mechanism of AHE can be parsed into the intrinsic mechanism and the extrinsic mechanism. The former originates from the intrinsic band structure of each material, and thus is independent of the transport lifetime τ, while the latter is due to asymmetric scattering by impurity sites, where its effect is proportional to the transport lifetime. Therefore, progress has been made to formulate a universal scaling relationship between the AH conductivity σ_{xy} and the longitudinal conductivity σ_{xx}. So far, it has been shown that there are roughly three major regimes for the behavior of AHE based on experimental reports of various materials as well as theoretical studies [78, 88]. This is shown in Fig. 1.25. In the high longitudinal conductivity region ($\sigma_{xx} > 10^6$ $(\Omega\text{cm})^{-1}$), the skew scattering is dominant, resulting in a scaling relation of $\sigma_{xy} \propto \sigma_{xx}$, known as the "superclean limit". In the intermediate metallic region ($10^4 < \sigma_{xx} < 10^6$ $(\Omega\text{cm})^{-1}$), known as the "moderately dirty metals", the intrinsic mechanism is known to dominate. This results in a constant σ_{xy}, independent of σ_{xx}. Finally, in the bad metal region ($\sigma_{xx} < 10^4$ $(\Omega\text{cm})^{-1}$), known as the "incoherent regime", the AH conductivity is known to follow a characteristic scaling of $\sigma_{xy} \propto \sigma_{xx}^{1.6}$, although the physical origin of this scaling law is still under investigation. Nevertheless, these scaling relations have been an important stepping stone in the unified understanding in the AHE of various materials, and also a useful tool in characterization of the origin of AHE for newly found magnetic materials.

Meanwhile, materials with unconventional AHE that do not follow these scaling relations have also been gaining large attraction. For example, some kagome lattice materials with non-coplanar magnetic structure has been found to possess AHE which does not follow the above scaling law, with the AH conductivity much higher than the typical ferromagnets such as Fe [15, 16].

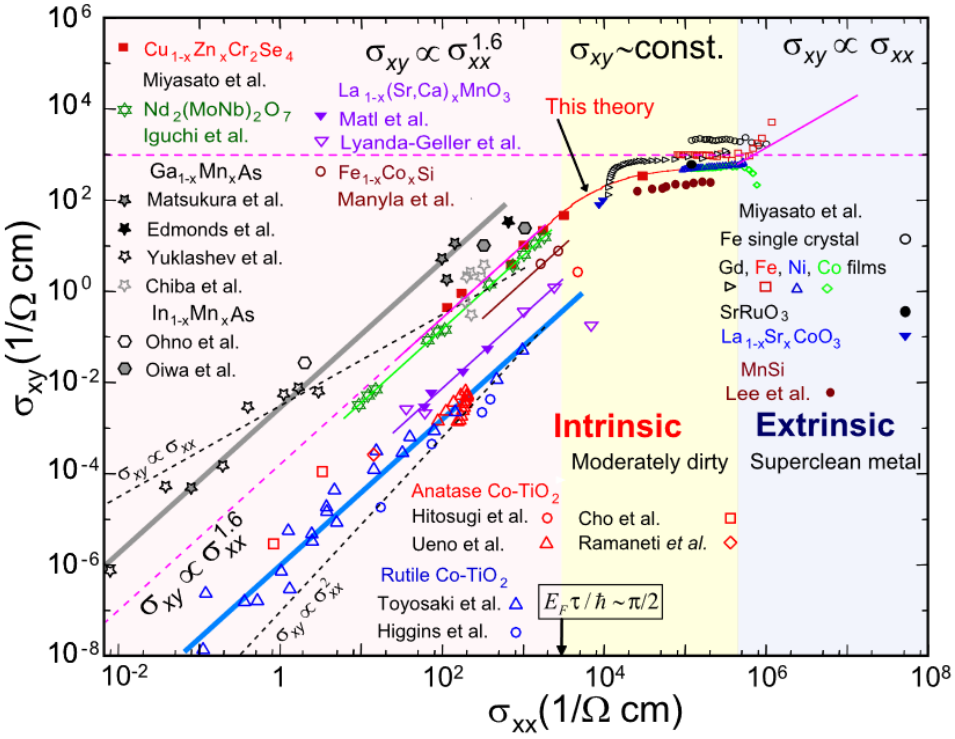

FIGURE 1.25: The scaling relation of the AHE with various experimental data. This figure is reproduced with permission from Reference. [88] Copyright 2023 by the American Physics Society.

These materials further deepens the understanding of the detailed physics behind the AHE, and also pave way for magnetic materials which surpass the limit of the AH conductivity set by the conventional mechanisms, which is expected to be useful towards next generation magnetic devices.

1.6 Purpose of this thesis

As mentioned, the field of atomically layered magnetic materials is an active and emerging field. The purpose of this thesis is to investigate the electrical transport properties of the atomically layered antiferromagnet thin-film devices, with prospects of probing the electrical and magnetic properties unique to the thin-films. In particular, we focus on two antiferromagnets.

The first is the rare-earth antiferromagnet $CeTe_3$, which has gained attraction recently as an atomically layered antiferromagnet with high mobility. While the material possesses unique characteristics such as the coexistence of CDW and magnetic order, there are no prior reports of the thin film measurements. If the high mobility is retained in the thin-film devices, unique electrical transport phenomena owing to the mobility such as the quantum oscillations can be expected. Furthermore, a strong coupling between the conduction electrons and the magnetic state is indicated in this material, since this is the only material in the family of rare-earth tritellurides where the RKKY interaction is the dominant magnetic interaction. Therefore, a significant modulation of the electrical properties can be expected with the onset of the magnetic order.

The second is the triangular lattice antiferromagnet Ag_2CrO_2, which has a unique magnetic structure of a 5 sublattice partially disordered state, owing to the large frustration in the material. It is one of the few triangular lattice antiferromagnets to possess a highly metallic conduction, and unique electrical transport properties had been measured in the vicinity of its magnetic transition temperature even in the bulk sample. While the electrical transport measurements of Ag_2CrO_2 had been limited by the fact that the bulk sample is inherently polycrystalline, it was recently shown that thin films of nearly monocrystalline samples can be obtained through the scotch tape method. Therefore, further unique phenomena owing to the exotic magnetic structure

can be expected in the electrical transport measurements of the Ag_2CrO_2 thin films.

Specifically, we have fabricated electrodes on the antiferromagnetc thin films, and performed longitudinal magnetoresistance and Hall measurements down to low temperatures. In the next Chapters, we will outline the experimental details and results of the electrical transport measurements performed for the $CeTe_3$ and Ag_2CrO_2 thin film devices.

Chapter 2

Experimental methods

In this research, we have fabricated nanometer-scale (nanoscale) devices, in order to perform electrical transport measurements of two kinds of atomically layered antiferromagnetic thin films, i.e., $CeTe_3$ and Ag_2CrO_2. In the following section, we first outline the device fabrication process and the explanation of the equipment, followed by the measurement setup.

2.1 Device fabrication techniques

2.1.1 fabrication of atomically layered thin films

Atomically layered thin films are fabricated from layered materials using a method known as the "Scotch tape" method. In this method, a bulk layered material is placed onto a scotch tape and peeled a number of times. The peeling leads to fabrication of thin film flakes, even down to a single atomic layer. This can be transferred onto a suitable substrate, where contact electrodes can be attached to the thin films for electrical transport measurements. The schematic image of the mechanical exfoliation technique and the optical microscope photos of the exfoliated thin films are shown in Figs. 2.1(a) and 2.1(b), respectively. The Scotch tape method allows an easy fabrication of thin film devices down to few nanometers in thickness, but the typical size of these thin flakes also decreases with decreasing the thickness. Since the size

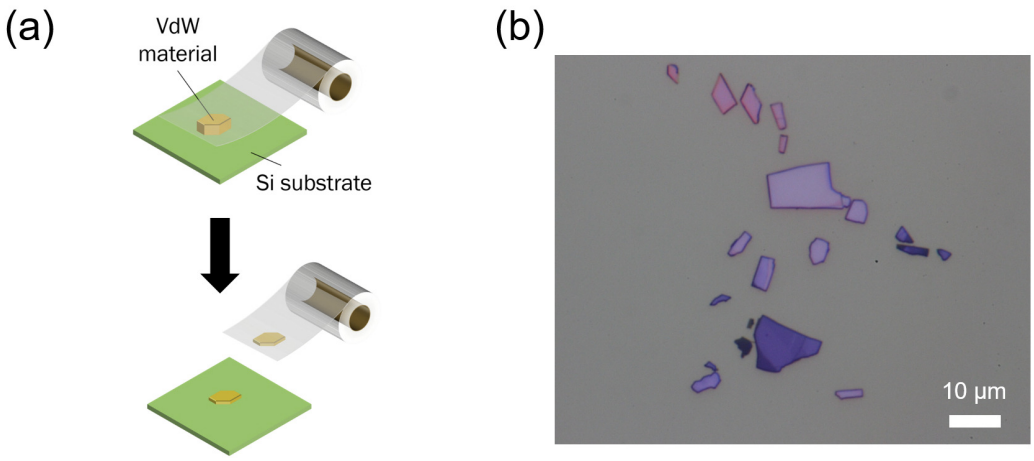

FIGURE 2.1: (a) Schematic image of the mechanical exfoliation method. (b) Optical microscope image of the exfoliated thin films.

of the flakes is of the order of few micrometers to a few hundred nanometers, nanofabrication is required to fabricate contact electrodes on the thin films.

2.1.2 Fabricaion of nanoscale devices

The following outlines a typical series of procedures for nanoscale fabrication. First, the nanoscale devices require a foundation where it can be fabricated. This is usually an insulating substrate: in this research, a $5\times5\text{mm}^2$ SiO_2/Si substrate is chosen.

The flow of the nanoscale pattern creation is shown in Fig. 2.2. First, the surface of a $5\times5\text{mm}^2$ SiO_2/Si substrate was coated with polymethylmethacrylate (PMMA) using a spin coater. The substrate was subsequently heated using a hot plate which hardens the PMMA. The PMMA is a type of resist (similar to a photoresist), meaning that it can be removed from the substrate when it is exposed to an electron beam followed by submersion in developer fluid. Nanoscale patterns were exposed onto the PMMA using an electron beam, and the substrate was submerged in a developer fluid (solution of isopropyl alcohol (IPA) and 4-methyl-2-pentanone mixed at a ratio of

3:1).

At this point, the substrate was still largely coated with the PMMA resist, except for the nanoscale patterns which were exposed and developed. Then, a desired material (Ti, Au) was deposited onto the substrate. Finally, the substrate was dipped in acetone which dissolves the resist. When the PMMA resist is dissolved, this also removes the deposited material above the resist from the substrate. The material which were deposited directly onto the substrate remains, meaning that the deposited material remains onto the substrate in the shape of the nanoscale pattern. While submerged, a flow of acetone was applied on the substrate by repeatedly sucking and draining a small pipette just above the substrate. This was done in order to make sure all of the materials except for the nanocale patterns were removed. Additionally, ultrasonic cleaning was performed to further remove the unwanted materials. This final process is known as the liftoff process. This entire procedure can be performed multiple times on a single substrate, allowing a flexible design of the nanoscale measurement devices.

Next, we outline some of the characteristic techniques and machines used in the fabrication process.

2.1.3 Electron beam lithography system: ELS 7000

The electron beam lithography system (ELS 7000) allows precise exposure of the substrate using an electron beam, with a theoretical minimum spacial resolution of 10 nm. Nanoscale patterns were designed using a commercial software such as AutoCAD and transferred to the system using a USB. The amount of total exposure of the substrate can be controlled through its electron beam current (how much electrons reach the substrate per second) and dose time (how long the substrate is exposed to the electron beam). This can be adjusted manually. It is important to use just the right amount of

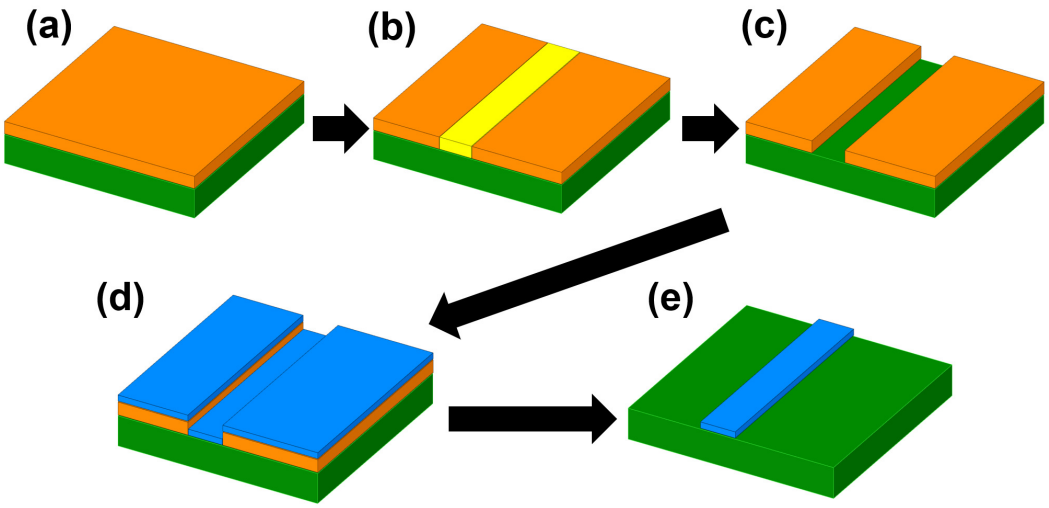

FIGURE 2.2: Flow of the fabrication of nanoscale patterns. (a) The substrate (shown in green) is coated by PMMA (shown in orange). (b) The PMMA is partially exposed to an electron beam (shown in yellow). (c) The PMMA is developed, which removes the exposed PMMA. (d) A desired material (e.g. Au, Ti, Cu, etc.) are deposited on the entire surface (shown in blue). (e) Finally, the rest of the PMMA is removed by submersion in acetone and liftoff.

exposure, as overexposure leads to a bloated and enlarged pattern, while underexposure results in unsuccessful removal of the exposed PMMA in the development process.

2.1.4 Electron beam and resistive heating depositions

Vapor deposition is one of the methods in which a material is deposited onto the substrate. For electron beam deposition, the depositing material (also called the target) is placed in a hearth, and the substrate is placed straight above the hearth. An electron beam is shot towards the target. This heats the target, and the material vaporizes. Under high vacuum, the mean free path of the metal vapor is of the order of meters, and thus moves straight upwards with little scattering. This is then deposited onto the substrate, creating a thin film of the target material on the substrate. The schematic image of electron beam deposition is shown in Fig. 2.3(a). The main advantage of this method is that since the energy of the electron beam is very high, it allows deposition of metals with high melting points.

In order to perform the electron beam deposition, the developed substrate was first placed on a deposition stage and placed in the Load-Lock (LL) chamber. The LL chamber was vacuumed until it was below 3×10^{-4} Pa, after which the stage was transferred to the main chamber. Deposition took place after cooling the main chamber with liquid N_2 in order to temporarily improve the vacuum. The electron beam current was controlled to achieve an optimal deposition rate and thickness, which will be detailed in the later sections.

For resistive heating deposition, the general principle is the same as electron beam deposition. The difference is that the depositing material is placed onto a tungsten boat. A large current is applied to the tungsten boat, and the boat heats up due to Joule heating. This then melts the material and the

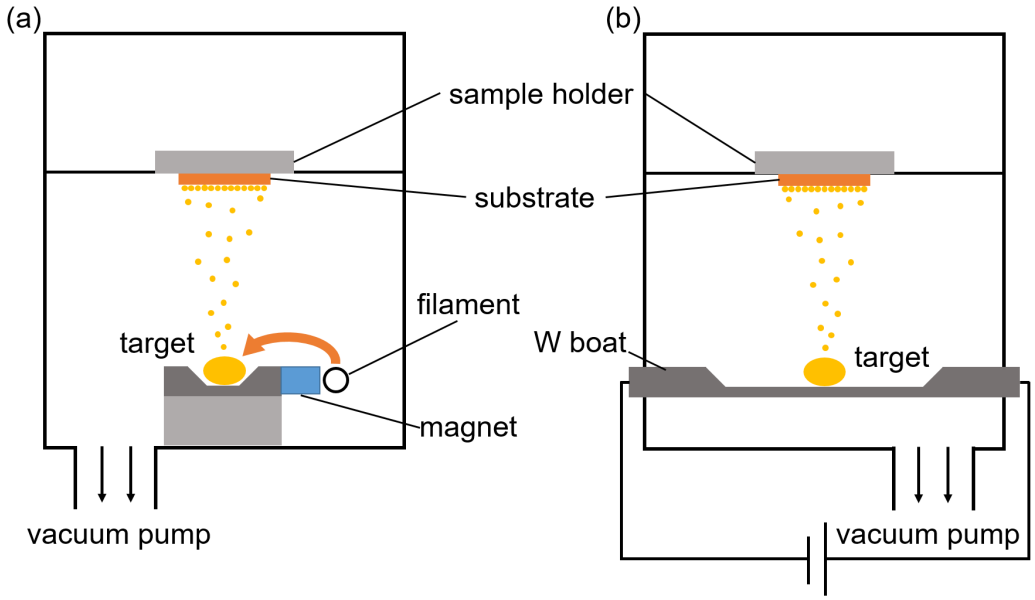

FIGURE 2.3: (a) Schematic image of the electron beam deposition. The electron beam is emitted from the filament, which bent by a magnet and irradiated onto the target. (b) Schematic image of the resistance heating deposition. A large current is applied through a tungsten boat, which evaporates the target through Joule heating.

vapor is deposited on the substrate. The schematic image of this process is shown in Fig. 2.3(b). The procedure of resistive heating deposition is very similar to that of electron beam deposition, with the difference of controlling the current through the tungsten boat instead of the electron beam current.

In this research, electron beam deposition was used to deposit Ti, while resistive heating deposition was used to deposit Au which has a low melting temperature.

2.1.5 Ar milling

Ar milling is a method of removing a small amount of the substrate and device surface. An Ar ion beam is accelerated towards the substrate which "mills" the surface. Since Ar is an inert gas, it is useful for removing oxidized layers of metals and improves an Ohmic contact. Moreover, since the milling machine is connected to the LL chamber, it allows deposition to take

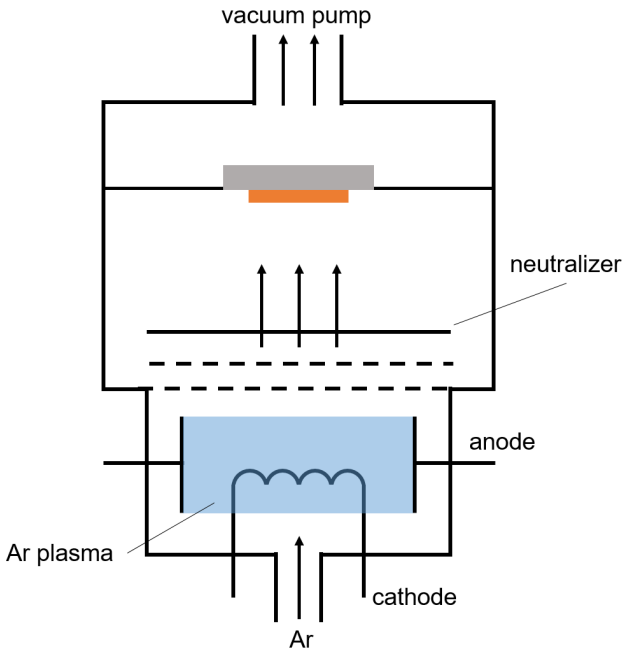

FIGURE 2.4: Schematic image of the Ar milling system. The cathode and anode generate an Ar plasma, which is accelerated towards the substrate to "mill" its surface.

place directly after Ar milling without exposure of the substrate to ambient air. Therefore, Ar milling is usually performed just before the electron beam/resistive heating deposition process. The schematic of the Ar milling system is shown in Fig. 2.4.

To perform Ar milling, the substrate was first attached to a stage and placed in the LL chamber. The chamber was vacuumed to roughly 3×10^{-4} Pa. Then, the milling source was turned on and Ar was leaked into the chamber at a rate of 10 sccm. This was maintained for 5 minutes with the shutter closed, and 5 minutes with the shutter open. This was done in order to fill the chamber with Ar and wash away any impurity gases. Then, the Accelerator was set to 400 V and 12 mA, and the Beam was set to 600 V. The Ar flow was set to 0.5 sccm, and the source was turned on. This was maintained for 15 sec to stabilize the Ar source, then the Ar beam was switched on to perform the Ar milling.

2.1.6 O_2 etching

O_2 etching is another method used to "mill" the surface of the substrate. This process removes a small amount of the substrate surface, and ensures that any residual PMMA or any other unwanted material was removed.

O_2 etching was usually performed when starting from a new substrate, to make sure that the PMMA can be spin coated properly. In O_2 etching, the substrate is placed in a vacuum chamber. The chamber is partially filled with O_2 after vacuumed. The roof and floor of the chamber are electrodes which a large voltage is applied. The O_2 becomes a plasma state under the large electric field, and O_2^+ ions collide with the substrate. This removes some of the substrate surface, ensuring a clean surface.

To perform the O_2 etching, the substrate was placed inside the chamber. Since the floor of the chamber is a large electrode, the substrate was placed on top of a glass plate in order to avoid conduction between the electrode and the substrate. When the etching machine is turned on, it automatically vacuums the chamber. The chamber was vacuumed to roughly 2.5 Pa. To begin the etching process, O_2 was leaked in the chamber to roughly 8 Pa and the voltage was turned on.

2.1.7 Glove box

Some materials may be sensitive to humidity of the surroundings, or oxidize extremely fast. Therefore, a fabrication space where no moisture or oxygen exists is highly preferable. Glove box is a box filled with high purity Ar. Since Ar is inert, devices stored within the glove box has the least probability of oxidization. The moisture of the Glove box is also highly regulated, so there is also the least probability of humidity interacting with the devices. The exterior of the glove box is shown in Fig. 2.5.

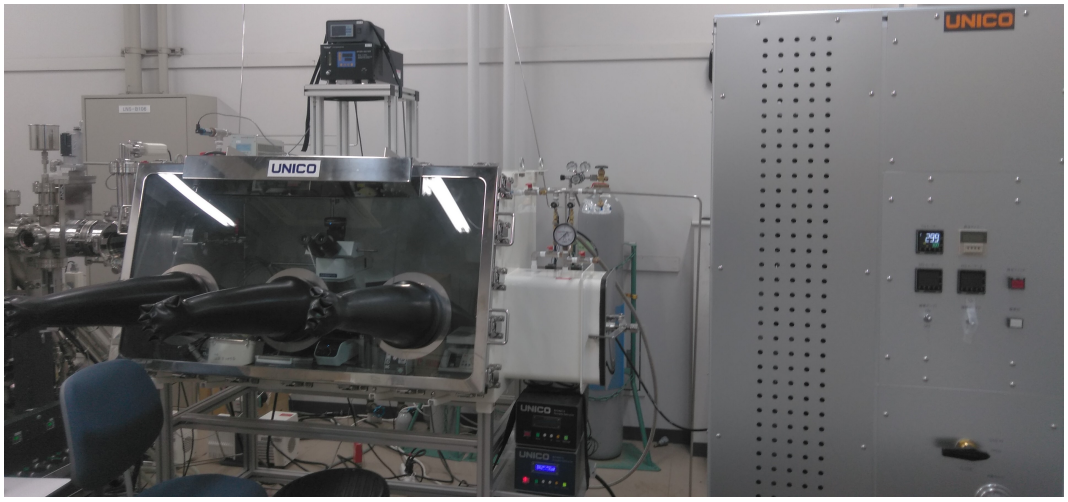

FIGURE 2.5: The exterior of the Ar filled glove box.

2.1.8 Chip carrier and wire bonding

Chip carriers are small chips which can be set on the measurement insert. They have gold electrode pads which, when set on the insert, connects electrically to an external switch box. The electrode pads of the nanoscale devices are connected to the electrode pads of the chip carrier, so that the measurement set up can be controlled externally by connecting the switch box with the external circuitry. In order to connect the electrode pads, a wire bonder is used. This is a machine which connects two points using an Al($Al_{99}Si_1$) wire. Once the nanoscale device fabrication is complete, the substrate is set on the chip carrier and wire bonded. This allows various measurements to be performed.

Next, we outline the specific fabrication process and conditions for the measurement devices prepared in this research.

2.2 Device fabrication conditions

Here, we outline the experimental conditions for fabrication of electrical transport devices of $CeTe_3$ and Ag_2CrO_2.

2.2.1 Device fabrication condition for $CeTe_3$

Single crystals of bulk $CeTe_3$ were provided from Quantum Materials Science Unit of Okinawa Institute of Science and Technology. The bulk sample was synthesized in an evacuated quartz tube. The tube was heated up to 900°C and slowly cooled to 550°C over a period of 7 days.

$CeTe_3$ flakes are transferred onto the SiO_2/Si substrate, and gold electrodes were deposited onto the flakes. No Ti was used, as a drastic increase in the contact resistance was observed. It is also important to note that the Ar milling conditions were crutial in obtaining Ohmic contact. The fabrication conditions of the device are given below. Creating the device in a short span of 2-3 days seemed to result in better devices.

1. A new 5×5 mm^2 SiO_2/Si substrate was brought out of the desiccator. The substrate was submerged in acetone and cleaned using the ultrasonic cleaner at 40 kHz for 5 minutes. Then, the substrate was submerged in IPA and dried using a N_2 gas blower. The substrate was then placed on a glass plate inside the O_2 etching machine. The machine voltage was set to low. O_2 is leaked up to roughly 8 Pa and the etching was performed for 30 seconds.

2. Next, PMMA was coated onto the substrate using the spin coater. The program was set to run at "slope 5 sec, 3000 rpm for 60 sec, then end". A single drop of PMMA was dropped onto the substrate using a large pipette and the spin coater was started. After the spin coating finished, the substrate was placed on a hot plate set to 120°C for 10 minutes.

3. Mark patterns were exposed onto the substrate using electron beam lithography. The large electrode pads were lithographed later, as the positions of the $CeTe_3$ flakes are randomly scattered on the substrate.

The lithography was performed using "coarse" setting, with dose time 0.3 μs at 4 nA.

4. The substrate was then submerged in the developer fluid for 30 seconds, and then submerged in IPA. The substrate was dried using the N_2 blower. This process was performed in ambient air.

5. The substrate was set onto the deposition stage and placed inside the LL chamber. The LL chamber was vacuumed until 3×10^{-4} Pa, and the substrate was transferred to the main chamber. The main chamber was cooled with liquid N_2, and the stage was also cooled for 10 seconds. Ti was deposited by 5 nm using electron beam deposition, at a rate of 0.2 Å/s. Then, Au was deposited by 95 nm using resistive heating deposition, at a rate of 1.0 Å/s.

6. After the depositions, the sample was taken out into ambient air and submerged in Acetone. This was maintained for at least one day, after which the substrate was lifted off by blowing with a pipette, or by applying 40 kHz ultrasonic cleaning for 30 seconds.

7. The substrate was transferred to the Glove box, where the bulk $CeTe_3$ samples were stored. The bulk material was pressed against a scotch tape, which would peel some thin flakes onto the tape. The tape was then pressed against another clean scotch tape (3M Scotch mending tape), and this was repeated several times in order to create thinner flakes. Once enough flakes were observed to be present on the tape, the scotch tape was pressed onto a blue tape (Nitto Denko Dunplon tape) with less adhesive, and the substrate was pressed against the blue tape to transfer the thin flake. The blue tape was used to transfer the thin flakes onto the substrate so that less of the adhesive material of the tape

is transferred onto the substrate and ensured the PMMA to be properly spin coated. The substrate was submerged in Acetone and placed on a hot plate at 60°C for 10 minutes to further remove the adhesive material. Then, the substrate was submerged in IPA and dried using a blower. A bilayer PMMA was coated on the substrate inside the Glove box.

8. The substrate was taken out in ambient air to locate the thin flakes. At this point, the thin flakes makes no contact with ambient air, as the flakes are capped by the bilayer PMMA. The locations of the thin flakes relative to the marks were recorded and photographs were taken. This was aligned with the mark design in AutoCAD and electrode patterns were created. Then, the patterns were lithographed using the electron beam lithography. The patterns which makes contact with the flakes were lithographed in "fine" setting with dose time of 5 μs at 0.2 nA, whereas the rest of the patterns were lithographed using "coarse" setting with dose time 0.3 μs at 4.0 nA.

9. The substrate was developed inside the Glove box, set on the deposition stage and placed in the LL chamber. Ar milling was performed with the same voltage parameter as the above and with a beam time of 55 seconds. Then, the substrate was transferred to the main chamber. The stage was cooled with liquid N_2 for 10 seconds. Au was deposited by 100 nm with resistive heating deposition at a rate of 1.5 Å/s. Slightly higher deposition rates are encouraged, as a rule of thumb the Au tends to "stick" onto the substrate better.

10. After deposition, the substrate is brought back into the Glove box and submerged in Acetone. This is maintained for at least one day. The substrate is lifted off and dried in the Glove box with a blower. Finally, in order to avoid further oxidization in ambient air after taking out the

device from the Glove box, the device was capped with PMMA. A corner of a KimWipe is dipped in a small amount of PMMA and traced on the thin flakes to drop small amounts of PMMA droplets onto the thin flakes. The device is then left on the hot plate at 120 °C for 10 minutes.

2.2.2 Device fabrication condition for Ag_2CrO_2

The polycrystalline bulk Ag_2CrO_2 samples were provided from Electronic Properties of Solids Laboratory of Hokkaido University. The bulk Ag_2CrO_2 crystal was fabricated through solid-state reaction of Ag, Ag_2O and Cr_2O_3 powders, which were encapsulated in gold cells and heated at 1200 °C for 1 h under 6 GPa. The procedures for fabrication of Ag_2CrO_2 thin film devices are almost identical to that of $CeTe_3$ devices, but some procedures are changed because Ag_2CrO_2 is stable under ambient air. We outline the difference in the fabrication procedure from the $CeTe_3$ device below.

1. All procedures which were performed in the Glove box for $CeTe_3$ were performed in ambient air. This is because Ag_2CrO_2 is an oxide and is stable under ambient air conditions.

2. In the deposition process of the electrode (Process 9. for $CeTe_3$), Ti was deposited just before the deposition of Au. This was done in order to increase the adhesion of the Au electrode on the Ag_2CrO_2 thin film, and also because Ag_2CrO_2 was not reactive to Ti. The conditions for the depositions of Ti were 5 nm using electron beam deposition, at a rate of 0.2 Å/s.

2.3 Measurement setup

We outline the measurement setup for our electrical transport measurements. In Figs. 2.6(a) and 2.6(b), we show the typical device structure taken with an

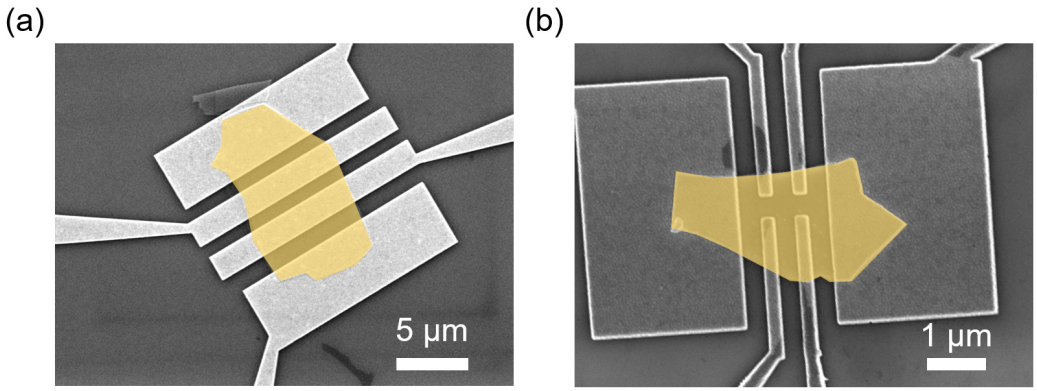

FIGURE 2.6: Scanning electron microscope images for (a) $CeTe_3$ and (b) Ag_2CrO_2 thin film devices. The highlighted (false-color) region indicates the thin films.

electron scanning microscope for $CeTe_3$ and Ag_2CrO_2 respectively. In $CeTe_3$, 4 electrode devices were fabricated in order to maximize the contact area. This was required to ensure an Ohmic contact, since $CeTe_3$ is highly reactive and easily became insulating. In the case of Ag_2CrO_2, it was possible to fabricate 6 - 8 electrode devices due to the ease of obtaining Ohmic contact. This allowed for simultaneous measurements of the magnetoresistance and Hall effect.

For the electrical transport of the thin film devices, We performed a typical 4-terminal resistance measurement using a commercial Lock-in amplifier (SR830 DSP Lock-in Amplifier). A circuit diagram of the electrical measurement is shown in Fig. 2.7. An alternate current was applied to the sample through the internal oscillator of the Lock-in amplifier, and the amplitude of the current was tuned with a resistor (I^+ and I^-). The measured voltage (V^+ and V^-) was amplified through a commercial low-noise amplifier (NF Low Noise Preamplifier LI-75A) and fed back into the Lock-in amplifier for the voltage measurement.

In order to measure the magnetoresistance and Hall effect, a superconducting magnet was used to apply the external magnetic field. To cool the devices, several different refrigerators were used. For $CeTe_3$, a cryogen free

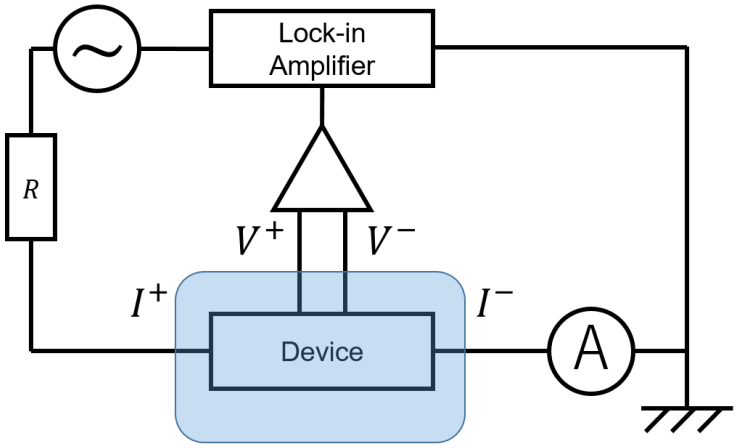

FIGURE 2.7: Circuit diagram for a typical electrical transport measurement. The blue shaded region indicates the area inside the refrigerator.

^{4}He refrigerator (C-Mag Cryogen-Free Superconducting magnet system) was used for the temperature range from 20 to 2 K. Additionally, a ^{3}He-^{4}He dilution refrigerator was used to cool the device in the temperature range from 4 K to 0.4 K. For Ag_2CrO_2, a variable temperature insert using liquid ^{4}He was used for the temperature range from 100 to 5 K.

Chapter 3

Magnetic hysteresis and quantum oscillations in $CeTe_3$ devices

In this chapter, we focus on the electrical transport properties of $CeTe_3$ thin films. This material is in the family of rare-earth tri-tellurides, which had originally been studied from the viewpoint of unique charge density wave (CDW) formation and its complex Fermi surface. Recently, this material family has also been gaining attraction as a high mobility antiferromagnet (AFM), but reports of thin film electrical transport measurements are still limited. In the present chapter, we show the magnetotransport measurements of $CeTe_3$ thin films up to applied fields of 8 T in the temperature range from 20 to 0.4 K. Two characteristic behaviors were observed in the magnetoresistance (MR) of the material, which were previously unreported in the bulk counter part. One is the magnetic hysteresis observed in the MR below its magnetic transition temperature, which suggests the existence of magnetic anisotropy along the stacking direction of the material. The other is the clear quantum oscillation observed below 20 K. The analysis of the quantum oscillations strongly indicates a modulation of the Fermi surface below the magnetic transition temperature for $CeTe_3$, while the mobility was observed to be one of the highest amongst the atomically layered magnetic thin films. In

This Chapter is reproduced from Reference. [24] and Reference. [89] with the permission of AIP Publishing.

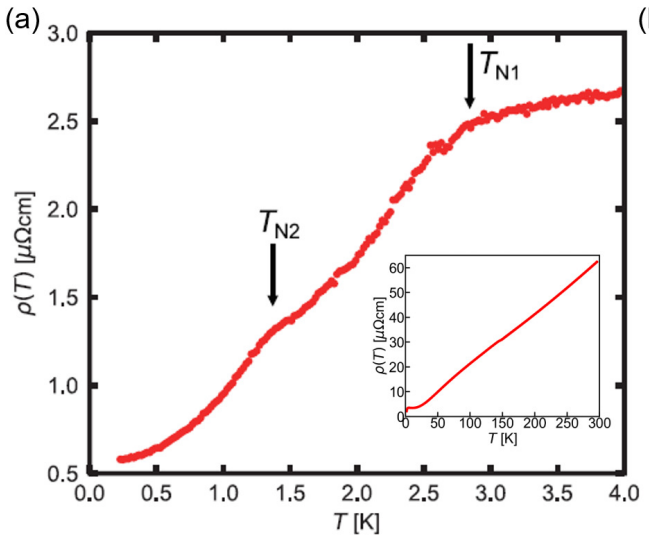

	Thickness	$RRR_{3.5\,K}$
S1	55 nm	18.2
S2	40 nm	32.5
S3	100 nm	18.2

FIGURE 3.1: (a) The temperature dependence of resistivity (device S1) below 4 K. The inset shows the full temperature range from 300 K for a typical device (device S3). (b) The thickness and residual resistivity ratio (RRR) at 3.5 K of the thin film devices discussed in the present measurements.

the next sections, the resistivity measurements are first discussed in order to evaluate the quality of the thin film devices, followed by the discussion of the magnetotransport measurements.

3.1 Evaluation of device quality through resistivity measurements

Devices were fabricated using the methods outlined in Ch. 2. First, we discuss the electrical resistivity of the device at zero applied field in order to evaluate the quality of the measured devices. The resistivity $\rho(T)$ measured with the $CeTe_3$ thin film device is plotted as a function of temperature in Fig. 3.1(a). In bulk, it has been reported that the two Te sheets provides a highly metallic temperature dependence of resistivity in $CeTe_3$, even though the CeTe slab does not possess high electrical conductivity. Such a metallic behavior were also observed in the thin film devices, indicating that the high

quality of the bulk sample is retained in the thin film counterpart. There were two characteristic resistivity changes in the low temperature regime: a significant resistivity drop at $T = 2.7$ K, and a kink structure at $T = 1.3$ K. These behaviors are consistent with the anomalies observed in bulk $CeTe_3$ resistivity measurements, which correspond to the two magnetic phase transitions at $T_{N1} = 3.1$ K and $T_{N2} = 1.3$ K. The anomalies of the resistivity due to the magnetic transition indicate that the conduction electrons are strongly coupled to the magnetic order, which implies that the RKKY should be the main interaction responsible for the magnetic structure in $CeTe_3$. The resistivity at room temperature of this device is 81.3 $\mu\Omega$·cm, resulting in the residual resistivity ratio (RRR) of 59.2 with respect to $\rho(T = 1.5\ \mathrm{K})$. This is 1.3 times higher than the previously reported value of the single crystalline bulk RRR $\sim$ 44.9. At the lowest temperature ($T = 0.2$ K), RRR reaches a value of 140, and a longitudinal resistivity of roughly 0.5 $\mu\Omega$·cm. The relatively high RRR is reproducible in multiple samples, as shown in Fig. 3.1(b). Atomically layered magnetic materials which possess such a high electrical conductivity down to its thin film devices are uncommon; the result showcases the unique high mobility nature of RTe_3 even down to thin film devices.

3.2 Magnetoresistance measurements

Next, we discuss the magnetoresistance (MR) measurements performed for the $CeTe_3$ thin films. For all samples, a positive MR was observed likely owing to the Lorentz force contribution, consistent with previous reports of bulk counterpart. Additionally, two phenomena were observed which were previously unreported for the bulk $CeTe_3$. One of them is the hysteresis in the MR depending on the external field sweep direction, and the other is the clear quantum oscillation in the MR observed at fields higher than 4 T.

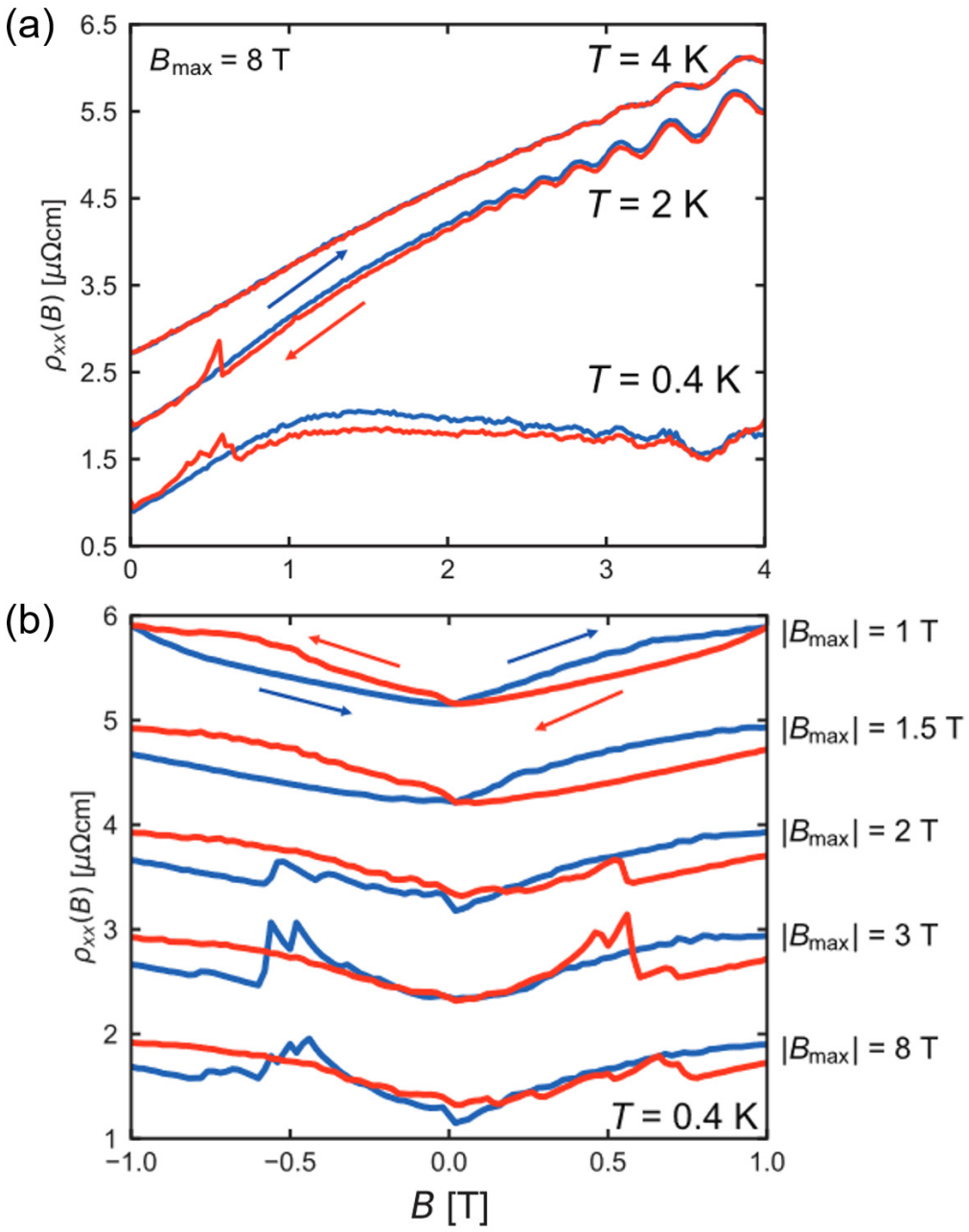

FIGURE 3.2: (a) The hysteresis in the MR observed below T_{N1} in the field range of 4 T (device S1). (b) The external field dependence of the MR hysteresis for various maximum applied fields $|B_{max}|$ (device S2).

3.2.1 Magnetic hysteresis

First, we will discuss the hysteresis observed in the MR. Below T_{N1}, a clear magnetic hysteresis was observed in the MR with a sharp peak structure at $B \approx 0.6$ T, as shown in Fig. 3.2(a). The magnetic hysteresis vanishes above $B \approx 4$ T, and the sharp peak appears only when B is swept from a high enough field (in this case, $B_{max} = 8$ T) to zero field, which we call the negative field sweeping. Note that the magnetic hysteresis is reproducible for other $CeTe_3$ thin film devices, even below T_{N2}, and also when the applied magnetic field is negative, as shown in Fig. 3.2(b). Furthermore, the peak amplitude depends on the absolute value of B_{max}. At $T = 0.4$ K, when $|B_{max}|$ is smaller than 1.5 T, the peak at $B \approx 0.6$ T vanishes, while it clearly shows up with the hysteresis behavior, as shown in Fig. 3.2(b). Such a hysteresis has never been reported previously in bulk $CeTe_3$ as well as in other RTe_3 devices. Although it is difficult to determine the origin of such a phenomenon, one possible origin could be due to some interface contributions to the electrical transport. For example, a hysteresis closely resembling our measurements has been observed for MR measurements in $CeTe_2$, which is a material close to $CeTe_3$. $CeTe_2$ has the same crystal structure as $CeTe_3$, but has a single Te layer instead of the double Te layers. Under its magnetic transition temperature, $CeTe_2$ is known to order ferrimagnetically, with an down-up-up-down spin structure along the layer stacking direction [90, 91]. This is different from the magnetic order of bulk $CeTe_3$, where the magnetic moments at the Ce sites in the two magnetic phases are believed to be aligned to the basal plane. In $CeTe_2$, a butterfly-shaped MR hysteresis has been reported in its bulk transport, which closely resembles our present data [92]. Furthermore, such a butterfly-shaped MR hysteresis has also been observed in another metallic AFM Ag_2CrO_2 [70]. In the case of Ag_2CrO_2, the MR hysteresis also likely originates from magnetic moments which are slightly canted along the

stacking direction of the material, which would switch its magnetization as the external field is applied. One possible scenario to explain the MR hysteresis and peak structure observed in $CeTe_3$ is that the electrical transport effects owing to the magnetic anisotropy along the stacking direction of the material are being observed, resulting in a similar MR effect to $CeTe_2$ or Ag_2CrO_2. The origin of the out-of-plane anisotropy is still under investigation, but a fact to consider is that the cleavable van-der-Waals layer is the Te bilayers for $CeTe_3$. This means that the interface of the $CeTe_3$ thin films closely resembles that of $CeTe_2$, which may result in some canted spins at the interface. It should also be noted that there are reports where the perpendicular anisotropy of a van der Waals ferromagnet Fe_5GeTe_2 [93] is enhanced by making it atomically thinner. We believe that by thin film fabrication, we have either induced canting of the magnetic moments, or there exist some canted magnetic moments at the interface which significantly affects the transport properties only in the thin film devices. In order to elucidate more details, it would be desirable to perform further experiments about the thickness dependence of the peak structure.

3.2.2 Quantum oscillation

Next, we focus on the quantum oscillation observed in the MR. A clear oscillation was observed in the MR at the external magnetic field higher than 4 T. The oscillation was observed from roughly 20 K down to the lowest temperature of 0.4 K. With decreasing the temperature, an increase in the amplitude of the MR oscillation was observed, and below T_{N2}, the field dependence of the oscillation had changed significantly. Such characteristic behavior is shown in Fig. 3.3. The observed oscillations are known as Shubnikov-de Haas (SdH) oscillations. The origin of the oscillations can be traced back to

the formation of quantized energy levels within the material. When the material is highly metallic that the conduction electrons can undergo a complete cyclotron motion in the presence of an external field, it leads to a quantization of the conduction electron energy levels known as the Landau energy levels. Given that the electrical transport of the material is governed by the density of states near the Fermi surface, an oscillation in the resistivity is observed as the Landau levels pass through the Fermi surface of the material.

In general, SdH oscillations are described using the Lifshitz-Kosevich (LK) equation,

$$\Delta\rho' \propto \frac{\lambda(B)T}{\sinh(\lambda(B)T)} e^{-\lambda(B)T_{\mathrm{D}}} \cos\left\{2\pi\left(\frac{F}{B} - \frac{1}{2} + \beta + \delta\right)\right\}, \tag{3.1}$$

where $\Delta\rho'$ is the oscillatory part of MR. T_{D} is the Dingle temperature which corresponds to the blurring of the Landau levels, F is the frequency, $2\pi\beta$ is the Berry phase, and δ is a phase shift which is 0 and $\pm\frac{1}{8}$ for 2D and 3D systems, respectively. $\lambda(B) = (2\pi^2 k_B m^*)/(\hbar e B)$, where k_B is the Boltzmann constant, m^* is the effective cyclotron mass, $\hbar$ is the reduced Plank's constant, and e is the elementary charge. From the analysis of SdH oscillations, we can identify features of the Fermi surface of the material such as its topology and structure, and also gain an understanding of the characteristic of the conduction electrons such as the effective mass and mobility.

First, we discuss the behavior of the SdH oscillation above T_{N2}. Figure 3.3(a) shows the MR with $\rho_{xx}(B = 0)$ subtracted. A clear SdH oscillation was observed in the temperature range from 20 to 2 K. As SdH oscillations are periodic to the inverse of the applied field, we have plotted the observed SdH oscillation as a function of the inverse of B and performed fast Fourier transform (FFT), as shown in Fig. 3.4. A single frequency peak has been obtained at 34 T, which is about two times smaller than that of $GdTe_3$.

The frequency of SdH oscillations are proportional to the extremal cross

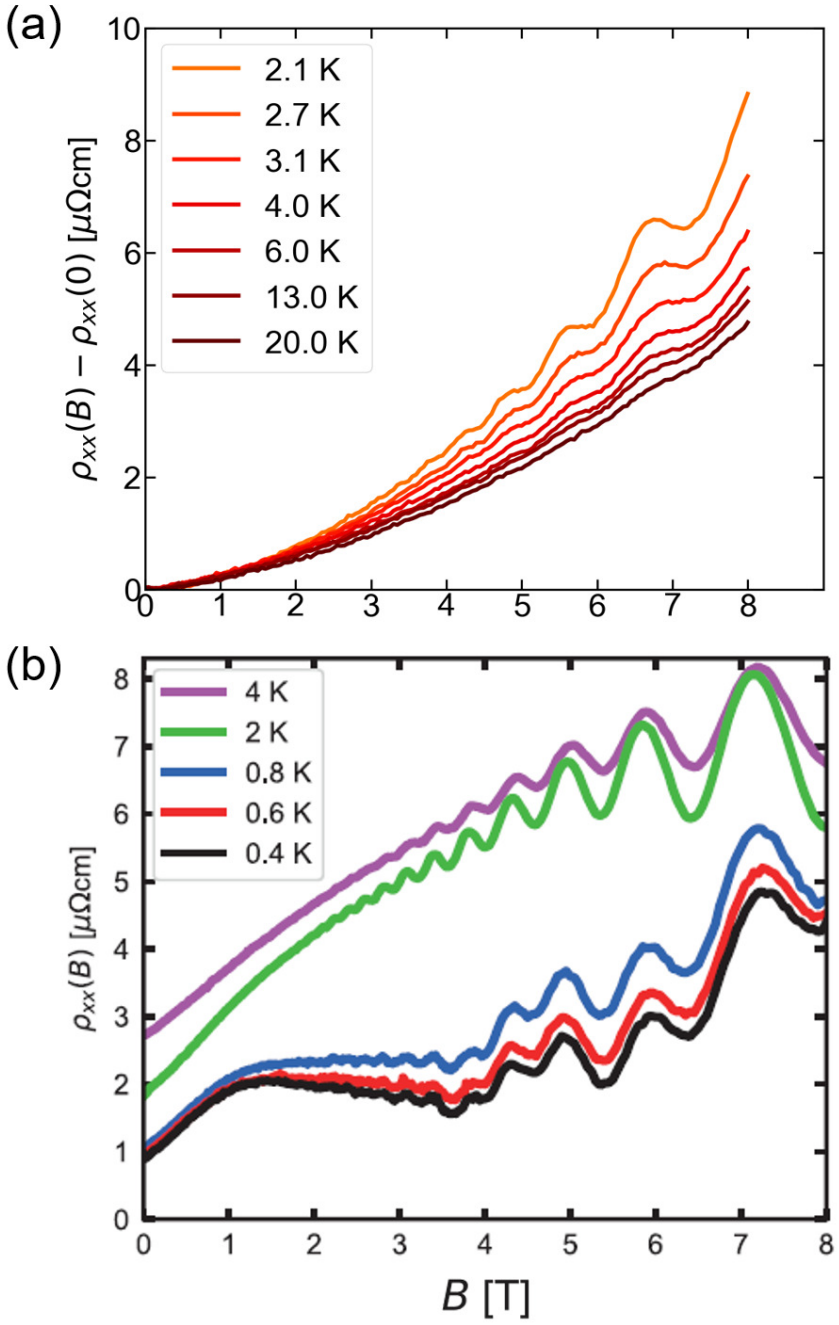

FIGURE 3.3: (a) Shubnikov-de-Haas oscillations observed above T_{N2}. The zero field resistivity is subtracted for clarity (Device S3). (b) Quantum oscillations observed below T_{N2} (Device S2).

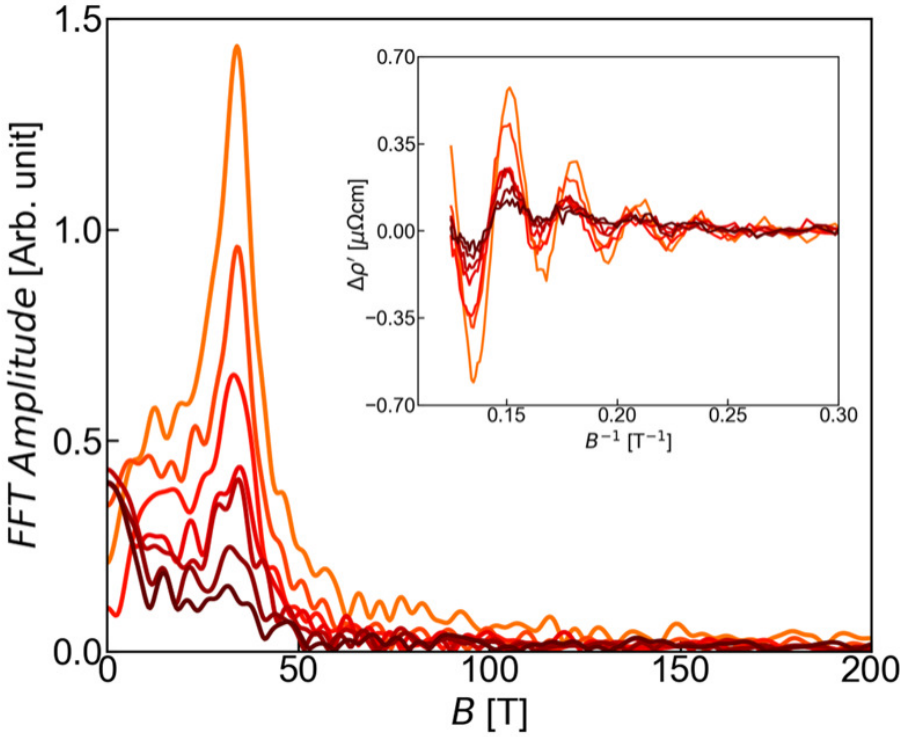

FIGURE 3.4: The FFT amplitude obtained from the oscillatory component of the longitudinal resistivity, as shown in the inset (device 3).

sectional areas of the originating Fermi pocket: $S = 2\pi ef/\hbar$, where S is the Fermi surface area and f is the frequency in the unit of T. Using this equation, it is shown that the low frequency quantum oscillation originates from a Fermi surface pocket which occupies only 0.15% of the entire Brillouin zone. The existence of such a small Fermi pocket is likely due to a Fermi structure often labeled as the α pocket in RTe_3. This Fermi surface structure has been observed in a number of rare-earth tri-tellurides including $GdTe_3$ and $LaTe_3$, and originates from the reconstruction of the Fermi surface due to the charge density wave formation.

Next, we discuss the temperature dependence of the oscillation amplitude above 2 K, from which the effective mass and mobility of the conduction electrons are obtained. At a constant applied field B_0, the amplitude of the SdH oscillation attenuates as a function of T with a factor of $\lambda(B_0)T/\sinh(\lambda(B_0)T)$, and a fit of this function to the FFT amplitude allows for the estimation of

the effective cyclotron mass of the electron. The mean value of the analyzed magnetic field range $B_0 \approx 5.5$ T was used for the FFT fit.

Figure 3.5(a) shows the temperature dependence of the FFT amplitude for different devices. First, we discuss the behavior observed for device S3. At temperatures above T_{N1}, the FFT amplitude follows the attenuation behavior described in the LK formula. Meanwhile, the behavior deviates below the magnetic transition temperature T_{N1}, with FFT amplitudes rapidly increasing roughly by a factor of 3 in a temperature range between 2.1 and 4 K. The deviation from the LK formula below T_{N1} has also been observed previously in related materials such as $GdTe_3$, but its behavior is notably different. In $GdTe_3$, the FFT amplitude plateaus under its magnetic transition temperature. On the other hand, a rapid enhancement of the FFT amplitude was observed below T_{N1} in $CeTe_3$. In the temperature dependent attenuation function of the LK formula (i.e., the prefactor of Eq. (4.1)), the only free parameter is the effective cyclotron mass. Therefore, if we assume that the LK formula holds even under the magnetic ordered state, the natural conclusion would be that the effective cyclotron mass of the conduction electrons are somehow modified due to the interaction between the magnetic ordering of $CeTe_3$ and the conduction electron. Therefore, a separate fit of the attenuation function has been made for temperatures below T_{N1}. The green and blue curves shown in Fig. 3.5(a) are the fits to the attenuation function below and above $T_{N1} \approx 3$ K for device S3. It should be noted that this enhancement of the amplitude below T_{N1} is reproducible with multiple devices of different thicknesses (device S1 and S2). For both devices, the FFT amplitude is enhanced below T_{N1} roughly by a factor of 2, clearly deviating from the paramagnetic fit.

Using least squares fitting to the attenuation function, the effective cyclotron mass m^* can be obtained: above T_{N1}, $m^* \approx 0.061 m_e$ and below T_{N1}, $m^* \approx 0.43 m_e$ where m_e is the electron rest mass. Interestingly, m^* is enhanced

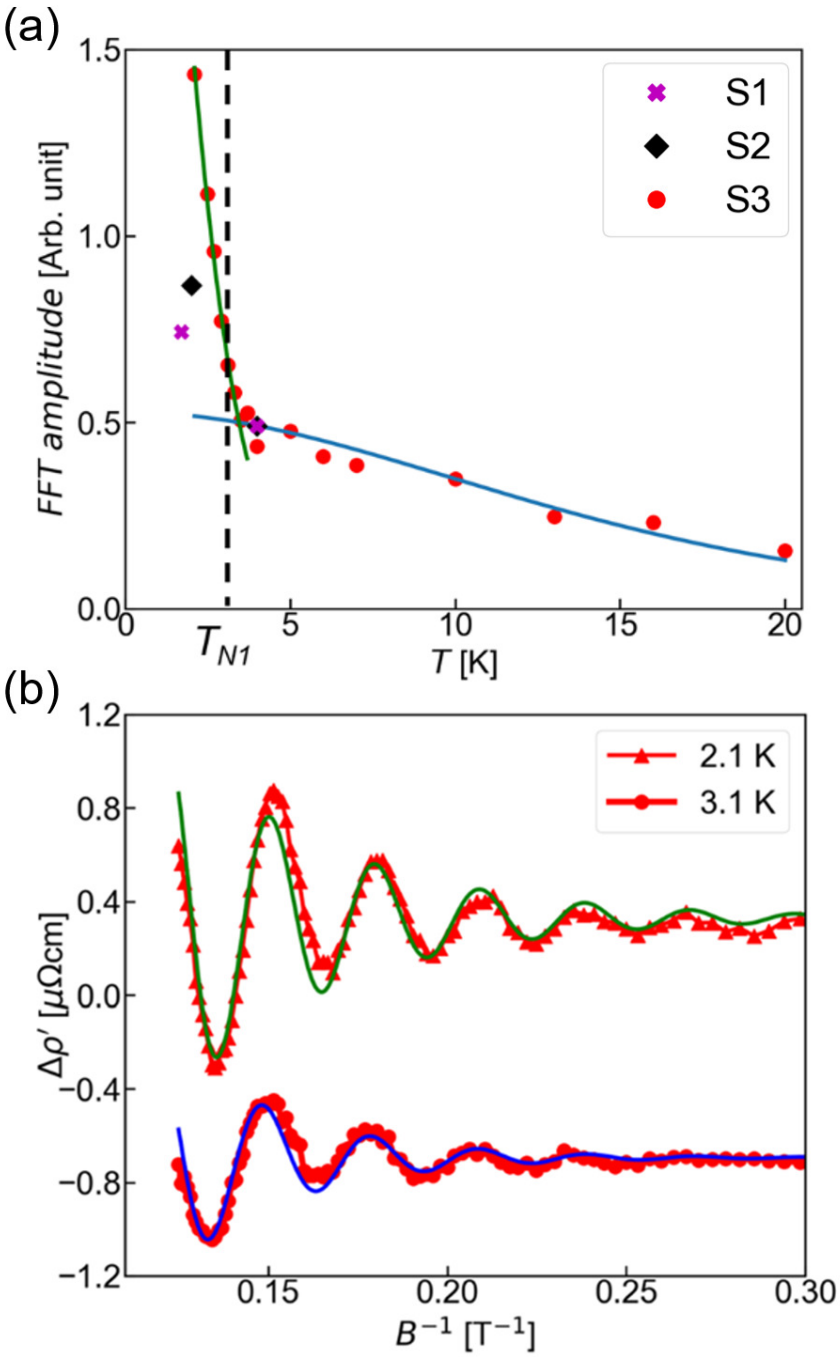

FIGURE 3.5: (a) Temperature dependence of the FFT amplitude, along with the fit of the Lifshitz-Kosevich formula attenuation function. (b) Refitting of the SdH oscillation with the use of the obtained effective mass.

by a factor of 7 below T_{N1}. As the effective mass should reflect the band curvature, one possibility for the origin of the enhancement could be attributed to a modulation of the Fermi surface. Although the details of the Fermi surface modulation from a magnetic order is still under analysis, the magnetic order in $CeTe_3$ would strongly be coupled to the CDW order, leading to a modulation of the CDW state below T_{N1} and therefore a modulation in the Fermi surface.

With an estimate of the effective mass, the oscillatory part of the MR can be refitted by the LK formula, as shown in Fig. 3.5(b). From this fitting, we can estimate the Dingle temperature T_D and the phase shift $\beta + \delta$. $\beta + \delta$ provides information about the topology of the band structures, while T_D enables us to calculate quantum lifetime and mobility, i.e., how much the conduction electrons are scattered and how well defined the Landau levels are. We obtain $T_D = 32$ K and $\beta + \delta = 1.1$ for 3.1 K, and $T_D = 2.2$ K and $\beta + \delta = -0.13$ for 2.1 K. The value of $\beta + \delta$ is close to 1 or 0 in both paramagnetic and antiferromagnetic states, which indicates a Berry phase of 2π and a topologically trivial band structure. The estimations of quantum lifetime and mobility given as $\tau_q = \hbar/(2\pi k_B T_D)$ and $\mu_q = e\tau_q/m^*$ respectively are 3.8×10^{-14} s and 1100 $cm^2V^{-1}s^{-1}$ for the paramagnetic state and 5.5×10^{-13} s and 2300 $cm^2V^{-1}s^{-1}$ for the antiferromagnetic state. These values are quantitatively consistent with those of bulk $GdTe_3$ with the mobility of $1200 - 2000$ $cm^2V^{-1}s^{-1}$, which is amongst one of the highest mobility observed for atomically layered magnetic thin films. Although the effective cyclotron mass increased under the antiferromagnetic state, T_D also increased, resulting in a larger quantum lifetime and mobility in the antiferromagnetic state compared to the paramagnetic state. The increase in the mobility of the electrons possibly originates from the loss of paramagnetic scattering, also observed as a large drop in $\rho(T)$ below T_{N1} (see Fig. 3.1(a)).

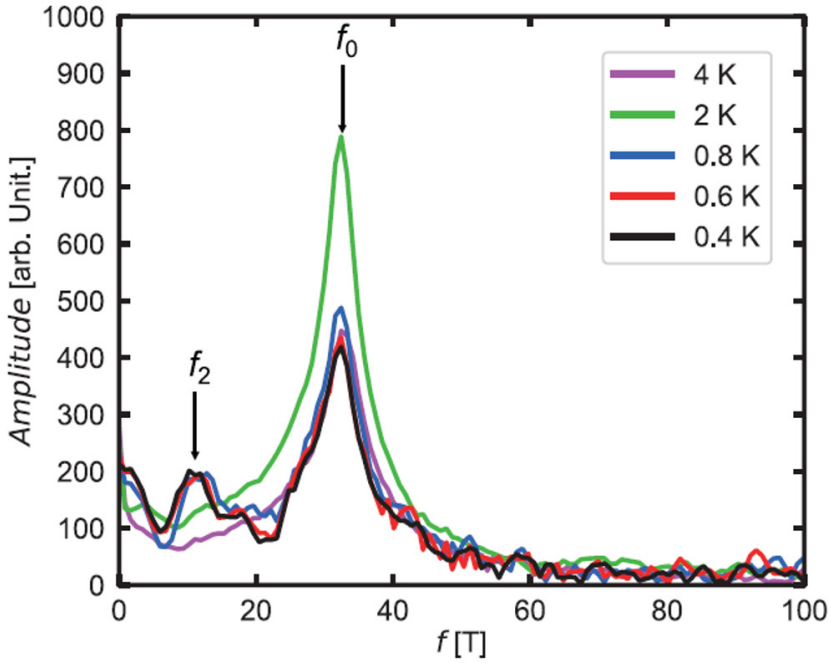

FIGURE 3.6: The temperature dependence of the FFT amplitude down to 0.4 K.

Finally, we discuss the SdH oscillations below T_{N2}, specifically the drastic change in the external field dependence of the oscillation as shown in Fig. 3.3(b). By performing the FFT analysis explained above, it was shown that an second frequency peak was observed at $f_2 = 11.0$ T in addition to the original frequency peak f_0, which corresponded to a pocket size of $S_2 = 1.05 \times 10^{13}$ cm^{-2} and roughly 0.04% of S_{tot}, as shown in Fig. 3.6. This SdH oscillation is previously unreported in any bulk RTe_3, and since the frequency of the SdH oscillation corresponds to the shape of the Fermi surface, this data indicates a further modulation of the Fermi surface which is induced by the long range magnetic order below T_{N2}. Further investigation of the low temperature Fermi surface such as angle-resolved photoemission spectroscopy (ARPES) measurements are anticipated to further elucidate the details of this unique phenomenon.

Chapter 4

Magnetotransport induced by spin fluctuations in Ag_2CrO_2 devices

In this Chapter, we focus on the magnetoresistance (MR) and Hall measurements of atomically layered triangular-lattice antiferromagnet Ag_2CrO_2 [65]. This is one of the few triangular-lattice antiferromagnets with a high electrical conduction, which allows for observation of unique electrical transport properties originating from an exotic magnetic structure. In Ag_2CrO_2, a unique magnetic ordering occurs due to from strong further-neighbor interactions and geometrical frustration. Below the Néel temperature $T_N = 24$ K, Ag_2CrO_2 has an antiferromagnetic ordering with a 5 sub-lattice magnetic unit cell, where the $S = 3/2$ spins at the Cr^{3+} sites possess a magnetic structure known as the partially disordered (PD) structure. In this structure, one in five spin sites is known to remain as an effective free spin even under its antiferromagnetic order [67, 94]. In this magnetic state, a minuscule but finite magnetization hysteresis is observed at 0.5 T, and the magnetization shows a plateau of $\sim 0.4\ \mu_B/Cr^{3+}$ under an applied magnetic field of 8 T which may indicate the presence of some unsaturated moments at the PD spin sites even under high magnetic fields [68].

Despite these unique properties, experiments on the electronic properties of this material had been limited due to the fact that the bulk material is

inherently poly-crystalline. Recently, our colleague reported successful fabrication of nearly mono-crystalline samples using the mechanical exfoliation technique, which allows us to probe the electronic properties of high quality Ag_2CrO_2 through nanofabrication [69, 70]. In this work, we measured the MR and Hall effect in Ag_2CrO_2 thin-film devices up to 8 T in the temperature range from 5 to 100 K, in order to obtain further information on the electrical transport and magnetic properties. In addition to a large negative MR near T_N, an anomalous Hall effect (AHE) is induced only in the vicinity of T_N. These results imply that fluctuations of the magnetic moments play a key role in the generation of the observed AHE. Therefore, we propose and discuss possible scenarios in which the fluctuations of the magnetic moments may lead to such behavior, such as the fluctuation-enhanced skew scattering mechanism or spin scalar chirality formed by a non-coplanar spin structure.

4.1 Evaluation of device through resistivity measurements

First, we show the temperature dependence of the resistivity of a typical Ag_2CrO_2 thin-film device in Fig. 4.1. As already demonstrated in previous studies [65, 69, 70], a characteristic drop in the resistivity is observed with the onset of the antiferromagnetic order, which is caused by the large suppression of the magnon scattering. The difference from the previous reports is the resistivity at low temperature: it is nearly two orders of magnitude smaller than that of poly-crystalline samples [65, 68]. This improvement is due to the fact that the device is nearly mono-crystalline quality. It should be noted that the resistivity of 0.7 $\mu\Omega$·cm at $T = 5$ K is almost the lowest in mesoscopic scale metals, comparable or even lower to that of pure Au or Ag.

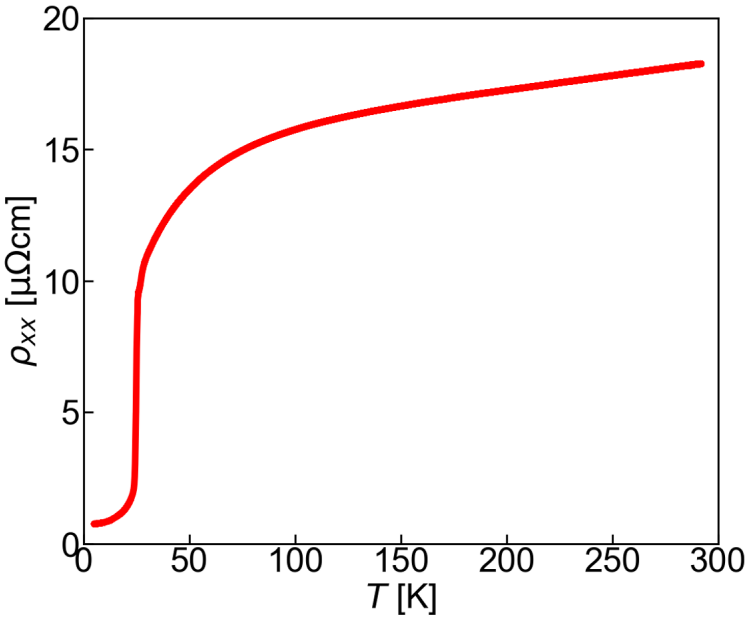

FIGURE 4.1: Electrical resistivity of a typical Ag_2CrO_2 thin-film device.

4.2 Effect of magnetic moment fluctuations in the magnetoresistance

Next we performed MR and Hall measurements in the temperature range of 5 - 44 K up to 8 T. In Fig. 4.2, the longitudinal MR at notable temperatures are displayed. At the lowest measured temperature ($T = 5.4$ K), a large positive MR of $+80\%$ was observed. A positive MR well below the transition temperature often occurs in magnetic materials due to the Lorentz force. It usually shows a parabolic field dependence at low temperatures when the electron mean free path is long enough to overcome the negative MR caused by the suppression of spin scattering. It should be noted that the positive MR observed in Ag_2CrO_2 does not show a simple quadratic dependence with respect to the magnetic field and saturates at high fields, suggesting a different origin from the Lorentz force contribution, but may be related to the antiferromagnetic structure [95, 96].

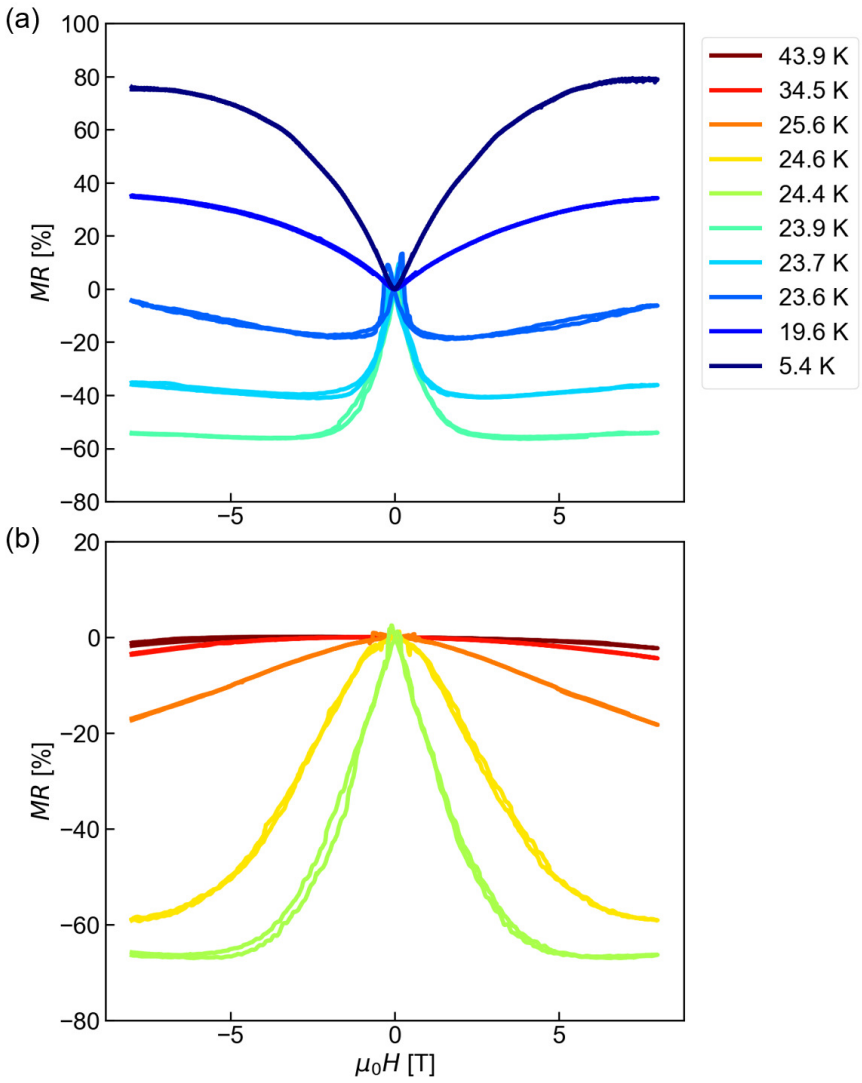

FIGURE 4.2: Magnetoresistance (MR) measurements (a) below and (b) above T_N. The magnetic field is applied along the stacking direction of the material.

As the temperature is increased, the emergence of the negative MR is observed, which does not saturate up to 8 T in the case of $T = 24.6$ K. Such behavior can also be seen in other magnetic materials, where the fluctuations of the magnetic moments near its transition temperature induce spin scattering, and are suppressed with the application of the external field, leading to a decrease in the magnetic scattering and the emergence of a negative MR [97, 98]. The negative MR takes a maximum absolute value of 65% in the vicinity of T_N, suggesting that the fluctuations of the magnetic moments are largest in this temperature range. It is also striking that the maximum MR ratio difference of roughly 140% is achieved between 5 K and 24 K due to the large positive and negative MR.

4.3 Unconventional anomalous Hall effect

The Hall resistance of Ag_2CrO_2 were taken simultaneously with the MR. In Fig. 4.3(a), we show the Hall resistivity ρ_H as a function of the perpendicular magnetic field at notable temperatures. Since the raw data contains some longitudinal component, the asymmetric component of the raw data is taken as ρ_H and plotted in Fig. 4.3(a).

No significant hysteresis was observed in our Hall measurement throughout the entire temperature range. The carrier type is electron, which is consistent with the previous studies where the Ag 5*s* band provides the conduction carriers in Ag_2MO_2 (M = magnetic ion) materials [99–101]. Along with the ordinary Hall effect, some nonlinear component was observed in the temperature range close to T_N. First, the ordinary Hall component was analyzed through a linear fit above 6 T, where the magnetization of the bulk material roughly plateaus. Assuming a single carrier model, the temperature dependence of the electron carrier concentration was obtained as Fig. 4.3(b). The carrier concentration was calculated as $0.9 - 1.5 \times 10^{22}$ cm^{-3}, which is

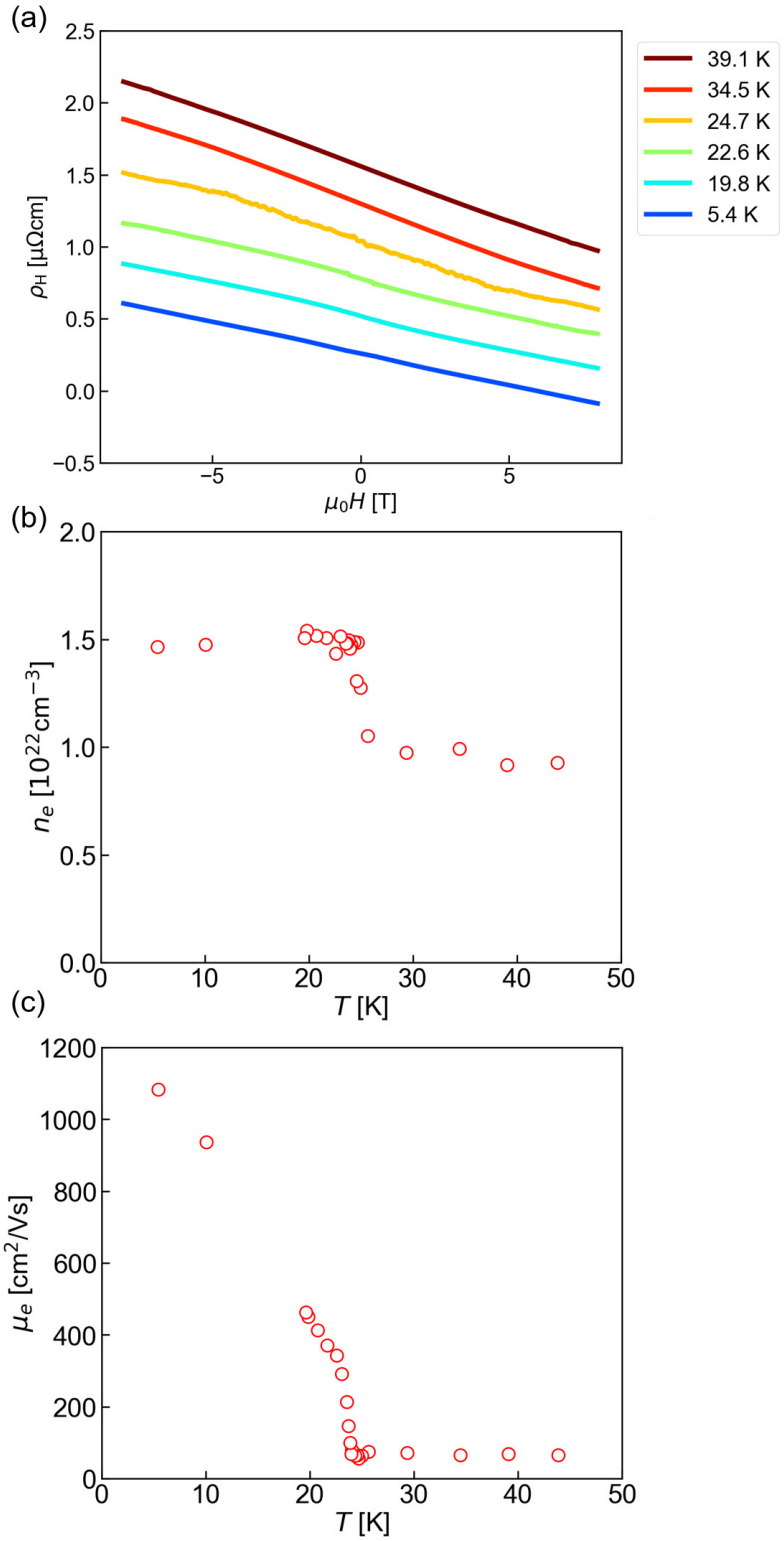

FIGURE 4.3: (a) Hall resistivity ρ_H at notable temperatures. (b) Temperature dependence of carrier concentration obtained from the linear fit at high fields. (c) Temperature dependence of electron mobility.

in the same order of magnitude as the carrier concentration of Ag ($5 - 6 \times 10^{22}$ cm^{-3}). Making use of the effective electron mass obtained from the zero field longitudinal resistivity, the temperature dependence of the electron mobility can also be obtained, as shown in Fig. 4.3(c). Similar to the large drop in the resistivity at T_N, an enhancement in the mobility by a factor of roughly 4 is observed between $T = 23.1$ and 25.7 K. This is further supportive evidence of large fluctuations of magnetic moments which are suppressed below T_N, leading to a notable increase in the mobility. The maximum value of the mobility in Ag_2CrO_2 exceeds 1080 cm^2/V·s, which is comparable to crystalline silicon at room temperature of roughly 1400 cm^2/V·s [102].

Now we analyze the anomalous Hall component defined as ρ_{AHE}, by subtracting the ordinary Hall effect from ρ_H, which is shown in Fig. 4.4(a) for notable temperatures. While the anomalous Hall contributions from the minuscule magnetization hysteresis around 0.5 T were not observed, a saturation of the anomalous component was observed for fields above 5 T. Figure 4.4(b) shows the temperature dependence of ρ_{AHE}^{sat}, which has a sharp peak in the vicinity of T_N. This is clearly different from the behavior of the bulk magnetization, which shows a small but finite hysteresis loop below $T = 20$ K. This behavior is also unlikely to be a multi-carrier effect because it is notable only in the vicinity of T_N.

Since the longitudinal resistivity changes drastically within this temperature range as shown in Fig. 4.1, we show the temperature dependence of the AHE angle $\tan\theta_{AHE} = \rho_{AHE}^{sat}/\rho_{xx}$ in Fig. 4.5(a). The striking result is the fact that $\tan\theta_{AHE}$ takes a maximum value of $2 - 4\%$, depending on the device quality. As the difference in device quality leads to changes in the longitudinal resistivity, we have plotted the scaling relation between σ_{AHE} and σ_{xx} between $20 - 40$ K where the Hall angle shows the unique temperature dependence. This is shown in Fig. 4.5(b). σ_{AHE} shows a clear σ_{xx} dependence throughout all the measured devices. The power law fit results in a fitted

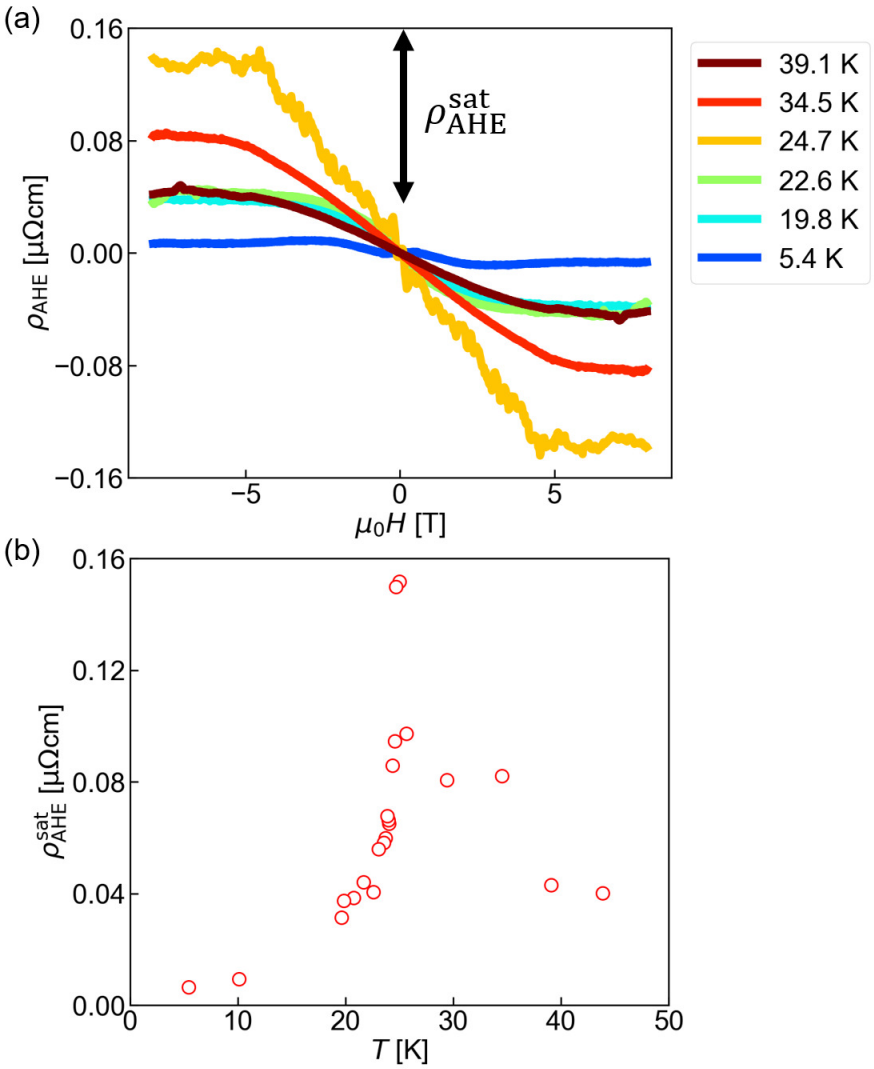

FIGURE 4.4: (a) Anomalous component of the Hall resistivity ρ_{AHE} with the definition of ρ_{AHE}^{sat}. (b) Temperature dependence of saturated ρ_{AHE}^{sat}.

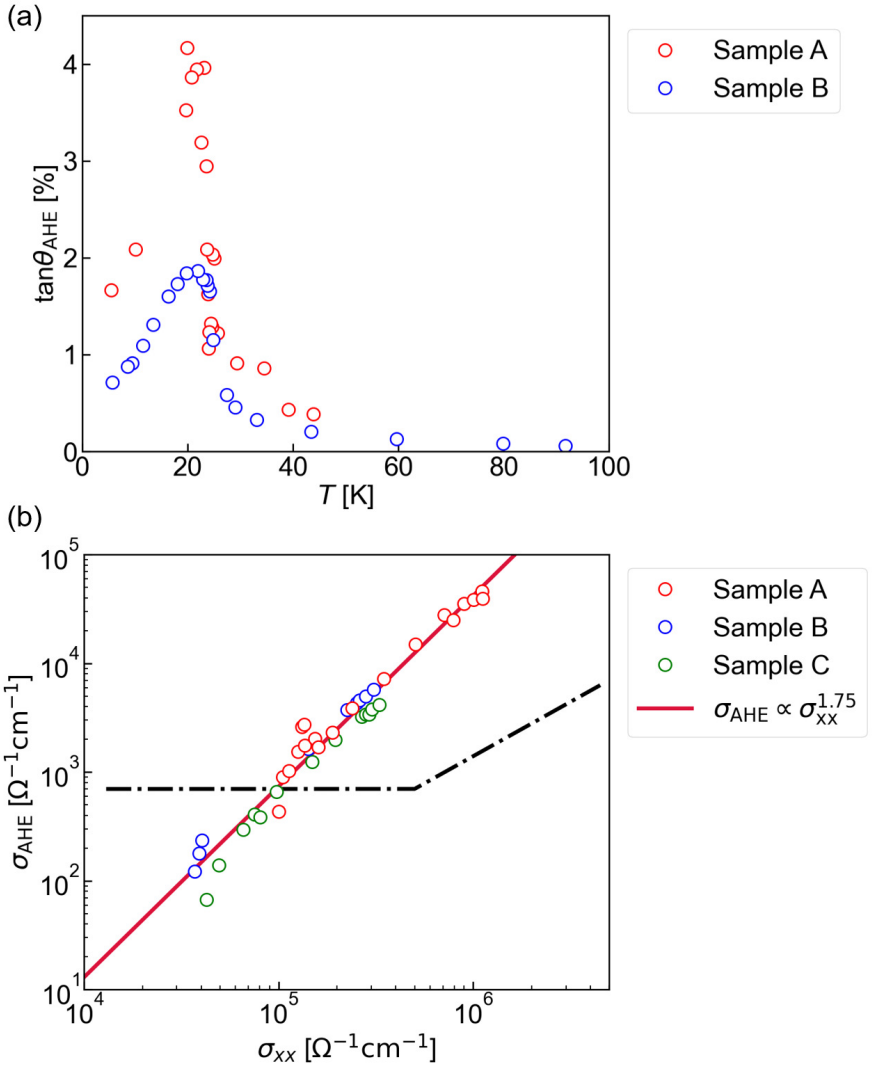

FIGURE 4.5: (a) Temperature dependence of the AHE angle $\tan\theta_{AHE}$. (b) Scaling relation between the longitudinal resistivity σ_{xx} and σ_{AHE}. The red line shows the power law fit and the eye guide (dotted line) indicates the conventional scaling relation observed in magnetic materials [88].

curve of $\sigma_{AHE} \propto \sigma_{xx}^{1.75}$, and such σ_{xx} dependence of σ_{AHE} is observed even in regimes where the intrinsic mechanism should dominate.

4.4 Possible origins of the unconventional anomalous Hall effect

We now discuss the possible origins of the unconventional anomalous Hall effect discussed in the above section. For this purpose, first-principles calculations were performed for Ag_2CrO_2, in order to gain information on the electronic structure and hybridization of Ag- and Cr-orbitals. The calculated band dispersion (Figs. 4.6(a)-(d)) shows that the dispersive Ag-*s* band crosses the Fermi energy, which likely dominates the electrical transport, as is consistent with previous results [99–101]. The density of states (DOS) for the low-temperature structure with the PD magnetic state was also calculated. As shown in Figs. 4.7, whether the Cr-*d* partial DOS remains near the Fermi energy strongly depends on the Hubbard-*U* correction, which is 3 and 0 eV for Figs. 4.7(a) and (b), respectively. In general, it is difficult to evaluate an appropriate *U* value for band-structure calculation. We believe that the real electronic structure lies somewhere in between the two calculations. This is also consistent with previous experimental reports; the Sommerfeld constant for the poly-crystalline bulk was given as 9.74 $mJmol^{-1}K^{-2}$ [65], implying a heavy effective electron mass, while the magnetic moment of the ordered Cr sites showed an almost full saturation of $2.9\mu_B$ [66], indicating an almost full saturation for $S = 3/2$. These two experimental results suggest that there is a finite DOS of the Cr-*d* bands at the Fermi energy, meanwhile the DOS may also be relatively small due to the almost fully occupied t_{2g}^3 state.

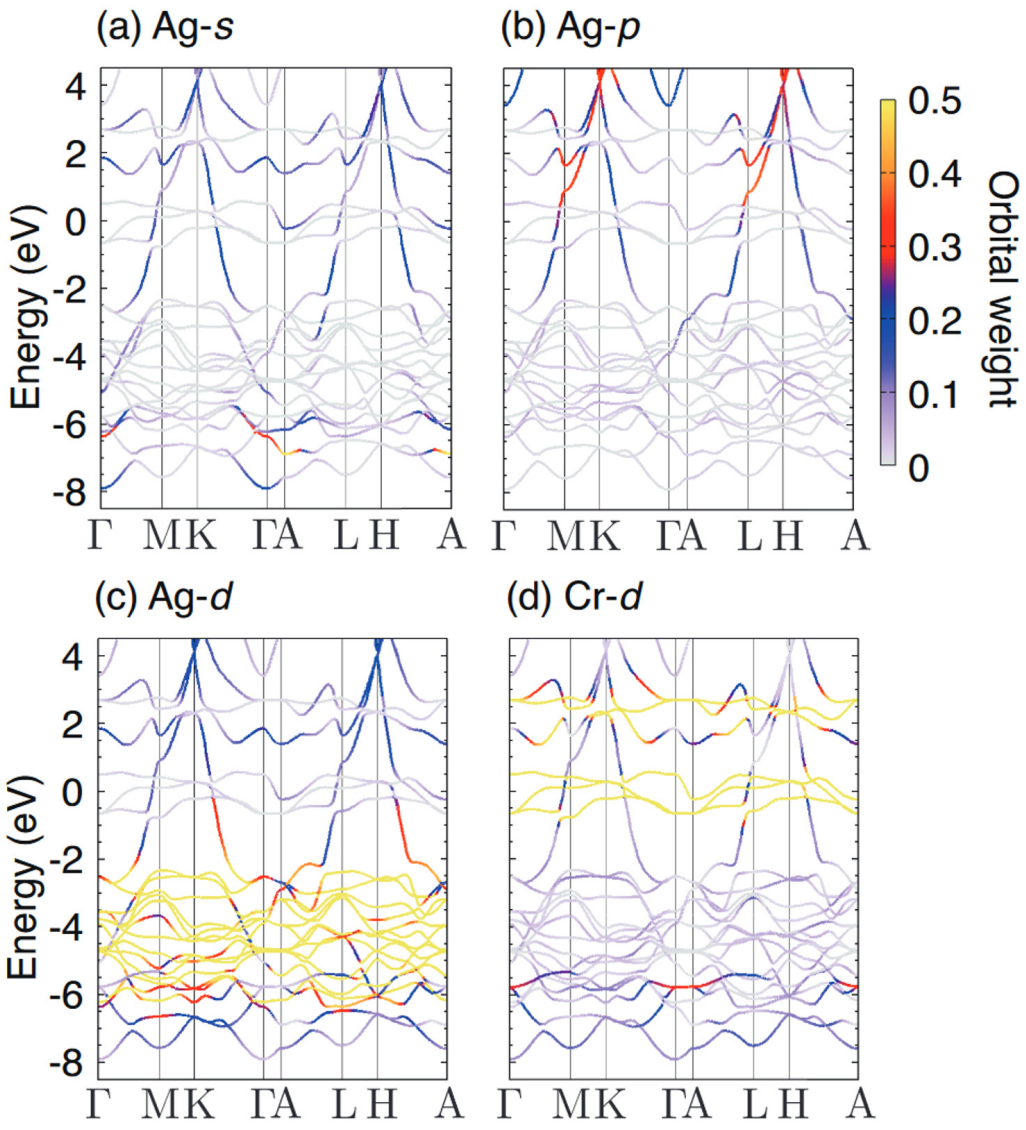

FIGURE 4.6: (a)-(d) Non-magnetic band structure for the trigonal ($P\bar{3}m1$) structure with the Ag-*s*, *p*, *d* and Cr-*d* orbital weights respectively.

Given these band-calculation analyses, we return to the temperature dependence of the AHE angle. As the AHE is maximized at the magnetic transition, it is likely that the effect originates from the fluctuations of the PD moments near T_N. As far as we know, there are two main mechanisms where fluctuations of the magnetic moments can give rise to an enhancement of the AHE. One is the skew scattering enhancement due to thermal fluctuations presented by Kondo [85], and the other is the scalar spin chirality model [103–107]. Both of these effects arise from extrinsic mechanisms, which is consistent with our scaling plot which showed a strong σ_{xx} dependence of the AH conductivity. In the following, we will discuss the feasibility of each mechanism.

As for the Kondo mechanism, the AHE originates from the *s*-*d* interaction in a magnetic material. With consideration of higher order terms in the Born approximation, Kondo showed that the skew scattering of a magnetic material can be enhanced near the magnetic transition temperature [85].

This effect is observed in clean ferromagnetic materials such as Fe or Ni, and has been successful in addressing their AHE temperature dependence. In our case, such a scenario could occur if hybridization between the Ag-*s* band and the Cr-*d* band exists, which could then explain the temperature dependence of the AHE angle in our data. However, the Kondo mechanism is not enough to explain the magnitude of the AHE angle observed in our experiment. This is due to the small partial DOS of the Cr-*d* band at the Fermi surface stated earlier, from which a relatively weak *s*-*d* interaction is expected. Considering the fact that a maximum AHE angle of only 0.1% is observed even for clean ferromagnets such as Fe [16, 108], an AHE angle of a few percent would not be due to the skew scattering mechanism presented by Kondo, especially when the hybridization of Ag-Cr bands may be weak.

Meanwhile, several kagome lattice materials have been reported to possess unconventionally large AHE angles of few tens of percent, owing to the

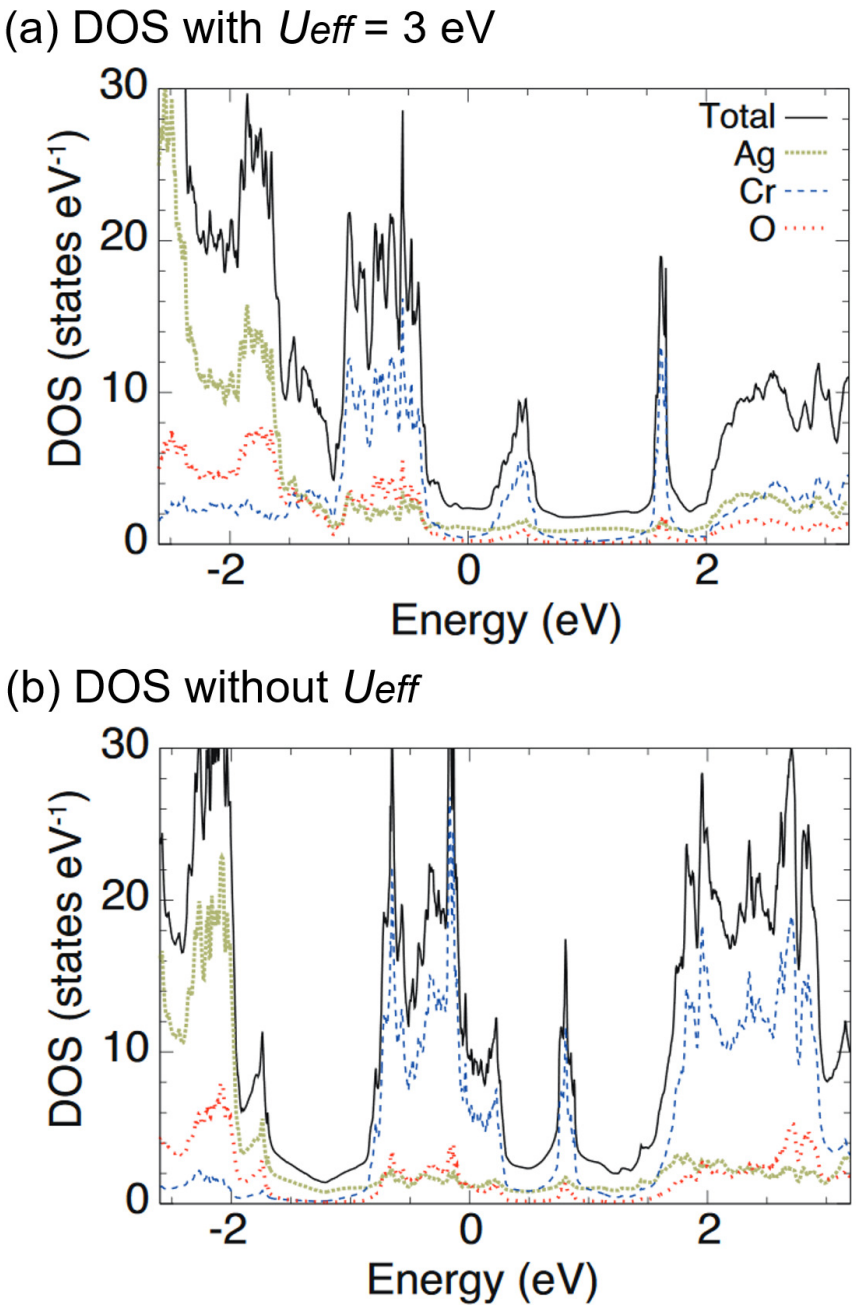

FIGURE 4.7: (a)-(b) Density of states for the monoclinic ($c2/m$) structure with the partially disordered magnetic state. The Hubbard-U correction $U_{eff} \equiv U - J = 3$ eV was included for (a).

scalar spin chirality obtained by the non-coplanar magnetic structure [15, 16]. In the spin scalar chirality mechanism, a non-coplanar spin structure can obtain a finite Berry curvature, leading to an AHE which is not simply proportional to the magnetization. It has also been shown theoretically that the skew scattering due to the non-coplanar structure can be greatly enhanced with the aid of thermal fluctuations of the magnetic moments [109]. Therefore, the temperature dependence of the AHE and the magnitude of the AHE angle could also be explained if there exists some non-coplanar structure in our system. However, the problem in this scenario lies in the determination of the magnetic structure which possesses such scalar spin chirality. In order to fully explain the observed phenomena, further refinements of the PD model may be required, such as the inclusion of canting of the ordered moments or expansion of the model to three-dimension, or consideration of other mechanisms other than the two presented in the current section may be essential.

Chapter 5

Conclusions and perspectives

In this thesis, we have performed electrical transport measurements of atomically layered magnetic materials in order to investigate and observe unique transport properties arising from the thin-film devices. Specifically, we have focused on two atomically layered antiferromagnets with high mobility. One is the rare-earth antiferromagnet $CeTe_3$, and the other is the triangular lattice antiferromagnet Ag_2CrO_2. Below, we give a brief summary of the experimental results for each material.

For the rare-earth antiferromagnet $CeTe_3$, we measured the magnetoresistance of $CeTe_3$ thin-film devices up to 8 T in the temperature range from 20 to 0.4 K. We have observed two characteristics that were previously unreported in the bulk samples. One is the magnetoresistance hysteresis below $T_{N1} \approx 3.0$ K, indicating the existence of some out-of-plane anisotropy of the magnetic moments. The other is the clear quantum oscillation, originating from a small Fermi pocket due to the formation of the charge density wave. From the temperature dependence of the quantum oscillation amplitude, it was shown that the effective mass was enhanced by a factor of roughly 7 at temperatures below T_{N1}, showing a significant modulation of the Fermi surface. Meanwhile, a notable enhancement in the mobility is also observed below T_{N1}, likely due to the suppression of the paramagnetic scattering. This results in a mobility of 2300 $cm^2V^{-1}s^{-1}$, which is amongst one of the highest mobilities observed for atomically layered magnetic thin films. Below

$T_{N2} \approx 1.2$ K, on the other hand, an additional oscillation frequency was observed, suggesting further modulation of the Fermi surface. The results on the quantum oscillations show a notable modulation of the electronic structure by the magnetic ordering, which is possibly mediated by the coupling between the charge density wave state and the magnetic state.

For the triangular lattice antiferromagnet Ag_2CrO_2, we simultaneously measured the magnetoresistance and Hall effect up to 8 T in the temperature range from 100 to 5 K. In the magnetoresistance measurement, a large positive magnetoresistance was observed well below $T_N \approx 24$ K, possibly related to the antiferromagnetic structure. On the other hand, a substantially large negative magnetoresistance was observed near the Néel temperature T_N. The result indicates large fluctuations of the magnetic moments in this temperature range. In the same temperature range, a nonlinear component in the Hall effect was observed. The obtained Hall angle $\tan\theta_{AHE}$ reaches 4%, and its scaling relation with respect to the longitudinal conductivity indicates that this effect arises from extrinsic scattering mechanisms. It is strongly indicated that the fluctuating moment near T_N plays a key role in the unique anomalous Hall effect, although further researches on the partially disordered state in Ag_2CrO_2 are required to fully elucidate the origin. The result is one of the few experimental reports on electrical transport of metallic triangular lattice magnetic systems, and demonstrates the unique magnetotransport properties arising from conduction electrons which are coupled to exotic magnetic structures. It also demonstrates that mechanical exfoliation is a useful tool which provides access to magnetic thin-film devices with high crystallinity.

Through the electrical transport of these two atomically layered antiferromagnets, we have showcased the emergence of novel electrical transport phenomena which can only be accessed in the thin-film devices. Furthermore, it should be noted that these results also provide information on the intrinsic nature of the magnetic and electronic physics of these materials, such

as the notable modulation of the electronic structure with the onset of magnetic order in $CeTe_3$, or the significant presence of magnetic moment fluctuation in Ag_2CrO_2. Therefore, exploration of transport effects in the atomically layered magnetic thin-film devices are important from the viewpoints of fundamental condensed matter physics as well as of future device applications.

Lastly, we discuss some perspectives towards future research. For $CeTe_3$, the thickness dependence of the magnetoresistance is highly desired to gain further information on the nature of the magnetoresistance hysteresis, and also to observe the quantum oscillation in the bilayer or monolayer limit. Additionally, Hall measurements are desired to elucidate whether the properties of the conduction carriers are altered by the onset of magnetic order. Furthermore, spin transport measurements in $CeTe_3$ would be particularly interesting. Since this material possesses high mobility, a long spin diffusion length might be expected which could be especially useful for nonlocal spin transport experiments. It is also important that the f-orbital is responsible for the magnetic moments in $CeTe_3$. For such a case, a large spin-orbit interaction can be expected, which implies a large response in the spin transport properties of this material such as the inverse spin Hall effect. Therefore, this material could be a good potential candidate towards the development of "f-orbital" spintronics.

As for Ag_2CrO_2, we have limited the investigation of the high-field transport properties to the external field applied along the c-axis in the present research. Research on the in-plane anisotropy is also an interesting topic for this material, especially since the unconventional anomalous Hall effect suggests that the model with a simple Ising spin along the c-axis may not be sufficient to explain the observed phenomena. Furthermore, spin transport in this material would also be interesting. This is because the response of the inverse spin Hall effect is known to be extremely sensitive to the fluctuation of the magnetic moments [110, 111]. We can expect further exotic behavior

in the spin transport properties, since the electrical transport measurements already suggest large fluctuation in the vicinity of T_N, which strongly affects the properties of the conduction electrons.

Bibliography

[1] K. S. Novoselov, A. K. Geim, S. V. Morozov, D. Jiang, Y. Zhang, S. V. Dubonos, I. V. Grigorieva, and A. A. Firsov, Science **306**, 666–669 (2004).

[2] K. S. Novoselov, A. Mishchenko, A. Carvalho, and A. H. C. Neto, Science **353**, aac9439 (2016).

[3] K. S. Novoselov, Reviews of Modern Physics **83**, 837–849 (2011).

[4] A. Geim and I. Grigorieva, Nature **499**, 419–425 (2013).

[5] C.-T. Kuo, M. Neumann, K. Balamurugan, H. J. Park, S. Kang, H. W. Shiu, J. H. Kang, B. H. Hong, M. Han, T. W. Noh, and J.-G. Park, Scientific Reports **6**, 20904 (2016).

[6] K.-z. Du, X.-z. Wang, Y. Liu, P. Hu, M. I. B. Utama, C. K. Gan, Q. Xiong, and C. Kloc, ACS Nano **10**, 1738–1743 (2016).

[7] J.-U. Lee, S. Lee, J. H. Ryoo, S. Kang, T. Y. Kim, P. Kim, C.-H. Park, J.-G. Park, and H. Cheong, Nano Letters **16**, 7433–7438 (2016).

[8] X. Wang, K. Du, Y. Y. F. Liu, P. Hu, J. Zhang, Q. Zhang, M. H. S. Owen, X. Lu, C. K. Gan, P. Sengupta, C. Kloc, and Q. Xiong, 2D Materials **3**, 031009 (2016).

[9] B. Huang, G. Clark, E. Navarro-Moratalla, D. R. Klein, R. Cheng, K. L. Seyler, D. Zhong, E. Schmidgall, M. A. McGuire, D. H. Cobden, W. Yao, D. Xiao, P. Jarillo-Herrero, and X. Xu, Nature **546**, 270–273 (2017).

[10] C. Gong, L. Li, Z. Li, H. Ji, A. Stern, Y. Xia, T. Cao, W. Bao, C. Wang, Y. Wang, Z. Qiu, R. Cava, S. G. Louie, J. Xia, and X. Zhang, Nature **546**, 265–269 (2017).

[11] W. Heisenberg, Zeitschrift für Physik **49**, 619–636 (1928).

[12] N. D. Mermin and H. Wagner, Physical Review Letters **17**, 1133–1136 (1966).

[13] P. C. Hohenberg, Physical Review **158**, 383–386 (1967).

[14] N. Nagaosa and Y. Tokura, Nature Nanotechnology **8**, 899–911 (2013).

[15] Y. Fujishiro, N. Kanazawa, R. Kurihara, H. Ishizuka, T. Hori, F. S. Yasin, X. Yu, A. Tsukazaki, M. Ichikawa, M. Kawasaki, N. Nagaosa, M. Tokunaga, and Y. Tokura, Nature Communications **12**, 317 (2021).

[16] S.-Y. Yang, Y. Wang, B. R. Ortiz, D. Liu, J. Gayles, E. Derunova, R. Gonzalez-Hernandez, L. Šmejkal, Y. Chen, S. S. P. Parkin, S. D. Wilson, E. S. Toberer, T. McQueen, and M. N. Ali, Science Advances **6**, eabb6003 (2020).

[17] K. Yumigeta, Y. Qin, H. Li, M. Blei, Y. Attarde, C. Kopas, and S. Tongay, Advanced Science **8**, 2004762 (2021).

[18] V. Brouet, W. L. Yang, X. J. Zhou, Z. Hussain, R. G. Moore, R. He, D. H. Lu, Z. X. Shen, J. Laverock, S. B. Dugdale, N. Ru, and I. R. Fisher, Physical Review B **77**, 235104 (2008).

[19] J. Laverock, S. B. Dugdale, Z. Major, M. A. Alam, N. Ru, I. R. Fisher, G. Santi, and E. Bruno, Physical Review B **71**, 085114 (2005).

[20] D. A. Zocco, J. J. Hamlin, K. Grube, J.-H. Chu, H.-H. Kuo, I. R. Fisher, and M. B. Maple, Physical Review B **91**, 205114 (2015).

[21] E. DiMasi, M. C. Aronson, J. F. Mansfield, B. Foran, and S. Lee, Physical Review B **52**, 14516–14525 (1995).

[22] Y. Iyeiri, T. Okumura, C. Michioka, and K. Suzuki, Physical Review B **67**, 144417 (2003).

[23] K. Deguchi, T. Okada, G. F. Chen, S. Ban, N. Aso, and N. K. Sato, Journal of Physics: Conference Series **150**, 042023 (2009).

[24] M. Watanabe, S. Lee, T. Asano, T. Ibe, M. Tokuda, H. Taniguchi, D. Ueta, Y. Okada, K. Kobayashi, and Y. Niimi, Applied Physics Letters **117**, 072403 (2020).

[25] V. Brouet, W. L. Yang, X. J. Zhou, Z. Hussain, N. Ru, K. Y. Shin, I. R. Fisher, and Z. X. Shen, Physical Review Letters **93**, 126405 (2004).

[26] H. Yao, J. A. Robertson, E.-A. Kim, and S. A. Kivelson, Physical Review B **74**, 245126 (2006).

[27] A. Kikuchi, Journal of the Physical Society of Japan **67**, 1308–1312 (1998).

[28] P. A. Vorobyev, P. D. Grigoriev, K. K. Kesharpu, and V. V. Khovaylo, Materials **12**, 2264 (2019).

[29] S. Lei, J. Lin, Y. Jia, M. Gray, A. Topp, G. Farahi, S. Klemenz, T. Gao, F. Rodolakis, J. L. McChesney, C. R. Ast, A. Yazdani, K. S. Burch, S. Wu, N. P. Ong, and L. M. Schoop, Science Advances **6**, eaay6407 (2020).

[30] N. Ru, C. L. Condron, G. Y. Margulis, K. Y. Shin, J. Laverock, S. B. Dugdale, M. F. Toney, and I. R. Fisher, Physical Review B **77**, 035114 (2008).

[31] C. D. Malliakas and M. G. Kanatzidis, Journal of the American Chemical Society **128**, 12612–12613 (2006).

[32] R. G. Moore, V. Brouet, R. He, D. H. Lu, N. Ru, J.-H. Chu, I. R. Fisher, and Z.-X. Shen, Physical Review B **81**, 073102 (2010).

[33] N. Ru, J.-H. Chu, and I. R. Fisher, Physical Review B **78**, 012410 (2008).

[34] A. A. Sinchenko, P. Lejay, and P. Monceau, Physical Review B **85**, 241104 (2012).

[35] A. V. Frolov, A. P. Orlov, A. Hadj-Azzem, P. Lejay, A. A. Sinchenko, and P. Monceau, Physical Review B **101**, 155144 (2020).

[36] A. A. Sinchenko, P. D. Grigoriev, P. Lejay, and P. Monceau, Physical Review B **96**, 245129 (2017).

[37] F. H. Yu, T. Wu, Z. Y. Wang, B. Lei, W. Z. Zhuo, J. J. Ying, and X. H. Chen, Physical Review B **104**, L041103 (2021).

[38] R. Okuma, D. Ueta, S. Kuniyoshi, Y. Fujisawa, B. Smith, C. Hsu, Y. Inagaki, W. Si, T. Kawae, H. Lin, F. Chuang, T. Masuda, R. Kobayashi, and Y. Okada, Scientific Reports **10**, 15311 (2020).

[39] P. Anderson, Materials Research Bulletin **8**, 153–160 (1973).

[40] L. Balents, Nature **464**, 199–208 (2010).

[41] Y. Shimizu, K. Miyagawa, K. Kanoda, M. Maesato, and G. Saito, Physical Review Letters **91**, 107001 (2003).

[42] M. F. Collins and O. A. Petrenko, Canadian Journal of Physics **75**, 605–655 (1997).

[43] M. Mekata, Journal of the Physical Society of Japan **42**, 76–82 (1977).

[44] T. Takagi and M. Mekata, Journal of the Physical Society of Japan **64**, 4609–4627 (1995).

[45] N. Achiwa, Journal of the Physical Society of Japan **27**, 561–574 (1969).

[46] W. B. Yelon, D. E. Cox, and M. Eibschütz, Physical Review B **12**, 5007–5015 (1975).

[47] S. Niitaka, H. Kageyama, M. Kato, K. Yoshimura, and K. Kosuge, Journal of Solid State Chemistry **146**, 137–143 (1999).

[48] S. Niitaka, H. Kageyama, K. Yoshimura, K. Kosuge, S. Kawano, N. Aso, A. Mitsuda, H. Mitamura, and T. Goto, Journal of the Physical Society of Japan **70**, 1222–1225 (2001).

[49] E. V. Sampathkumaran and A. Niazi, Physical Review B **65**, 180401 (2002).

[50] H. Kageyama, K. Yoshimura, K. Kosuge, H. Mitamura, and T. Goto, Journal of the Physical Society of Japan **66**, 1607–1610 (1997).

[51] A. Maignan, C. Michel, A. Masset, C. Martin, and B. Raveau, European Physical Journal B **15**, 657–663 (2000).

[52] S. Rayaprol, K. Sengupta, and E. Sampathkumaran, Solid State Communications **128**, 79–84 (2003).

[53] S. Mitsuda, H. Yoshizawa, N. Yaguchi, and M. Mekata, Journal of the Physical Society of Japan **60**, 1885–1889 (1991).

[54] S. Mitsuda, N. Kasahara, T. Uno, and M. Mase, Journal of the Physical Society of Japan **67**, 4026–4029 (1998).

[55] M. Mekata, N. Yaguchi, T. Takagi, T. Sugino, S. Mitsuda, H. Yoshizawa, N. Hosoito, and T. Shinjo, Journal of the Physical Society of Japan **62**, 4474–4487 (1993).

[56] J. Rossat-Mignod, P. Burlet, J. Villain, H. Bartholin, W. Tcheng-Si, D. Florence, and O. Vogt, Physical Review B **16**, 440–461 (1977).

[57] Y. Fang, F. Tang, Y. R. Ruan, J. M. Zhang, H. Zhang, H. Gu, W. Y. Zhao, Z. D. Han, W. Tian, B. Qian, X. F. Jiang, X. M. Zhang, and X. Ke, Physical Review B **101**, 094424 (2020).

[58] S. A. M. Mentink, A. Drost, G. J. Nieuwenhuys, E. Frikkee, A. A. Menovsky, and J. A. Mydosh, Physical Review Letters **73**, 1031–1034 (1994).

[59] A. Dönni, G. Ehlers, H. Maletta, P. Fischer, H. Kitazawa, and M. Zolliker, Journal of Physics: Condensed Matter **8**, 11213 (1996).

[60] V. Fritsch, S. Lucas, Z. Huesges, A. Sakai, W. Kittler, C. Taubenheim, S. Woitschach, B. Pedersen, K. Grube, B. Schmidt, P. Gegenwart, O. Stockert, and H. v. Löhneysen, Journal of Physics: Conference Series **807**, 032003 (2017).

[61] S. K. Upadhyay, K. K. Iyer, and E. V. Sampathkumaran, Journal of Physics: Condensed Matter **29**, 325601 (2017).

[62] M. He, X. Xu, Z. Wu, C. Dong, Y. Liu, Q. Hou, S. Zhou, Y. Han, J. Wang, and Z. Qu, Physical Review Materials **7**, 033401 (2023).

[63] Y. Chen, Y. Zhang, R. Li, H. Su, Z. Shan, M. Smidman, and H. Yuan, Physical Review B **107**, 094414 (2023).

[64] K. K. Iyer, K. Maiti, S. Rayaprol, R. Kumar, S. Mattepanavar, S. Dodamani, and E. V. Sampathkumaran, Physical Review Materials **7**, L101401 (2023).

[65] H. Yoshida, E. Takayama-Muromachi, and M. Isobe, Journal of the Physical Society of Japan **80**, 123703 (2011).

[66] M. Matsuda, C. de la Cruz, H. Yoshida, M. Isobe, and R. S. Fishman, Physical Review B **85**, 144407 (2012).

[67] J. Sugiyama, H. Nozaki, K. Miwa, H. Yoshida, M. Isobe, K. Pr ša, A. Amato, D. Andreica, and M. Månsson, Physical Review B **88**, 184417 (2013).

[68] T. Kida, A. Okutani, H. Yoshida, and M. Hagiwara, Physics Procedia **75**, 647–652 (2015).

[69] H. Taniguchi, S. Suzuki, T. Arakawa, H. Yoshida, Y. Niimi, and K. Kobayashi, AIP Advances **8**, 025010 (2018).

[70] H. Taniguchi, M. Watanabe, M. Tokuda, S. Suzuki, E. Imada, T. Ibe, T. Arakawa, H. Yoshida, H. Ishizuka, K. Kobayashi, and Y. Niimi, Scientific Reports **10**, 2525 (2020).

[71] H. Taniguchi, "Electrical detection of magnetic fluctuations in nanoscale frustrated magnetic materials", PhD thesis (Osaka University, 2020).

[72] C. Kittel, *Introduction to solid state physics (8th edition)* (Wiley, 2008).

[73] D. Shoenberg, *Magnetic oscillations in metals (cambridge monographs on physics)* (Cambridge University Press, 1984).

[74] K. Ueda and Y. Onuki, *Physics of heavy electron systems* (Shokabo, 1998).

[75] E. Hall, The London, Edinburgh, and Dublin Philosophical Magazine and Journal of Science **10**, 301–328 (1880).

[76] E. M. Pugh, Physical Review **36**, 1503–1511 (1930).

[77] E. M. Pugh and T. W. Lippert, Physical Review **42**, 709–713 (1932).

[78] N. Nagaosa, J. Sinova, S. Onoda, A. H. MacDonald, and N. P. Ong, Reviews of Modern Physics **82**, 1539–1592 (2010).

[79] R. Karplus and J. M. Luttinger, Physical Review **95**, 1154–1160 (1954).

[80] T. Jungwirth, Q. Niu, and A. H. MacDonald, Physical Review Letters **88**, 207208 (2002).

[81] M. Onoda and N. Nagaosa, Journal of the Physical Society of Japan **71**, 19–22 (2002).

[82] J. Smit, Physica **21**, 877–887 (1955).

[83] J. Smit, Physica **24**, 39–51 (1958).

[84] C. M. Hurd, *The hall effect in metals and alloys* (Springer, 1972).

[85] J. Kondo, Progress of Theoretical Physics **27**, 772–792 (1962).

[86] J.-P. Jan, Helvetica Physica Acta **25**, 677 (1952).

[87] J. M. Lavine, Physical Review **123**, 1273–1277 (1961).

[88] S. Onoda, N. Sugimoto, and N. Nagaosa, Physical Review B **77**, 165103 (2008).

[89] M. Watanabe, R. Nakamura, S. Lee, T. Asano, T. Ibe, M. Tokuda, H. Taniguchi, D. Ueta, Y. Okada, K. Kobayashi, and Y. Niimi, AIP Advances **11**, 015005 (2021).

[90] J.-G. Park, I. Swainson, W. Buyers, M. Jung, and Y. Kwon, Physica B: Condensed Matter **241-243**, 684–686 (1997).

[91] K. Stöwe, Journal of Alloys and Compounds **307**, 101–110 (2000).

[92] M. H. Jung, K. Umeo, T. Fujita, and T. Takabatake, Physical Review B **62**, 11609–11613 (2000).

[93] T. Ohta, K. Sakai, H. Taniguchi, B. Driesen, Y. Okada, K. Kobayashi, and Y. Niimi, Applied Physics Express **13**, 043005 (2020).

[94] M. Matsuda, S. E. Dissanayake, H. K. Yoshida, M. Isobe, and M. B. Stone, Physical Review B **102**, 214411 (2020).

[95] H. Nagasawa, Physics Letters A **41**, 39–40 (1972).

[96] H. Yamada and S. Takada, Journal of the Physical Society of Japan **34**, 51–57 (1973).

[97] H. Yamada and S. Takada, Progress of Theoretical Physics **48**, 1828–1848 (1972).

[98] B. Raquet, M. Viret, E. Sondergard, O. Cespedes, and R. Mamy, Physical Review B **66**, 024433 (2002).

[99] H. Yoshida, Y. Muraoka, T. Sörgel, M. Jansen, and Z. Hiroi, Physical Review B **73**, 020408 (2006).

[100] U. Wedig, P. Adler, J. Nuss, H. Modrow, and M. Jansen, Solid State Sciences **8**, 753–763 (2006).

[101] H. Yoshida, S. Ahlert, M. Jansen, Y. Okamoto, J.-I. Yamaura, and Z. Hiroi, Journal of the Physical Society of Japan **77**, 074719 (2008).

[102] P. Norton, T. Braggins, and H. Levinstein, Physical Review B **8**, 5632–5653 (1973).

[103] J. Ye, Y. B. Kim, A. J. Millis, B. I. Shraiman, P. Majumdar, and Z. Te šanovi ć, Physical Review Letters **83**, 3737–3740 (1999).

[104] Y. Lyanda-Geller, S. H. Chun, M. B. Salamon, P. M. Goldbart, P. D. Han, Y. Tomioka, A. Asamitsu, and Y. Tokura, Physical Review B **63**, 184426 (2001).

[105] G. Tatara and H. Kawamura, Journal of the Physical Society of Japan **71**, 2613–2616 (2002).

[106] H. Kawamura, Journal of Magnetism and Magnetic Materials **310**, 1487–1493 (2007).

[107] H. Ishizuka and N. Nagaosa, Physical Review B **103**, 235148 (2021).

[108] T. Miyasato, N. Abe, T. Fujii, A. Asamitsu, S. Onoda, Y. Onose, N. Nagaosa, and Y. Tokura, Physical Review Letters **99**, 086602 (2007).

[109] S. Onoda and N. Nagaosa, Physical Review Letters **90**, 196602 (2003).

[110] Y. Niimi, D. Wei, and Y. Otani, Journal of the Physical Society of Japan **86**, 011004 (2017).

[111] H. Taniguchi, M. Watanabe, T. Ibe, M. Tokuda, T. Arakawa, T. Taniguchi, B. Gu, T. Ziman, S. Maekawa, K. Kobayashi, and Y. Niimi, Physical Review B **102**, 094405 (2020).

Acknowledgements

First of all, I would like to express my appreciation to my supervisor, Prof. Yasuhiro Niimi, who has provided immense support throughout my Doctoral course. This project would not have been possible without his help. I would also like to thank Prof. Nan Jiang for the many helpful discussions and advice during my research.

I am also grateful to Prof. Kensuke Kobayashi, who has allowed me to start my journey at Osaka university in the first place, as well as many support throughout the course. I am also grateful to Prof. Tomonori Arakawa, who has provided many helpful technical advice and support on top of general support throughout the course, as well as many troubleshooting regarding the refrigerators.

Regarding $CeTe_3$, this research would not have been possible without the bulk samples provided by Prof. Yoshinori Okada, Prof. Ryutaro Okuma, and Prof. Daichi Ueta, as well as fruitful discussions regarding the physical properties of $CeTe_3$. For Ag_2CrO_2, I would like to thank Prof. Hiroyuki K. Yoshida for providing the bulk samples and discussions on the magnetic structure of Ag_2CrO_2, and Prof. Ochi Masayuki and Prof. Hiro Ishizuka for their immense theoretical support regarding the possible origins of the AHE. I am grateful to Prof. Hirokazu Tada and Prof. Kohei Hamaya for their electron beam lithography system.

I would like to thank Junko Sasaki and Akiko Takao for their secretary service. Additionally, I would like to thank Prof. Shigeo Wada, Prof. Akira Oiwa, Prof. Toshiharu Katayama, Kumi Shinoki, and Manami Ishibashi for

their many support throughout the Osaka Univeristy Honors Program for Graduate Schools in Science.

I would also like to thank Prof. Masayuki Hagiwara, Prof. Masayuki Ochi, Prof. Junichi Shiogai, and Prof. Shintaro Takada for taking the time to review this thesis.

I would also like to show my appreciation to members of the former Kobayashi group and the current Niimi group. For the research of $CeTe_3$, I would like to thank Takashi Ibe for introducing me to the research of atomically layered materials, Dr. Sanghyun Lee, Takuya Asano for their support of the dilution refrigerator, Dr. Masahiko Yokoi for his support on the C-mag refrigerator, Ryotaro Asama and Tomo Higashihara for further research of the rare-earth tritellurides. For the research of Ag_2CrO_2, I would like to thank Dr. Hiroki Taniguchi and Dr. Shota Suzuki for their support on sample fabrication, and Dr. Masashi Tokuda for his support on the setup of the variable temperature insert. Although I have only listed above the people related to this thesis, I am grateful to all members of the group for their help throughout this course.

Lastly, I would like to express my gratitude to my friends, my family including my beloved dog Taro, and my partner Kyoko, who has always comforted me with their kindness.

Lists of Publication

Peer-reviewed papers

1. M.Watanabe, T. Higashihara, R. Asama, M. Tokuda, S. Suzuki, N. Jiang, M. Ochi, H. Ishizuka, H. K. Yoshida, and Y. Niimi, "Unconventional anomalous Hall effect in a triangular lattice antiferromagnet", In preparation for submission to Physical Review B.

2. M. Maeda, M. Tokuda, R. Nakamura, M. Watanabe, K. Takaki, N. Jiang, K. Kudo, and Y. Niimi, "Fabrication of Se-doped PtBi2 Thin Film Devices", JPS Conference Proceedings 38, 011036 (2023).

3. R. Nakamura, M. Tokuda, M. Watanabe, M. Nakajima, K. Kobayashi, and Y. Niimi, "Thickness-induced crossover from strong to weak collective pinning in exfoliated $FeTe_0.6Se_0.4$ thin films at 1 T". Physical Review B 104, 165412 (2021).

4. K. Fujiwara, S. Iwakiri, M. Watanabe, R. Nakamura, M. Yokoi, K. Kobayashi, and Y. Niimi, "Charge density wave transitions in mechanically-exfoliated $NbSe_3$ devices". Japanese Journal of Applied Physics 60, 070904 (2021).

5. M. Watanabe, R. Nakamura, S.-H. Lee, T. Asano, T. Ibe, M. Tokuda, H. Taniguchi, D. Ueta, Y. Okada, K. Kobayashi, and Y. Niimi, "Shubnikov-de-Haas oscillation and possible modification of effective mass in $CeTe_3$ thin films". AIP Advances 11, 015005 (2021).

6. H. Taniguchi, M. Watanabe, T. Ibe, M. Tokuda, T. Arakawa, T. Taniguchi, B. Gu, T. Ziman, S. Maekawa, K. Kobayashi, and Y. Niimi, "Spin treacle in a frustrated magnet observed with spin current", Physical Review B 102, 094405 (2020).

7. M. Watanabe, S.-H. Lee, T. Asano, T. Ibe, M. Tokuda, H. Taniguchi, D. Ueta, Y. Okada, K. Kobayashi, and Y. Niimi, "Quantum oscillations with magnetic hysteresis observed in $CeTe_3$ thin films", Applied Physics Letters 117, 072403 (2020).

8. H. Taniguchi, M. Watanabe, M. Tokuda, S. Suzuki, E. Imada, T. Ibe, T. Arakawa, H. Yoshida, H. Ishizuka, K. Kobayashi, and Y. Niimi, "Butterfly-shaped magnetoresistance in triangular-lattice antiferromagnet Ag_2CrO_2", Scientific Reports 10, 2525 (2020).

First author presentations (International conferences)

Oral presentations

1. M. Watanabe, R. Asama, M. Tokuda, S. Suzuki, N. Jiang, H. K. Yoshida, and Y. Niimi, "Anomalous Hall effect induced by spin fluctuations in a triangular lattice antiferromagnet", Intermag 2023 (Sendai, Japan, May 2023).

2. M. Watanabe, S. Lee, T. Asano, T. Ibe, M. Tokuda, H. Taniguchi, D. Ueta, Y. Okada, K. Kobayashi, and Y. Niimi, "Coexistence of quantum oscillation and magnetic hysteresis in $CeTe_3$ thin films", Annual Conference on Magnetism and Magnetic Materials 2020 (MMM2020) (Online, November 2020).

Poster presentations

1. M. Watanabe, R. Asama, M. Tokuda, S. Suzuki, H. K. Yoshida, and Y. Niimi, "Unique magnetoresistance and Hall effects in classical triangular antiferromagnet Ag_2CrO_2 thin films", 24th International Colloquium on Magnetic Films and Surfaces (ICMFS-2022) (Okinawa, Japan, July 2022).

2. M. Watanabe, S. Lee, T. Asano, T. Ibe, M. Tokuda, H. Taniguchi, D. Ueta, Y. Okada, K. Kobayashi, and Y. Niimi, "Hall and butterfly-shaped magnetoresistance effects in atomically thin $CeTe_3$ films", New Perspective in Spin Conversion Science 2020 (NPSCS2020) (Chiba, Japan, February 2020).

3. M. Watanabe, T. Ibe, M. Tokuda, H. Taniguchi, Y. Okada, K. Kobayashi, and Y. Niimi, "Hall measurements in atomically thin $CeTe_3$ films", International Symposium for Nano Science 2019 (ISNS 2020) (Osaka, Japan, November 2019).